Summer 8-4-2011

Thermoelectric Properties of Zr0.5Hf0.5Ni1-xPdxSn0.99Sb0.01 and Effect of Nanoinclusions on Transport Properties of Half Heuslers

Rumana Yaqub
University of New Orleans, ryaqub1@uno.edu

Thermoelectric Properties of $Zr_{0.5}Hf_{0.5}Ni_{1-x}Pd_xSn_{0.99}Sb_{0.01}$ and Effect of Nanoinclusions on Transport Properties of Half Heuslers

A Dissertation

Submitted to the Graduate Faculty of the
University of New Orleans
In partial fulfillment of the
Requirement for the degree of

Doctor of Philosophy
In
Engineering & Applied Sciences

by
Rumana Yaqub

B.Sc Govt Punjab University,1985
M.Sc Govt College University, Pakistan,1989
M.Sc Wayne State University,2007

August, 2011

Dedication

I dedicate this thesis to my parents who taught me the value of education and I am

deeply indebted to them for their continued support, encouragement and

unwavering faith in me

AKNOWLEDGMENT

My experience as a graduate student in University of New Orleans has changed completely significantly for better suitability with academic research and philosophy towards acquiring knowledge. Many people have contributed directly and indirectly to my research work. I am thankful to all those who have affected and been affecting my life and attitudes to become a strong person.

I express sincere thanks and gratitude to my advisor Dr Kevin Stokes for giving me an opportunity to embark a research on thermoelectric and for his unconditional support, invaluable guidance, patience and motivation throughout this research. He opened a new research filed for me on which I had no previous experience. I wish to say thanks to Dr Ferdinand P Poudeu Poudeu for allowing me to use his lab with freedom for preparing samples and making measurements. Without his cooperation this work would not have been accomplished.

I express my special gratitude to all my committee members, Dr Paul J Schilling, Dr Weilie Zhou and Dr Leszek Malkinski. I am indebted to Dr Leonard Spinu for agreeing to become a committee member in the absence of Dr Leszek Malkinski.

Special thanks are due to postdoctoral fellows Dr Nathan Takas and Dr Julien P A Makongo for their invaluable assistance in helping me with measurements on ULVAC ZEM 3 and laser flash apparatus. Dr Sumithra Santhanam also merits special acknowledgement for helping me in pressing samples. I am thankful to Dr Girija and Praniti Sahoo for providing me with nanoinclusions. Besides these people, I greatly appreciate Westly Nolting for doing Hall Effect measurements on half Heusler samples.

The period I have spent at AMRI is a happy and rewarding time for me because I have met many great people. I have benefited from their knowledge, patience and selflessness. I am very thankful to the administrative staff of AMRI and the Department of Physics. Special thanks to Denise who has been a constant emotional and moral help for me.

My whole family has always been supporting me wholeheartedly and I am eternally grateful for their unconditional love.

Abstract

Thermoelectric materials convert temperature gradients into electricity and vice-versa. These materials utilize the Seebeck effect for power generation and function without moving parts and are highly reliable. The efficiency of thermoelectric devices is related to the dimensionless figure of merit for the constituent materials, defined as $ZT = \frac{S^2\sigma}{\kappa}T$ where S is the Seebeck coefficient, σ is the electrical conductivity, κ is the thermal conductivity and T is the temperature. Maximizing ZT is very challenging because of interdependence of parameters, for example, increasing the electrical conductivity by increasing the carrier concentration invariably lowers S and vice versa. Presently numerous thermoelectric materials are being investigated by different research groups. Despite having high thermal conductivity, half-Heusler materials are promising candidates for thermoelectric applications due to their relatively high power factor ($S^2\sigma$) and the ability to tune the thermal and electrical properties through substitutional doping.

In this research work, I have investigated the synthesis and transport properties of half Heusler series $Zr_{0.5}Hf_{0.5}Ni_{1-x}Pd_xSn_{0.99}Sb_{0.01}$ (0≤x≤1). Also the role of NiO and HfO$_2$ nanoinclusions in half –Heusler matrix were studied. The half Heusler samples were prepared by solid state reaction. Resistivity, Seebeck coefficient and thermal conductivity were measured for all samples over a temperature range from room temperature to 750K. Hall effect measurements at room temperature were also performed. Addition of NiO inclusions did result in an improvement in ZT whereas addition of 3% vol HfO$_2$ in $Zr_{0.5}Hf_{0.5}Ni_{0.8}Pd_{0.2}Sn_{0.99}Sb_{0.01}$ showed 19% improvement in ZT.

Key Words: Half Heusler, thermoelectric, nanoinclusions, nanomaterial,

List of Figures

List of Tables

Table of Contents

CHAPTER 1

BASIC PRINCIPLES OF THERMOELECTRICS

1.1 Introduction

The alarming levels of global warming combined with increased energy demands have initiated many workshops and conferences to discuss strategies for tackling the present energy crisis. Decreasing fossil fuel supplies and a series of environmental problems like ozone depletion, greenhouse emissions, and catastrophic oil spills have drawn broad communal concern. These have led to renewed interest in science and technology in order to provide a sustainable supply of clean energy. Solar cells, wind turbines and fuel cells are some of the directions in which research is moving. One avenue to address these energy issues is the field of thermoelectrics which investigates solid state materials to convert heat to electricity (power generation) or electricity to heat (solid state cooling). If high efficiency materials can be identified and synthesized, the thermoelectric field has the potential to meet the future energy challenge.

Thermoelectric devices possess the desirable features of being highly reliable, silent, scalable, have no moving parts and use no greenhouse gases. In heating and cooling applications, thermoelectrics provide extraordinary temperature control since both heating and cooling is performed by the same module. The down side of thermoelectric devices is their poor efficiency (around 5-10% for near room temperature power generation applications). The efficiency of thermoelectric devices is fundamentally limited by the material's properties. So far the best commercially available thermoelectric material, is Bi_2Te_3 (and related alloys) which have *ZT* around 1. With this value, the coefficient of performance of thermoelectric cooler is about one

third the values for conventional compressor-based refrigerator systems. Thermoelectric devices still have a niche market. The low efficiency or coefficient of performance is acceptable in certain applications, but to be economically competitive with the kitchen refrigerator, for example, a thermoelectric refrigerator requires $ZT \approx 3$ at room temperature[1].

1.1.1 Brief History of Thermoelectrics

Thermoelectric phenomena were first observed by Thomas Johann Seebeck in 1821 [2]. He performed an experiment in which two dissimilar conductors were connected and maintained at different temperatures. When a compass was placed in the vicinity of this closed circuit compass needle was deflected. The explanation of his experiment was given by later that the temperature gradient, depending on the type of conducting materials, induces current along the closed loop and therefore by Ampere's law deflects the compass. The voltage produced was found to be proportional to the temperature difference between the two junctions. This discovery initiated a period of research that lasted roughly 30 years during which the complementary effect was discovered in 1834 by Peltier who observed temperature changes in the vicinity of junction between dissimilar conductors when was current passed [3]. In the subsequent three decades from 1821 to 1851, thermoelectrics were understood macroscopically, and their relevance to power generation and refrigeration was recognized. In 1895 Rayleigh used thermoelectric phenomenon in the generation of electricity, although he incorrectly calculated the efficiency of his thermoelectric generators. In 1909 and 1911, Altenkirch derived the basic theory of thermoelectrics[4, 5]. From the 1930s, the field of thermoelectrics progressed rapidly which lead to a microscopic understanding and development of new materials[6]. As research developed, thermoelectrics gradually started gaining attention in industry in the early 1960's. In the 1990s, renewed interest in thermoelectrics provided research opportunities to advance thermoelectric

materials discovery in several areas including complex material structures and nanometer-scale materials.
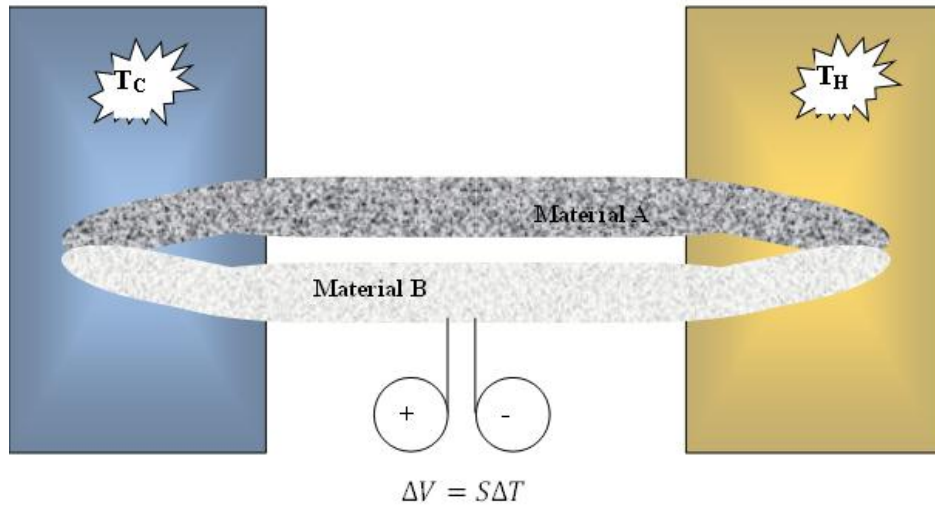
Figure:1-1 Schematic for the observation of Seebeck effect

Current research aimed at developing the next generation thermoelectric materials typically follows these two different approaches: One involves traditional method to look for new families of bulk thermoelectric materials and other method is focused on improving existing material properties by low dimensional strategy or by alloying. Some new materials have been proven to be viable technologically in power generation and refrigeration applications[7].

Discovery of phonon-glass electron-single crystal (PGEC) materials pioneered by Slack was a breakthrough in the field of thermoelectric materials [8]. PGEC materials have electronic properties similar to good semiconductor single crystals but thermal properties which are associated with amorphous materials. The main task of the PGEC approach is to generate solids that have very low thermal conductivity but high electrical conductivity. Skutterudites and clathrates are among the members of novel PGEC materials.

The low-dimensional material is another approach for the selection of thermoelectric materials. This method has two strategies. One approach uses synthesis of low dimensional material to boost the Seebeck coefficient and to control the electrical conductivity independently[9]. In the second strategy, numerous nanometer-scale interfaces are used to scatter phonons more effectively than electrons which lowers the thermal conductivity without a detrimental effect on electron transport [10]. Bi_2Te_3/Sb_2Te_3 superlattices (SL) and PbTe/PbSeTe quantum dot superlattices (QDSL) are examples of this second approach and have been reported to show tremendous increase in *ZT* [11, 12].

1.2 Thermoelectric Phenomena

1.2.1 Thermoelectric Coefficients

The Seebeck and Peltier coefficients are the important parameters for describing thermoelectric materials for energy conversions applications. They are called cross effects since they connect an electric response to a thermal gradient or a thermal current to electrical current. The Seebeck effect was discovered by Thomas Johann Seebeck [2] and is thermoelectric phenomenon and has considerable importance in technological applications. The basic demonstration of the Seebeck coefficient is illustrated in Fig 1.1. Each end of bi-metallic couple is kept at a different temperature. The temperature gradient causes charge carriers to diffuse from hot side the cold side. The build-up of charge carriers on the cold side eventually stops when the electric field created by the charge separation in material reaches the steady state. An increase in the temperature gradient can resume the buildup of charge carriers on the cold side and thus lead to an increase in the thermoelectric voltage. This voltage can drive a continuous current flowing through the conductor if the junctions are kept at different temperatures. The temperature difference ΔT is related to the open-circuit voltage across the two junctions as:

$$S_{ab} = \frac{\Delta V}{\Delta T} \tag{1-1}$$

The differential Seebeck $S_{ab} = S_a + S_b$ is sum of the absolute Seebeck coefficients of the two materials and measures the magnitude of an induced thermoelectric voltage in response to a temperature difference across the material in typical units of $\mu V/K$. S_a and S_b in (1-1) Seebeck coefficients of material A and B, respectively. The Seebeck coefficient can be negative (electrons as charge carriers) or positive (holes as charge carriers).

The Peltier effect shows that carrier can also carry heat when they flow through the conductor (see Fig. 1-2) [3]. The Peltier effect can be considered to be the reverse of the Seebeck effect. When a current passes through two dissimilar materials such as metals or semiconductors a rate of heating q occurs at one junction and a rate of cooling $-q$ occurs at the other junction depending on the direction of flow of current. The Peltier heat q is proportional to the current I by

$$q = \Pi_{ab} I = (\Pi_a - \Pi_b) I \tag{1-2}$$

If current is passed through a material with temperature gradient, it also accompanied by heat generation or absorption. This is called the Thomson effect [13]. The gradient of the heat flux is given as:

$$\frac{dq}{dx} = T_{ab} I \frac{dT}{dx} \tag{1-3}$$

where x is a spatial coordinate, and T_{ab} is Thomson coefficient. The Thomson coefficient is distinct among the three main thermoelectric coefficient because it is the only one directly

5
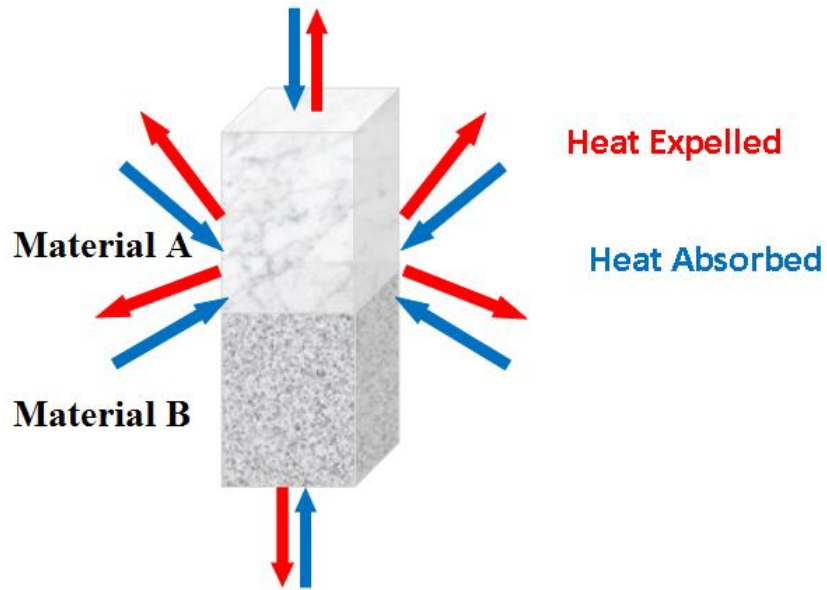
Figure:1-2 The Peltier effect. Heat is expelled or absorbed at the junction between dissimilar materials when an electric current is injected
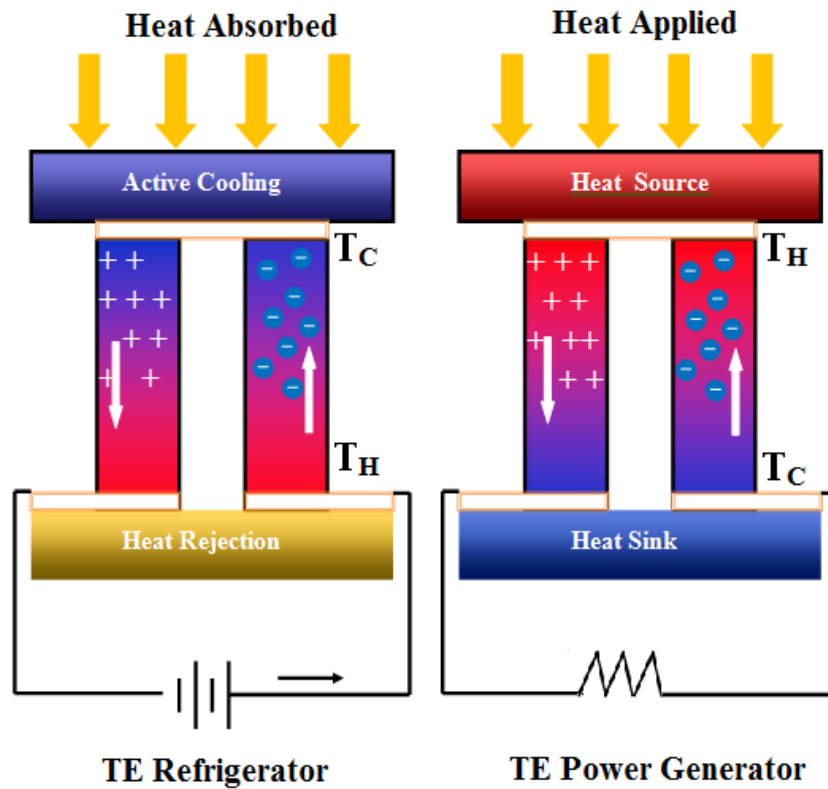
Figure:1-3 Schematic of a thermoelectric couple.

measurable for individual materials (no junction is necessary to observe the effect). Lord Kelvin suggested a relation that connects three coefficients to each other [14]

$$\Pi_{ab} = S_{ab}T \tag{1-4}$$

$$\mathrm{T}_{ab} = T\frac{dS_{ab}}{dT} \tag{1-5}$$

1.2.2 Cooling, Power Generation and the Thermoelectric Figure of Merit

The principal component of a thermoelectric (TE) device is a TE couple which comprises a "p" branch with a positive Seebeck coefficient, S_p, (hole charge carriers) and an "n" branch with a negative Seebeck coefficient, S_n, (charge carriers are electrons). The branches are set thermally in parallel and electrically in series. Fig. 1.3 shows schematic of such a TE couple. The total thermal conductance κ and electrical resistance R are given as:

$$\kappa = \frac{k_p A_p}{L_p} + \frac{k_n A_n}{L_n} \qquad\qquad R = \frac{L_p \rho_p}{A_p} + \frac{L_n \rho_n}{A_n} \tag{1-6}$$

where k, L and A are the thermal conductivity, length and cross section of the legs.

The efficiency of TE refrigeration modules is defined as the ratio of the rate at which heat is extracted from the source to the rate of expenditure of electricity energy.

$$\phi = \frac{Q_C}{W} = \frac{(S_p - S_n)IT_C - \kappa\Delta T - \frac{1}{2}I^2 R}{I[(S_p - S_n)\Delta T + IR]} \tag{1-7}$$

where $\Delta T = T_C - T_H$, T_C and T_H are the temperatures of the cold and hot junction, respectively. If there were no irreversible effects, ϕ equals $\frac{T_C}{\Delta T}$, the Carnot limit. For a given ΔT, ϕ depends on the current. By optimizing current, we can obtain either a maximum heat pump or maximum efficiency. The current which yields maximum heat pump also produces the maximum ΔT. The maximum ϕ is given as:

$$\phi_{max} = \frac{T_C}{T_H - T_C} \frac{\sqrt{1+Z\bar{T}} - \frac{T_H}{T_C}}{\sqrt{1+Z\bar{T}} + 1} \tag{1-8}$$

Similarly in a thermoelectric power generation device, the efficiency is defined as the rate of power delivered (W) to the heat flow from the source to the sink (Q_c) [6]

$$\eta = \frac{W}{Q_c} = \frac{I[(S_p - S_n)\Delta T - IR]}{K\Delta T + [(S_p - S_n)IT_H - \frac{1}{2}I^2 R]}. \tag{1-9}$$

To achieve maximum power generation, current can be tuned by optimizing load to couple resistance ratio. The maximum efficiency (η_{max}) of a TE power generation device is given by Ioffe [15] :

$$\eta_{max} = \frac{T_H - T_C}{T_H} \frac{\sqrt{1+Z\bar{T}} - 1}{\sqrt{1+Z\bar{T}} + \frac{T_C}{T_H}} \tag{1-10}$$

where $\bar{T}$ is the average temperature at which ZT versus T curve reaches maximum, i.e. at the optimum temperature. The Carnot efficiency $\eta_{carnot} = \frac{T_H - T_C}{T_H}$ is the highest efficiency permitted by thermodynamics for a heat engine. The term $\frac{\sqrt{1+Z\bar{T}} - 1}{\sqrt{1+Z\bar{T}} + \frac{T_C}{T_H}}$ is the loss term, and Z is called the figure of merit defined as:

$$Z = \frac{S^2}{R\kappa} \tag{1-11}$$

The efficiency of a power generator and coefficient performance of refrigeration are both related to the Carnot efficiency and figure of merit Z. The major difference between the two is efficiency of a power generator η_{max} increases with increasing ΔT but is limited by Carnot efficiency which is less than 1 while coefficient performance of refrigeration ϕ_{max} increases with decreasing ΔT and can reach a value larger than 1.

A quick observation can be made from equation (1-10): The efficiency tends towards Carnot limit when $Z\bar{T}$ approaches infinity. There is no theoretical limit on $Z\bar{T}$. Estimation based on equation (1-10) are shown in Table 1.1 that gives the clear picture of the relationship of

8
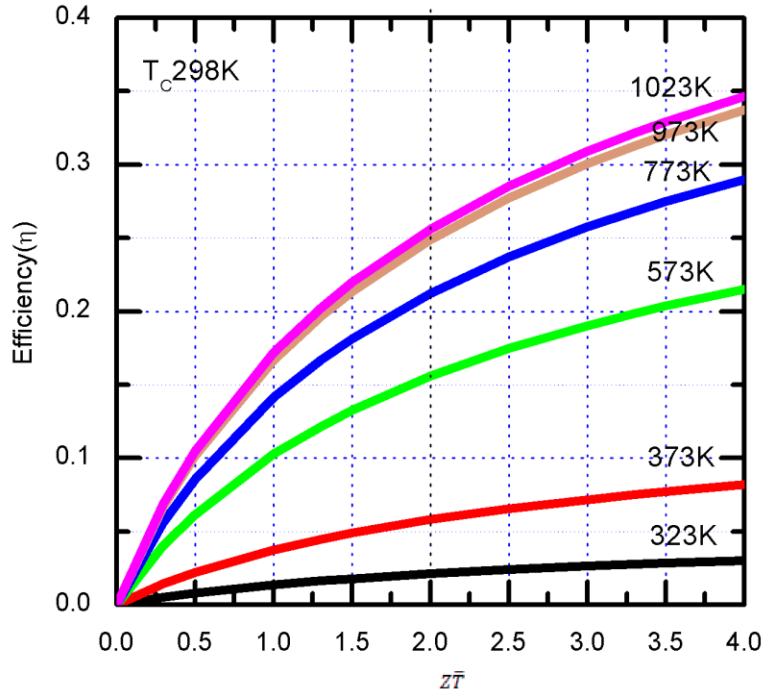
Figure:1-4 Conversion efficiency η as a function of average figure of merit $Z\bar{T}$ calculated using equation (1-10).

Table 1.1 Efficiency variation with $Z\bar{T}$.

$Z\bar{T}$	1	1	1	1	2	2	2	2	3	3	3	3
$T_H(°C)$	323	573	773	1023	323	573	773	1023	323	573	773	1023
$T_C(°C)$	298	298	298	298	298	298	298	298	298	298	298	298
η	1.4%	10.3%	14.1%	17.2%	2.1%	15.6%	21.2%	25.6%	2.6%	19.1%	25.8%	30.9%
η/η_{carnot}	17.7%	21.4%	23.0%	24.3%	27.6%	32.5%	34.6%	36.3%	34.2%	39.7%	41.9%	43.6%

9

theoretical $Z\bar{T}$ values to the relative Carnot efficiency. The graph in Fig.1-4 shows the efficiency of power generator as a function of the material's dimensionless figure-of-merit for a range of operation temperatures and the heat sink temperature T_C is fixed to be 25°C. It is evident the higher the $Z\bar{T}$, the higher the efficiency. It is noticed that the thermocouple with $Z\bar{T}$ in the range 1-2 has conversion efficiency of ~27.5-40.% at working temperature of 700 °C.

For a thermocouple consisting of p and an n type legs, the figure of merit is given as

$$Z = \frac{(S_p - S_n)^2}{[(k_p \rho_p)^{1/2} + (k_n \rho_n)^{1/2}]^2} \qquad (1\text{-}12)$$

Equation (1.12) shows that Z is independent of the dimensions of the legs of the thermoelectric couple but depends upon the product upon the product $\kappa\rho$. By selection of best p type and n type thermoelectric materials which have similar transport properties the figure of merit can be directly related to the Seebeck coefficient S resistivity ρ according by equation:

$$Z = \frac{S^2}{\rho k} \qquad (1\text{-}13)$$

In addition to material properties, practical parameters must be considered when designing a thermoelectric device. These additional parameters include thermal and electrical contact resistance. The thermal contact resistance is generated by the heat transfer characteristics of the ceramic plates and contact layers used to build the thermoelectric module. The heat exchangers and corresponding heat losses should also be taken into account. Moreover, the transport properties of TE materials vary with temperature. When thermoelectric device is operating across a wide temperature range, temperature-dependent material and device parameters should be factored in the calculation of the performance.

1.3 Transport of Electrical and Heat Current

Generally, classical transport phenomena are regulated by two opposing mechanisms: driving forces (electric fields and temperature gradients) which are responsible for the motion of carriers and scattering which retards the direct motion. This situation is described by the linearized Boltzmann equation which provides the systematic method for accounting for effects of forces, currents and scattering on the electron and phonon distribution functions. Under certain assumptions and conditions, this equation may be used to describe charge and heat transport in solids.

The classical distribution function f (**k,r**,t) [6, 16] which determines the number of carriers in the **k**th state in the neighborhood of position of carrier r at time t is introduced to explain the occupancy of allowed energy states. The distribution function can be affected by various mechanisms, such as external fields (electric and magnetic fields), diffusion, and collision process or temperature gradient. The total rate of change of the distribution function is given by

$$\frac{df}{dt} = \left(\frac{\partial f}{\partial t}\right)_{diff} + \left(\frac{\partial f}{\partial t}\right)_{field} + \left(\frac{\partial f}{\partial t}\right)_{coll} \tag{1-14}$$

The subscripts *field*, *diff*, and *coll* denote the changes of f (**k,r**,t) under eternal fields, diffusion and collisions, respectively. For steady state we set $\frac{df}{dt} = 0$. The resulting result Boltzmann's transport equation for carriers after substituting $\left(\frac{\partial f}{\partial t}\right)_{diff} = \text{r.}\nabla_i f$ and $\left(\frac{\partial f}{\partial t}\right)_{coll} = \frac{1}{h}\text{k.}\nabla_k f$ is written as:

$$-\left(\frac{\partial f}{\partial t}\right)_{coll} = \text{r.}\nabla_i f + \frac{1}{h}\text{k.}\nabla_k f \tag{1-15}$$

The negative sign in front of collision term shows that collisions tend to reduce the occupancy of state **k**.

Under non-equilibrium conditions, the main contribution to scattering comes from the lattice defects, phonons, and grain boundaries. At low temperatures, static impurities and defects are the primary scattering mechanisms. As temperature increases, the thermal vibrations are enhanced and this becomes the main scattering mechanism for charge carriers. The effects of the various scattering mechanisms are expressed in terms of their relaxation times. The collision term in (1-15) is generally estimated in this way by using the relaxation time approximation[6]. To show small deviations of f (non-equilibrium distribution) from the equilibrium distribution f_o, it is assumed that the time rate of change of distribution function due to collisions is proportional to the deviation of the distribution function from its equilibrium value. In this case (1-14) can be written as:

$$\left(\frac{\partial f}{\partial t}\right) = -\frac{f-f_o}{\tau} \qquad (1\text{-}16)$$

which is Boltzmann equation in the relaxation time approximation and τ is relaxation time. This relaxation time is also called mean free time and describes average time between changes of occupancy of each energy level. The inverse of relaxation time is collision rate or scattering rate.

Generally the relaxation time varies with the energy of charge carriers and the energy dependence of relaxation time is expressed in a power law form as

$$\tau = \tau_o E^r \qquad (1\text{-}17)$$

where τ_o constant depends upon the effective mass of carriers and temperature and r scattering parameter depends upon the scattering mechanism involved.

1.3.2 Electron Distribution Function

The equilibrium distribution of electrons is determined by the Fermi-Dirac function [6] which takes into account Fermi energy E_F and gives the probability that a state of energy E is occupied

$$f_o(E) = \frac{1}{\text{Exp}[(E-E_F)/k_BT]+1} \tag{1-18}$$

Fermi energy strongly depends on carrier concentration and weakly on temperature. The term in (1-18) $\xi = E / k_B T$ is called the reduced energy with $\xi_F = E_F / k_B T$ the reduced Fermi energy. $E - E_F$ is the total energy transported by a carrier. The carrier concentration, number of occupied energy levels in the conduction band per unit crystal volume can obtained from energy dependent distribution function $f(E)$ by

$$\int_0^\infty f(E)g(E)dE = n \tag{1-19}$$

$g(E)$ is the density of states per unit volume, and n is the carrier concentration. For a single parabolic band structure, $E = \frac{h^2k^2}{8\pi m^*}$ and when E is measured from the band edge for either electrons or holes and $g(E)$ is given by[6]:

$$g(E) = \frac{4\pi(2m^*)^{3/2}E^{1/2}dE}{h^3} \tag{1-20}$$

1.3.3 General Expressions for Thermoelectric Parameters

When either an electric field or a temperature gradient is applied to a conductor, there is a flow of both charge and heat. The motion of electrons and phonons is treated separately without considering the effects of electron-phonon and phonon-electron scattering on the distribution function. That is, the electric field only influences the electron distribution and the temperature gradient alters both the electron and phonon distribution. But if only the electronic part of the

13

thermal conductivity is taken into account the effect on the phonon distribution can be ignored [6, 8, 16].

Thus contracting (1-15) and (1-16) we can find the departure of the electron distribution from the steady state which is supported in the absence of a field or temperature gradient,

$$-\frac{f-f_o}{\tau} = \mathrm{r} \cdot \nabla_i f + k \cdot \nabla_k f \qquad (1\text{-}21)$$

Assuming the temperature gradient and electric field are small so that deviations of distribution is small $f - f_o \ll f_o$, $\quad \nabla f = \nabla f_o$, $and \; \nabla_k f = \nabla_k f_o = \frac{\partial f_o}{\partial E} \nabla_k E = \hbar v \frac{\partial f_o}{\partial E}$ then (1-21) becomes

$$-\frac{f-f_o}{\tau} = \mathbf{v} \cdot \nabla_r f_o \frac{\mathbf{p}}{\hbar} \cdot \nabla_r f_o = \mathbf{v} \cdot (\nabla_r f_o + q\mathbf{E}\frac{\partial f_o}{\partial E}) \qquad (1\text{-}22)$$

which is the so-called "linearized Boltzmann Equation." For electrons $q = -e$ and for holes $q = +e$. From the electron distribution function (1-18) we get[6]:

$$\frac{\partial f_0}{\partial E} = \frac{\partial f_o}{\partial \xi}\frac{\partial \xi}{\partial E} = \frac{df_o}{d\xi}\frac{1}{k_B} : or \; \frac{df}{d\xi} = k_B T \frac{\partial f_o}{\partial E} \qquad (1\text{-}23)$$

$$\nabla_r f_o = \frac{df_o}{d\xi}\nabla_r \xi = kT\frac{\partial f_o}{\partial E}\nabla_r \xi \qquad (1\text{-}24)$$

$$\nabla \xi = \frac{\nabla_r E - \nabla_r E_F}{k_B T} - \frac{E - E_F}{k_B T^2} = -\frac{\nabla_r E_F}{k_B T} - \frac{E - E_F}{k_B T^2}\nabla_r T \qquad (1\text{-}25)$$

From (1-22), (1-24) and (1-25) we obtain distribution function as combination of equilibrium part of the distribution and change in distribution caused by external fields.

$$f = f_o - \tau\mathbf{v}.\,(-\frac{E - E_F}{T}\nabla_k T - \nabla_k \phi)\frac{\partial f_o}{\partial E} \qquad (1\text{-}26)$$

Electrochemical potential ϕ is the main driving force responsible for current or thermoelectric effect and is combination of chemical potential and electrostatic potential, *V*. The chemical potential occurs due to the gradient in carrier concentration and temperature whereas

14

the electrostatic potential builds through gradient in electric field, E. The relationship between these potentials and Fermi energy is:

$$E = -\nabla V \quad \text{and} \quad \emptyset = E_F + qV \tag{1-27}$$

Let us consider the simple case, where the field and temperature gradient lie along the x axis and when $f = f_o$ there is no flow of current. Furthermore, thermal velocity $(v^2 = \frac{2E}{3m^*})$ greatly exceeds the drift velocity and is isotropic

The electric current density j and heat current density w (heat flow per unit cross-section area) are given by[6]

$$j = \int_0^\infty qv\, f(E)g(E)dE = \frac{2q}{3m^*}\int_0^\infty g(E)\tau E \frac{\partial f_0}{\partial E}\left[\frac{\partial \emptyset}{\partial x} + (\frac{E-E_F}{T})\frac{\partial T}{\partial x}\right]dE \tag{1-28}$$

$$w = \int_0^\infty v(E - E_f)f(E)g(E)dE = -\frac{E}{q}kj + \frac{2}{3m^*}\int_0^\infty g(E)E^2 \frac{\partial f_0}{\partial E}\left[\frac{\partial \emptyset}{\partial x} + (\frac{E-E_F}{T})\frac{\partial T}{\partial x}\right]dE \tag{1-29}$$

1.3.4 Electrical Conductivity, Seebeck Coefficient and Electronic Thermal Conductivity

The electrical conductivity is the capability of material conducting and electric current is a result of charge carrier movement. When the electrical potential difference developed along the conducting material exists, mobile charge carriers create an electrical current. If ε is the electric field the electrical conductivity σ is expressed by equation

$$\sigma = \frac{j}{\varepsilon} \tag{1-30}$$

Let us set the temperature gradient to zero and the term $-(\frac{\partial \emptyset/\partial x}{q})$ in equation (1-28) is the electric field so that electrical conductivity (1-30) becomes

$$\sigma = -\frac{2q^2}{3m^*}\int_0^\infty g(E)\tau E \frac{\partial f_0}{\partial E}dE \tag{1-31}$$

To seek an equation for Seebeck coefficient we set up a temperature gradient so that the electric current be zero, then equation (1-28) reduces to

15

$$\frac{\partial \emptyset}{\partial x} \int g(E) \tau E \frac{\partial f_o}{\partial E} dE + \frac{1}{T} \frac{\partial T}{\partial x} \int_0^\infty g(E) \tau E (E - E_F) \frac{\partial f}{\partial E} dE = 0 \qquad (1\text{-}32)$$

Thus the Seebeck coefficient is expressed as:

$$S = \frac{\partial \emptyset / \partial x}{q \partial T / \partial x} = \frac{1}{qT} \left\{ E_F - \frac{\int_0^\infty g(E) \tau E^2 (\partial f_o / \partial E)}{\int_0^\infty g(E) \tau E (\partial f_o / \partial E)} \right\} \qquad (1\text{-}33)$$

To obtain an expression for thermal conductivity we ensure no current passes through the material. Under this condition of no current the electric thermal conductivity is equal to the ratio $w/(\partial T/\partial x)$. Thus from (1- 29) and (1- 32), we get

$$k_e = \frac{2}{3m^*T} \left\{ \frac{\left[\int_0^\infty g(E) \tau E (\partial f_o / \partial E) dE \right]^2}{\int_0^\infty g(E) \tau (\partial f_o / \partial E) dE} - \int_0^\infty g(E) \tau E (\partial f_o / \partial E) dE \right\} \qquad (1\text{-}34)$$

If we define the integral K_s as

$$K_s = \frac{2T}{3m^*} \int_0^\infty g(E) \tau E^{s+1} \frac{\partial f_o}{\partial E} dE \qquad (1\text{-}35)$$

 the derivation of transport parameters becomes easier.

There are several scattering processes with different relaxation time τ contribute to the total the scattering mechanism .According to Matthiessen's rule they all should be taken into account but to simplify the result we assume that one scattering process dominates in the relaxation time equation (1-17). Inserting (1-17) and (1-20) we may rewrite integral K_s as

$$K_s = \frac{8\pi}{3} \left(\frac{2}{h^2} \right)^{3/2} (m^*)^{1/2} T \tau_o \int_0^\infty E^{s+r+3/2} \frac{\partial f_o(E)}{\partial E} \qquad (1\text{-}36a)$$

$$K_s = \frac{8\pi}{3} \left(\frac{2}{h^2} \right)^{3/2} (m^*)^{1/2} T \tau_o \left(s + r + \frac{3}{2} \right) (k_B T)^{s+r+3/2} F_{s+r+3/2} \qquad (1\text{-}36b)$$

Where $F_n(\xi)$ is Fermi-Dirac integral defined as:

$$F_n(\xi) = \int_0^\infty \xi^n f_o(\xi) d\xi \qquad (1\text{-}37)$$

Here ξ is reduced energy and n can be integers or half integers. The expression for electrical conductivity and Seebeck coefficient in terms of integrals K_s is:

16

$$\sigma = \frac{1}{\rho} = \frac{e^2}{T} K_o \tag{1-38}$$

$$S = \pm \frac{1}{eT}\left(E_F - \frac{K_1}{K_o}\right) = \pm \frac{k_B}{e}\left[\xi_F - \frac{(r+5/2)F_{r+3/2}(\xi)}{(r+3/2)F_{r+1/2}(\xi)}\right] \tag{1-39}$$

For electrons E_F is measured upward from the bottom of the conduction band and S is negative.

For holes, E_F is measured downward from the top to the valence band and S is positive

Thus carrier concentration n (1-19) can be expressed in terms of reduced Fermi energy

$$n = \int_0^\infty f(E)g(E)dE = \frac{4}{\sqrt{\pi}}\left(\frac{2\pi m^* k_B T}{h^2}\right)^{3/2} F_{1/2}(\xi_F) \tag{1-40}$$

1.3.5 Nondegenerate and Degenerate Semiconductors

For nondegenerate semiconductors and considering the Fermi energy as variable quantity $E_F/kT \ll 1$, that is the Fermi energy lies in the forbidden gap well away from the band edge. The Fermi-Dirac integrals can be written as:

$$F_n(\xi) = \exp\left(\frac{E_F}{k_B}\right)\int_0^\infty \xi^n \exp(-\xi)d\xi = \exp(\xi)\Gamma(n+1) \tag{1-41}$$

where Γ is gamma funciton such that $\Gamma(n+1) = n!$ The electric conductivity and Seebeck coefficient under non degenerate condition in the terms of gamma function are:

$$\sigma = \frac{8\pi}{3}\left(\frac{2}{h^2}\right)^{3/2} e^2 (m^*)^{1/2} T \tau_o (k_B T)^{r+3/2} \Gamma\left(r + \frac{5}{2}\right)\exp(\xi) \tag{1-42}$$

$$S = \pm \frac{k_B}{e}\left[\xi - \left(r + \frac{5}{2}\right)\right] \tag{1-43}$$

$$n = \left(\frac{2\pi m^* k_B T}{h^2}\right)^{3/2}\exp(\xi) \tag{1-44}$$

The quantity $\left(\frac{2\pi m^* k_B T}{h^2}\right)^{3/2}$ is known as effective density of states. The mobility of charge carrier can be found using (1-42) and (1-44) in $\sigma = ne\mu$ and does not depend on the Fermi energy.

Considering the degenerate case $E_F/k_B T \gg 1$ the Fermi level is well above the conduction band edge for electrons or well below the valence band edge for holes. The Fermi-Dirac integrals are expressed as:

$$F_n(\xi) = \frac{\xi^{n+1}}{n+1} + n\xi^{n-1}\frac{\pi^2}{6} + n(n-1)\xi^{n-3}\frac{7\pi^4}{360} + \cdots \tag{1-45}$$

To solve it for electrical conductivity on the first term in the series is used. Thus we get:

$$\sigma = \frac{8\pi}{3}\left(\frac{2}{h^2}\right)^{3/2} e^2 (m^*)^{1/2} \tau_o \xi^{r+3/2} \tag{1-46}$$

The Seebeck coefficient requires the first two terms of the series because if only the first is used Seebeck would go to zero.

$$S = \mp\frac{\pi^2}{3}\frac{k_B}{e}\frac{(r+3/2)}{E_F/k_B T} \tag{1-47}$$

1.3.6 Thermal Conductivity

Heat transport is another key property of thermoelectric materials. Thermal conductivity κ indicates the ability of a material to conduct heat, and is often defined as heat q transmitted in time t through a distance L, in a direction normal to a surface of area A, due to temperature difference ΔT, Thus thermal conductivity can be expressed as[8]:

$$\kappa = \frac{q}{t}\frac{L}{A\Delta T} \tag{48}$$

According to classical theory κ is

$$\kappa = \frac{1}{3}C_v v^2 \langle\tau\rangle \tag{1-49}$$

where C_v is the specific heat, v is the velocity of propagation of elementary excitation such as electrons or phonons, $\langle\tau\rangle$ is its average relaxation time which is the time taken to travel a mean free path $l = v\langle\tau\rangle$.

18

Generally heat is transported by two mechanisms: phonons and thermalized electrons in the conduction band. Phonons are simply the quanta of lattice vibration. Total thermal conductivity is given as the sum of lattice conductivity κ_L and the part from electrons κ_e:

$$\kappa = \kappa_L + \kappa_e \tag{1-50}$$

1.3.7 Electronic Thermal Conductivity

The electronic component of the thermal conductivity is an important feature, especially in the case of heavily doped semiconductors ($n \sim 10^{19}\text{-}10^{20}\text{cm}^{-3}$). In the case of nondegenerate electron gas, Cv is given by

$$C_v = \frac{3}{2}nk_B \tag{1-51}$$

Here n is the carrier concentration and k_B is Boltzmann's constant. The electronic thermal conductivity is given as by

$$\kappa_e = \frac{1}{2}nv^2 k_B\langle\tau\rangle \tag{1-52}$$

The electrical conductivity of a semiconductor with a carrier concentration of n is related to carrier mobility $\mu = \frac{e\langle\tau\rangle}{m^*}$ by:

$$\sigma = ne\mu = ne^2\frac{\langle\tau\rangle}{m^*} \tag{1-53}$$

m^* is the effective mass of a carrier. From (1-53) we can rewrite κ_e in equation (1-52) as

$$\kappa_e = \left(\frac{1}{2}m^*v^2\right)\frac{k_B}{e^2}\sigma \tag{1-54}$$

The average kinetic energy of carriers is the thermal energy of $\left(\frac{3}{2}k_BT\right)$. Therefore, the electronic thermal conductivity is

$$\kappa_e = \frac{3}{2}\left(\frac{k_B}{e}\right)^2 \sigma T \tag{1-55}$$

19

This is the Wiedmann-Franz law often written $\kappa_e = L\sigma T$ where the term $\frac{3}{2}\left(\frac{k_B}{e}\right)^2$ is known as the

Lorentz number L, which is same for metals and nondegenerate (heavily doped) semiconductors.

The exact form of the electronic thermal conductivity κ_e in general can be derived from the

transport equations. Using (1-35) in (1-34) $\kappa_e = -\frac{w}{(\partial T/\partial x)}$ reduces to

$$\kappa_e = \frac{2}{3m^*T}\left\{\frac{\left[\int_0^\infty g(E)\tau E^2 \frac{\partial f_o(E)}{\partial E}dE\right]^2}{\int_0^\infty g(E)\tau E \frac{\partial f_o(E)}{\partial E}dE} - g(E)\tau E^2 \frac{\partial f_o(E)}{\partial E}dE\right\}$$

$$= \frac{1}{T^2}\left(K_2 - \frac{K_1^2}{K_o}\right) \tag{1-55}$$

k_e can be expressed in term of Lorentz number L defined as $k_e/\sigma T$. Then from (1-35) and (1-

55) it can be expressed as:

$$L = \frac{1}{e^2T^2}\left(\frac{K_2}{K_o} - \frac{K_1^2}{K_o^2}\right) \tag{1-56}$$

$$L = \left(\frac{k}{e}\right)^2\left\{\frac{\left(r+\frac{7}{2}\right)F_{r+5/2}(\xi)}{\left(r+\frac{3}{2}\right)F_{r+1/2}(\xi)} - \left[\frac{\left(r+\frac{5}{2}\right)F_{r+3/2}(\xi)}{\left(r+\frac{3}{2}\right)F_{r+1/2}(\xi)}\right]^2\right\} \tag{1-57}$$

For non-degenerate system the Lorentz number is given by[6]:

$$L = \left(r + \frac{5}{2}\right)\left(\frac{k_B}{e}\right)^2 \tag{1-58}$$

For strongly degenerate samples the Lorentz number is a universal constant, as derived above,

$$L = \frac{\pi}{3}\left(\frac{k_B}{e}\right)^2 = 2.45 \times 10^{-8}V^2/K^2 \tag{1-59}$$

1.3.8 Lattice Thermal Conductivity

A good approximation for the thermal conductivity of any heat conducting entity can be

derived from the classic kinetic theory. The lattice thermal conductivity is defined as:

$$k_l = \frac{1}{3}C_V v_s l \tag{1-60}$$

Here C_v is the specific heat capacity at constant volume, v_s is the sound velocity, and l is the phonon mean free path.

Eucken [17] pointed out at temperature greater than the Debye temperature k_l of a dielectric crystal is inversely proportional to the absolute temperature at high temperature. This rule is obeyed by a wide variety of crystals. Peierls[18] predicted that as the temperature is lowered below the Debye temperature, thermal conductivity should increase exponentially It is experimentally found that when temperature drops to about one-twentieth of the Debye temperature, the thermal conductivity reaches a maximum. At even lower temperature, lattice thermal conductivity varies with temperature T^3. Thus at very low temperature, the behavior of k_l dominated by the Debye T^3 law of C_v is given by:

$$\kappa_l = \frac{1}{3} C_v v l \approx \frac{1}{3} \left(\frac{T}{\theta_D}\right)^3 v l \qquad (1\text{-}61)$$

where θ_D is Debye temperature defined in terms of ω_D, the phonon cutoff frequency as $\theta_D = \frac{\hbar}{k_B}(\omega_D)^{1/3}$. In the low temperature regime, because of the limited number of excited phonons, the short wavelength phonon do not contribute to lattice thermal conductivity. At high temperature (above the Debye temperature), C_v approaches the classical value $3R$, making k_l primarily dominated by the behavior of mean free path l and short wavelength phonons are dominant.

1-4. Scattering Mechanisms

After knowing the expression for transport coefficients, the next step is to find suitable expressions for the relaxation time or scattering rate. There are various types of mechanisms such as electron-phonon scattering, static imperfection scattering and electron-electron scattering [19]. Once the scattering mechanism is identified the scattering rate can be easily found. The

scattering mechanism depends on type of obstacle whether it is charged impurity, neutral impurity, and grain boundaries inclusion and so on, so that the scattering rate varies with scattering mechanisms involved. Once the scattering rates are known, using results of Boltzmann equation, we can get final expression of thermal conductivity.

1.4.1 Electron Scattering

Electrons in solid can scatter by lattice defects, they can interact with each other to contribute to scattering or they can interact with phonons. The most important scattering in metals and semiconductors is electron-phonon scattering[19] and explains the temperature dependence of the resistivity (increases with increase in temperature and the mobility of semiconductor decreases with increasing temperature). In semiconductor Brillouin zone is mostly unoccupied whereas in metals, much of it is occupied by electrons. This large change in momentum is seen metal due to scatter because scattering takes place near Fermi surface. In semiconductors, small phonon wave vector participates in the scattering because changes in the electron wave vector takes place occur only at a small angle. At room temperature only, acoustic phonon scattering is dominant. The temperature dependent electron-phonon scattering rate in metals at high and low temperature is given as[19]:

$$1/\tau \sim T/\theta_D \qquad T \gg \theta_D \tag{1-62}$$

$$1/\tau \sim (T/\theta_D)^3 \qquad T \ll \theta_D \tag{1-63}$$

Bardeen and Shockley first developed relation of the relaxation time as function of energy [20, 21]

$$\tau \sim \frac{E^{-1/2}}{m^{*3/2}k_BT} \sim T^{-3/2} \tag{1-64}$$

1.4.2 Optical Phonon Scattering

Optical phonon is scattering is an elastic scattering and dominated at high temperature in polar semiconductors. When the interaction between the electrons or holes and the optical modes is not strong and with simplest assumption $T \gg \theta_D$, Howarth [22] finds the by approximation that at high temperature the scattering rate is varied with square root of energy given as

$$\tau_o \sim \frac{E^{1/2}}{m^{*1/2}T} \sim T^{-1/2} \qquad (1\text{-}65)$$

1.4.3 Phonon-Phonon Scattering

In most semiconductors, at high temperature region, phonons –phonon scattering is the most dominant scattering mechanism. This was Peierls [18] who showed that the most important processes are those that involve three phonons: either two phonons combine to create a third phonon or one phonon breaks up into two phonons These are called Normal and Umklapp process. In the so-called normal process, the energy and momentum are conserved in the collision. The wave vector of third phonon K_3 lies within the first Brillouin zone Fig 1-5 and consequently there is only redistribution of the phonons without introducing any resistance. On the contrary, in the Umklapp process only energy is conserved and momentum is not conserved so that this process is responsible for thermal resistance, even in defect free crystals. The wave vector of created phonon lies outside the first Brillouin zone Fig. 1-5 (B) and is physically equivalent to a point within the first Brillouin zone, and it can therefore be mapped back into the first Brillouin zone by the addition of a reciprocal lattice vector, **G**. Peierls's [18] theory predicted that k_l above Debye temperature should vary as $1/T$. Thus at high temperature regime Umklapps processes are the primary phonon scattering mechanism responsible for lowering the lattice thermal conductivity [23].

In an ideal harmonic lattice there is no coupling between the phonon modes and it is anharmonic part of the lattice that causes phonon-phonon collisions Keyes [24] using Lindemann melting rule[25] suggested a nifty, but, estimated, relation of lattice thermal conductivity as a function of density, atomic weight and melting temperature at high temperature.
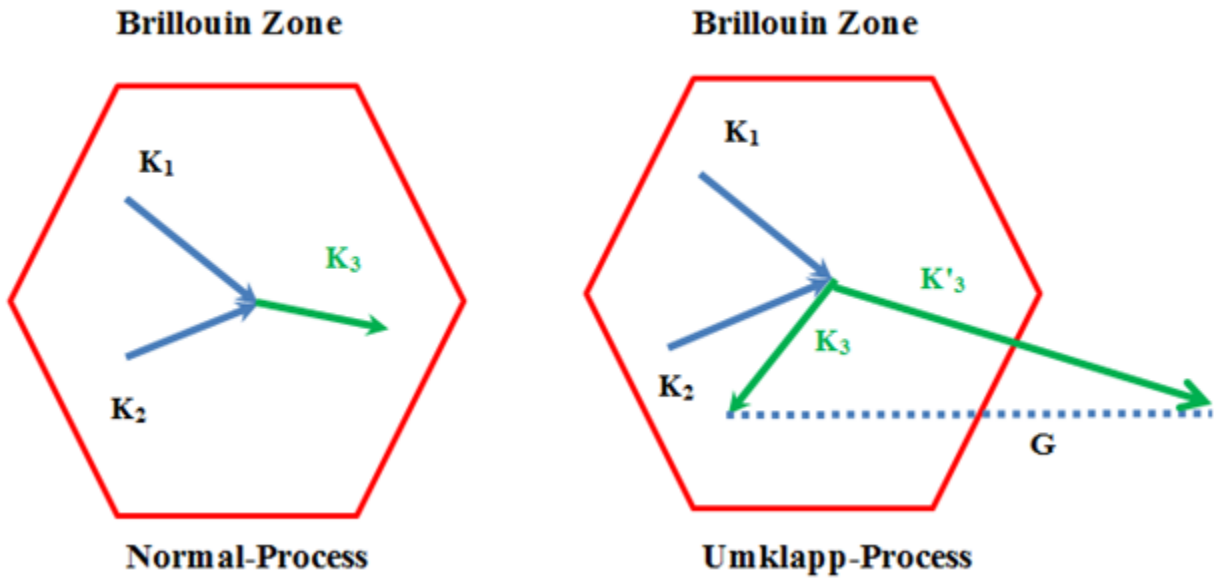
Figure:1-5 Phonon-Phonon Scattering(A) N-Process.K_3 lies within the first Brillouin zone (A) U Process G lies outside the first Brillouin zone

Keyes relation based on phonon-phonon scattering, at high temperature is given as:

$$k_l T = B \frac{T_m^{3/2} \rho^{2/3}}{A^{7/6}}$$
(1-66)

where $B = \frac{R^{3/2}}{3\gamma^2 \varepsilon_m^3 N_o^{1/3}}$ is a constant and useful for the approximate prediction of lattice thermal conductivity ,ρ is the density, T_m is the melting temperature, A is the mean atomic weight, R is the gas constant, ε_m is a constant which is mostly same for all material ,N_o is Avogadro's number and γ is the Gruneisen parameter
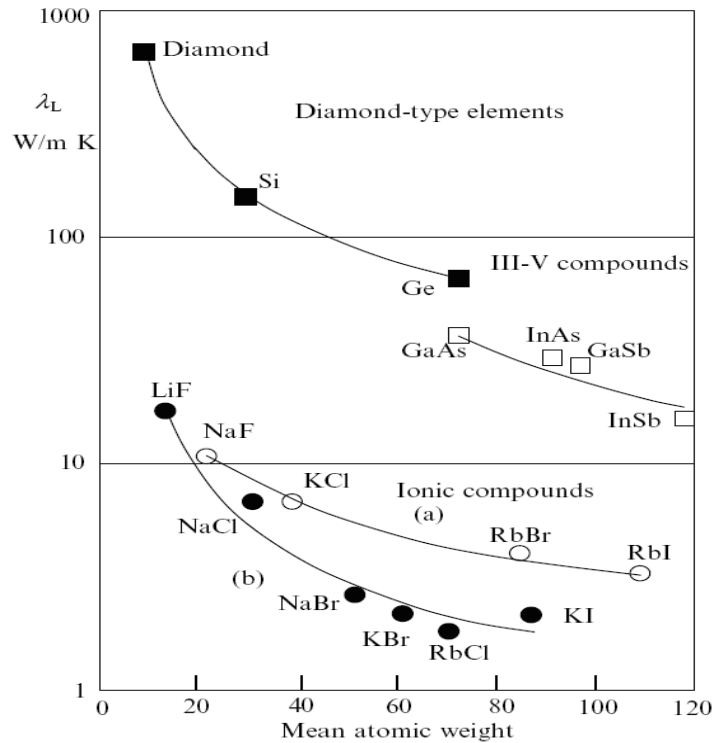
Figure:1-6 Lattice thermal conductivity varies as a function of mean atomic weight for ionic and covalent crystals[26, 27]

The Gruneisen parameter is one of the measures of the anharmonicity of the lattice vibrations. T_m, ρ and A are all easy to measure once the sample is made. The factor B in equation is independent of the material, which allows some conclusion for the thermal conductivity[26]:

1. In the high temperature range lattice thermal follows 1/T law.

2. A low melting point leads to a low thermal conductivity.

3. The proportionality to $\rho^{2/3}$ makes k_l low for crystal with large interatomic distances.

4. k_l falls off with increasing atomic weight and also falls with increasing ionicity of the bonds

As shown in Fig. 1-6 the lattice thermal conductivities of the ionic alkali halides are much lower than those of diamond-type elements and the III-V compounds [26]. This may

suggest that ionic compounds should have higher figure of merit than covalent semiconductors. But, covalent materials usually have high carrier mobility. It turns out the factor $(\mu m^{*3/2}/k_l)$ is highest for semiconductor in which covalent bonds dominate.

1.4.4 Umklapp Scattering

At the high temperature phonon-phonon Umklapp process dominates. Considering the second order perturbation theory, Sommerfeld estimated the relaxation time for Umklapp scattering τ_U at $T > 300$ K as [28]

$$\frac{1}{\tau_U} = 2\gamma^2 \frac{k_B T \omega^2}{\mu V_o \omega_D} \tag{1-67}$$

Where γ is the Gruneisen anharmonicity parameter, μ is the shear modulus, V is the volume per atom, ω_D is the Debye frequency.

1.4.5 Point Defects and Alloy scattering

A point defect simply implies that one of the atoms making up the crystal is different from all others such as show in Fig. 1-7. Also point defect scattering can have several origins and is high temperature mechanism so point defects can have little or no effect on long wavelength phonons, but high energy phonons (short wavelength phonons) are strongly scattered by point defects. Point defects are caused by an atom with mass different from the host atoms (isotopes, solid solutions, alloys, or lattice vacancies) is of highly important point defect in thermoelectric material. This is called mass fluctuation defect. The phonon travels with little or no scattering when the lattice is uniform but the lattice has lots of defects, anharmonic phonon-phonon scattering is stronger because the bonding in the crystal is disturbed. It was suggested that at high temperature the formation of a solid solution or alloy could lead to a stronger scattering of phonons than of the electrons, which could improve the ratio of mobility to lattice thermal

26

conductivity and is of significant importance in the improvement of performance of thermoelectric materials [16].
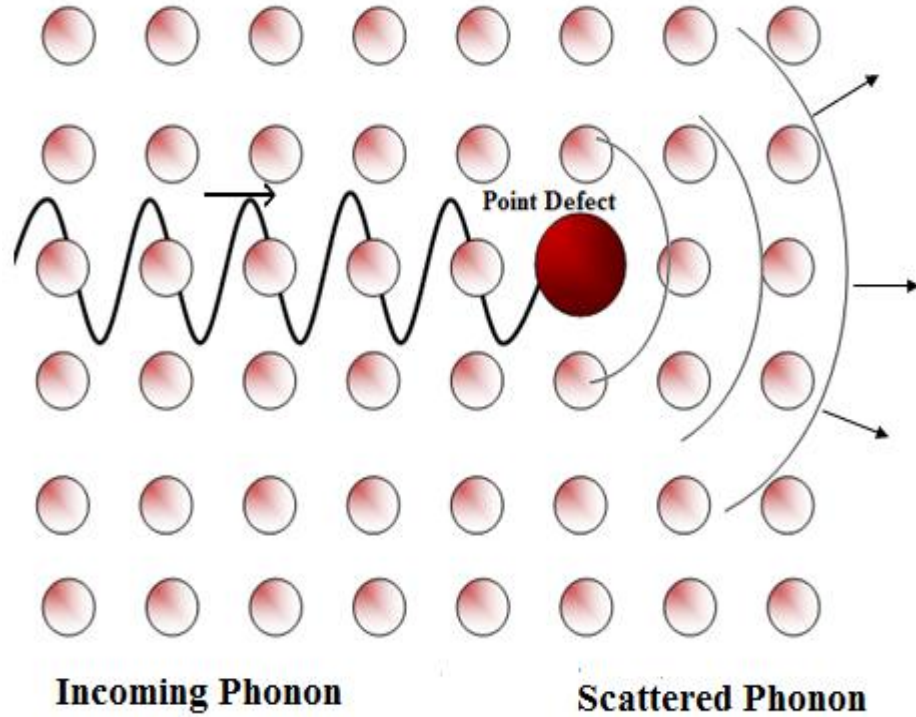
Figure 1-7: A point defect scatters an incoming phonon into spherical phonons.

Rayleigh scattering is expected for frequencies that are small compared to the defect. It is assumed in the Rayleigh scattering when the scattering cross-section σ_{scatt} changes with density the scattering cross section for point defect is given according to relation:

$$\sigma_{scatt} \propto c^6 q^4 \left(\frac{\Delta\chi}{\chi} + \frac{\Delta\rho}{\rho}\right)^2 \tag{1-68}$$

Here c is the linear dimension of the defect, q the magnitude of the wave vector for a given phonon, $\Delta\chi$ is the local change in compressibility and $\Delta\rho$ is the local change in density.

The relaxation time τ_{point} at high temperature for scattering on point defects can be expressed in terms of phonon frequency ω [26]:

$$\frac{1}{\tau_{point}} = \frac{V_o \Gamma \omega^4}{4\pi v^3} \tag{1-69}$$

where V_o is the cube root of atomic volume. The sound velocity v is assumed to be given by Debye expression and Γ is the disorder parameter. Alloy scattering is utilized in almost all of the important thermoelectric a materials as a method of lowering the lattice thermal conductivity.

1.4.6 Boundary Scattering

There are various types of defects of geometrical obstacles such inclusions voids which are situated at grain boundaries and thereby take part in scattering mechanism The scattering rates due to grain boundary defects can be estimated very much as suggested in Fig 1-8

Scattering rate = Number of particles which hit an obstacle/second,

$$\frac{1}{\tau} = N v \pi r^2 \tag{1-70}$$

The scattering rate depends both on properties of the carrier as well on properties of the defects present at the grain boundary. Boundary scattering has been known to be effective in reducing lattice thermal conductivity. Therefore lattice thermal conductivity is expected to be reduced by introducing interfaces by pressing a micro- or nanosized powder into pellet. It is also noted the thermal conductivity is reduced at low temperatures by boundary scattering where other scattering mechanisms are generally weak.

However it has been investigated that boundary scattering might be important in thermoelectric materials at normal temperatures and high temperatures in highly disordered materials[29].

Figure 1-9 shows different scattering mechanism contributing to the thermal conductivity of a large pure crystal. The area within dotted red curve shows schematically the reduction of thermal conductivity by point defect scattering. The area within blue dots indicates the reduction due to the boundary scattering. This means in this region much of the heat is transported by low
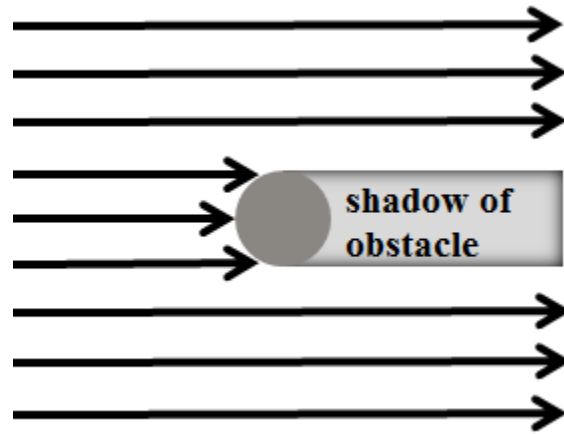
Figure:10-8 Stream of *N*/cm³ particles moving with velocity *v* cm/s. Obstacle casts shadow of area =π*r* ²
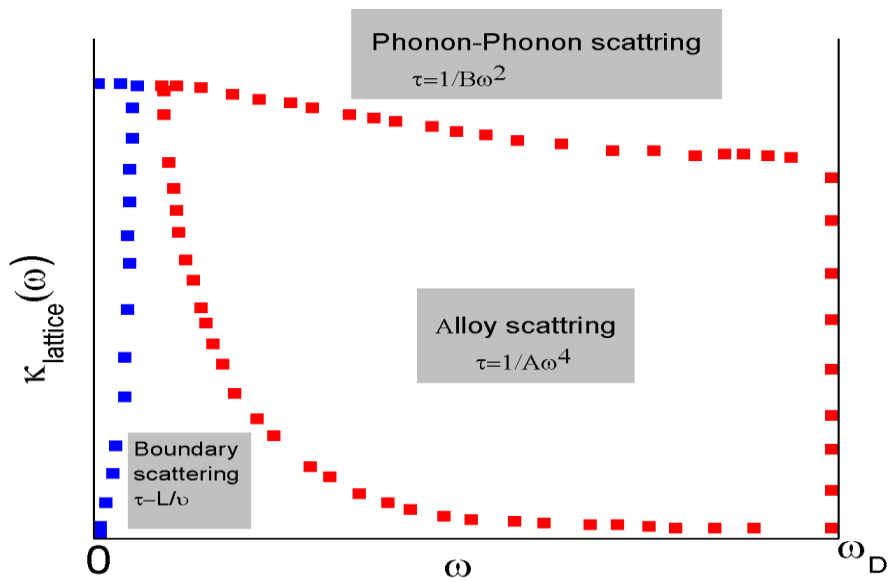
Figure: 1-9 Contribution to thermal conductivity from various parts of phonon spectrum against phonon frequency[29].

frequency phonons because the low frequency phonons have a much longer mean free path and. can be easily scattered by boundaries The combined effect of phonon-phonon and alloy scattering makes boundary scattering significant at high temperature. Thus in solid solution it is possible to improve the thermoelectric figure of merit by boundary scattering because the high frequency phonons are strongly scattered thus removing the contribution by alloy scattering and increasing boundary scattering effect

1.5 Factors Relating to Optimizing Electron Transport Properties

The challenge in any effort to discover new thermoelectric (TE) materials lies in achieving simultaneously high electronic conductivity, high thermoelectric power, and low thermal conductivity. These quantities together define the figure of merit of materials. These quantities are determined by electronic structure and scattering of charge carriers thus are not independently controllable parameters. Therefore there seems to be various possible ways to enhance *ZT*. One approach involves optimizing the properties of material and then optimizes reduced Fermi energy. Using the result of classical approximation for semiconductor (1-43) and (1-44) *ZT* can be expressed as function of reduced Fermi energy [6]

$$ZT = \frac{S^2}{L + \kappa_l / ne\mu T} = \frac{\left[\eta - (r + \frac{5}{2})\right]^2}{(\beta exp\xi)^{-1} + (r + \frac{5}{2})} \tag{1-71}$$

Here the quantity β which is introduced by Chasmar and Stratton [30] is material parameter and defined as:

$$\beta = \left(\frac{K}{e}\right)^2 \frac{\sigma_o T}{\kappa_l} = 5.74 \times 10^{-4} (\mu/k_l)(m^*/m_e)^{3/2} T^{5/2} \tag{1-72}$$

where $\sigma_o = 2e\mu \left(\frac{2\pi m^* kT}{h^2}\right)^{3/2}$ is the reduced electrical conductivity.

30

To maximize *ZT* for a given material one must first calculate β to determine the optimum

value of ξ. Then adjust ξ so that $\xi = \xi_o$ this may be achieved by doping with suitable impurities.

The doping changes ξ_o significantly the corresponding change in β is negligible unless the

material is very heavily doped resulting in significant change in the band structures or mobility.

The optimum value of reduced Fermi energy is obtained by setting $\frac{dZ}{d\xi} = 0$. This gives:

$$\xi_o + 2\left(r + \frac{5}{2}\right)\beta exp\xi_o = r + \frac{1}{2} \tag{1-73}$$

Equation 1-72 shows that at any particular temperature β is proportional to

$\mu(m^*/m_e)^{3/2}/\kappa_l$ this shows that the preferred semiconductors are those with high carrier

mobility, large effective mass and low thermal conductivities. According to equation 1.13

optimization of figure of merit *ZT* depends upon also on maximizing power factor and

minimization thermal conductivity. Power factor becomes small when the Fermi level too far

into the forbidden gap of a semiconductor[6]. Thus Seebeck coefficient and electrical

conductivity can be tuned via optimizing carrier concentration, Figure 1-10 shows the

optimization of *ZT* through carrier concentration tuning [32]. Maximizing the efficiency *ZT* of a

thermoelectric involves a compromise of thermal conductivity and Seebeck coefficient with

electrical conductivity. It is noted from Fig 1-10 that when *n* is too large *ZT* drops down

drastically due to decease in Seebeck coefficient and large electronic thermal conductivity Thus

there is a limit where modification of any three thermoelectric parameters *S*. σ and κ adversely

influences the other transport coefficients so that thermoelectric figure of merit does not vary

much.

It is seen that optimum thermoelectric figure of merit is obtained for typically heavily

doped semiconductors with a carrier concentration between 10^{19} and 10^{21} carriers per cm^3.Jonker
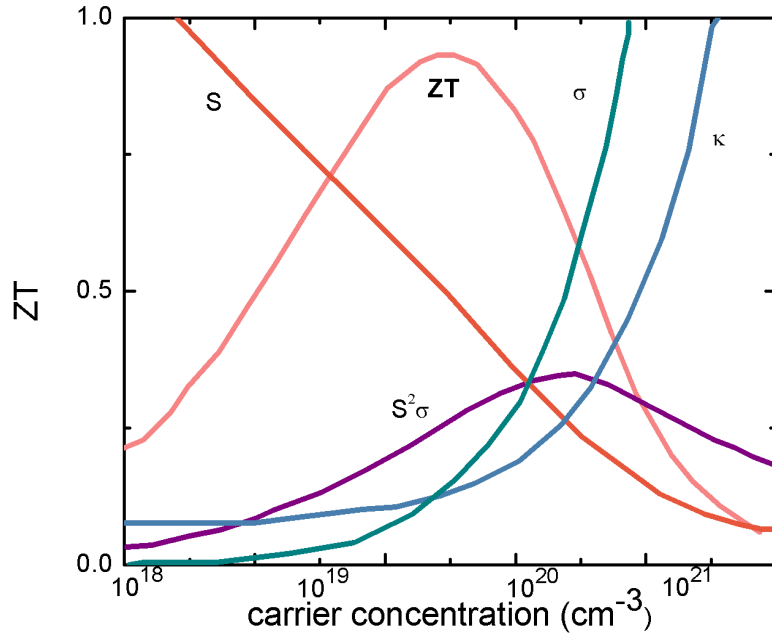
Figure:0-10 Dependence of thermoelectric transport parameters on carrier concentration

Table 2. Comparison at room temperature of the thermoelectric properties of metals semiconductors and insulators[31].

TE Parameters	Metals	Semiconductors	Insulators
S (VK^{-1})	5×10^{-6}	200×10^{-6}	1000×10^{-6}
$\sigma=ne\mu$ $(\Omega\text{-m}^{-1})$	10^{8}	10^{5}	10^{-10}
$\kappa=\kappa_e+\kappa_l$ $(Wm^{-1}K^{-1})$	$\kappa=\kappa_e+\kappa_l\approx\kappa_e$ 10-100	$\kappa=\kappa_e+\kappa_l;\kappa_e<\kappa_l$ 1-100	$\kappa=\kappa_e+\kappa_l;\approx\kappa_l$ 0.1-1
ZT	$\approx10^{-3}$	$\approx0.1\text{-}1.0$	$\approx10^{-14}$

has also demonstrated by plotting Seebeck coefficient as a function of the carrier concentration

and showed Seebeck coefficient drops at the insulator regime and therefore insulators are not

good thermoelectric materials [33]. Table 2 explain how rapid change in thermoelectric effects changes from metals to insulators because of the thermoelectric properties dependence on carrier concentration.

1.6 Search for High Performance Thermoelectric Materials

As explained above semiconductors appear to be the materials of choice for exploring high performance thermoelectric material. These materials with superior performance have attracted great attention from academic research perspective as well as with industrial application. There is a challenge to develop thermoelectric materials with high dimensionless figure of merit to customize the interrelated thermoelectric parameters for crystalline structures. Various approaches have been adopted to enhance ZT. Transport theory (1-70) shows ZT depends upon the reduced Fermi energy, scattering parameter the reduced. The reduced Fermi energy can be optimized by creating heavily doped semiconductors with optimized carrier concentration of about 10^{18} to 10^{20}/cm^3[34].

The interrelation of transport parameters to optimize the figure of merit is non-trivial and most of thermoelectric research is extensively focused on improving the thermopower and electrical conductivity by judicious doping of promising materials. This approach is reasonably effective for improving temperature dependent power factor but difficulty crops up in maximizing ZT because of the thermal conductivity of material. Any attempt to maximize electrical conductivity ends up in corresponding rise in the thermal conductivity.

Another approach is to fabricate compound with large number of atoms in the unit cell to decouple the interrelated parameters. The large number of atoms in unit cell lowers the fraction of vibration modes (phonons) that carry heat efficiently (acoustic modes). This lowers lattice thermal conductivity and ZT can be enhanced [35]. There are various materials which have large

and complex structures and can be most promising material to be used as thermoelectric materials. Zintl compounds [36] with a large unit cell, including $Yb_{14}MnSb_{11}$, $Yb_{11}GaSb_9$, $Ca_{11}GaSb_9$and $SrZnSb_2$ have been revealed to possess an intrinsically low lattice thermal conductivity due to the high fraction of low-velocity optical phonon modes [37]. To enhance *ZT* by minimizing lattice thermal conductivity is most extensively explored in phonon glass electronic crystals (PGEC) where the naming implies desirable thermoelectric material would act as glass with respect to phonon but as a crystal with respect to electrons and holes. In these compounds rattling motion of loosely bonded atoms within a large cage generates strong scattering against lattice phonon propagation but has less impact on the transport of electrons. skutterudites [38, 39] and clathrates [40] are examples of highly motivated PGEC materials in which thermal conductivity can be reduced greatly while maintaining the electric conductivity at a highly level. Chalcogenides are sulfides, selenides, and tellurides and show semiconducting behavior. Commercially chalcogenides are the most generic materials such as Bi_2Te_3 and its solid solution $Bi_2Te_{3-x}Se_x$ and $Bi_{2x}Sb_x$[6],Te_x PbTe and TAGS (Te-Ag-Ge-Sb)[41] are among the most demanding thermoelectric materials.

As seen in section 1.2.2 device equations (1-90) and (1-10) do not show on any dependence on dimensionality. Thus to crack the bottleneck of improvement of figure of merit low dimensional material can be good choice. Dresselhaus et al. suggested that the power factor can be enhanced through the use of quantum confinement effects[9]. As the system size decreases and come close to a nanometer scale the density states of various low dimensional systems splits and becomes narrow and increases the power factor. Substructure approach is another effective enhance performance by increasing the complexity. It is identified that interfaces between dissimilar materials within a thermoelectric device can scatter phonon and so

thermoelectric materials composed of layers of different materials stacked on top of each other reduces compared to bulk materials and consequently Z is enhanced. Venkatasubramanian and his co-workers have reported high ZT value ~ 2.4 for p-type Bi_2Te_3/Sb_2Te_3 superlattice[42]. Figure 1-11 shows ZT of recent high performance bulk thermoelectric materials as a function of applied temperature.

1.7 Objective of the Work

Half Heusler materials of ZrNiSn base system have drawn attention as a promising thermoelectric materials because of their semiconductor like band structures[43-45]. These values the electrical resistivity are of an order of magnitude state of art material and exhibit large Seebeck coefficient[46, 47]. There is a scope of optimizing the thermoelectric properties by alloying at Ni site to enhance figure of merit of these material. One of the motives for this thesis is to synthesize half-Heusler $Zr_{0.5}Hf_{0.5}Ni_{1-x}Pd_xSn_{0.99}Sb_{0.01}$ by solid state reaction. It is well known that presence of nano sized oxides serving as thermoelectric materials have special advantages such as n type oxides exhibit relatively low thermoelectric performance as compared to p-type NiO is p-type refractory material and HfO_2 is n-type. We will incorporate nanometer-sized NiO and HfO_2 into $Zr_{0.5}Hf_{0.5}Ni_{1-x}Pd_xSn_{0.99}Sb_{0.01}$ matrices having the superior transport properties and compare the role of these oxides in half-Heusler.
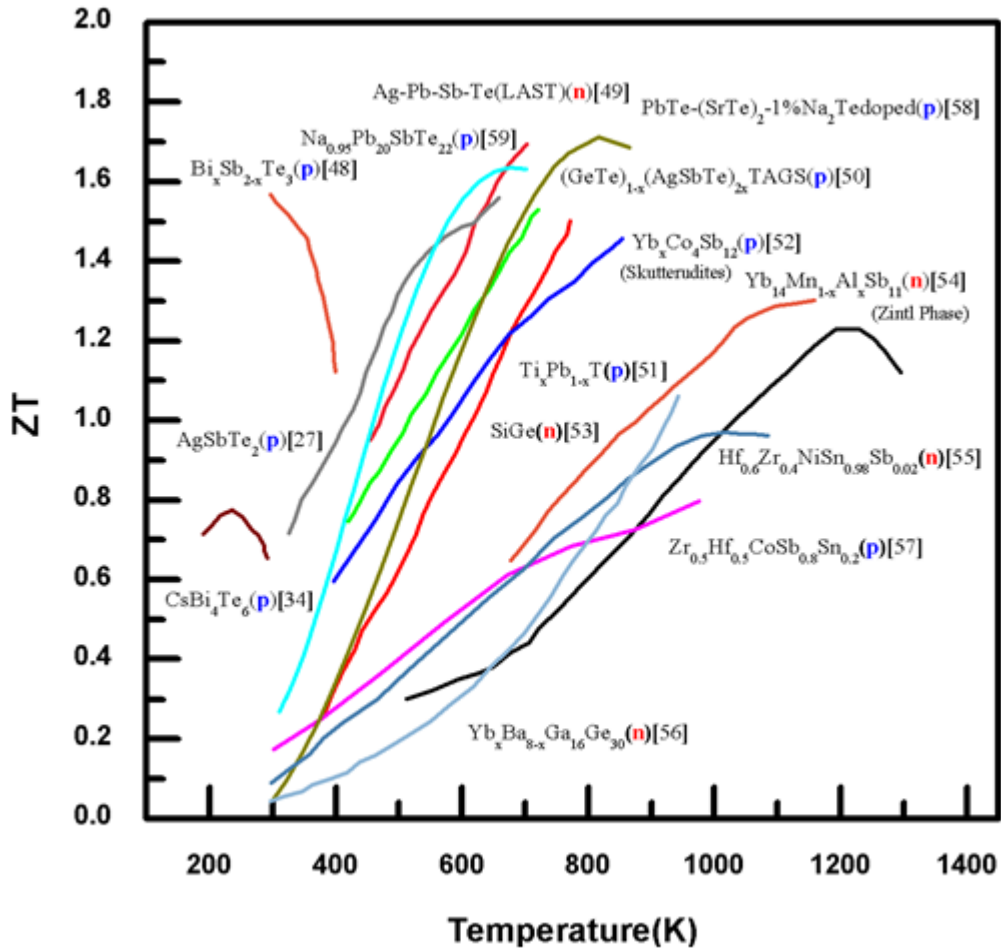
Figure:1-11 Figure of merit of high performance bulk thermoelectric materials [27, 34, 48-59]

1.8 Reference

[1]   B. C. Sales, Science 295 (2002) 1248.

[2]   T. J.Seebeck., Abh. Koenigl, Akad. Wiss. Berlin (1822) 265.

[3]   J. C. Peltier, Ann. Chim LVI (1834) 371.

[4]   E. Altenkirch, Physics, Z 10 (1909) 560.

[5]   E. Altenkirch, Physics, Z. (1911) 920.

[6]   G. S. Nolas, J.Sharp, and J. Goldsmid, Thermoelectrics: Basic Principles and New Materials Developments, Springer, 2001.

[7]   M. S. Dresselhaus, G. Chen, M. Y. Tang, R. G. Yang, H. Lee, D. Z. Wang, Z. F. Ren, J. P. Fleurial, and P. Gogna, Advanced Materials 19 (2007) 1043.

[8]   D. M. Row, CRC Handbook of Thermoelectrics, CRC-Press, 1995.

[9]   L. D. Hicks and M. S. Dresselhaus, Physical Review B 47 (1993) 12727.

[10]   G. Chen, Physical Review B 57 (1998) 14958.

[11]   R. Venkatasubramanian, E. Silvola, T. Colpitts, and B. O'Quinn, Nature 413 (2001) 597.

[12]   T. C. Harman, P. J. Taylor, M. P. Walsh, and B. E. LaForge, Science (2002)

[13]   W. Thomson, in Proceeding Royal Society, Vol. 91, Edinburgh, 1851.

[14]   H. Reiss and G. J. M. Koper, The Journal of Physical Chemistry 99 (1995) 7837.

[15]   A. F. Ioffe, L. S. Stil'bans, E. K. Iordanishvili, and T. S. Stavitskay, Semiconductor Thermoelements and Thermoelectric Cooling, London, 1957.

[16]   H. J. Goldsmid, Electronic Refrigeration, Pion Ltd., London, 1986.

[17]   A. Eucken, Ann Physik (1911)

[18]   R. E. Peierls, Ann. Physik 3 (1929) 1055.

[19]   J. F. Nye, Physical properties of crystals, Clarendon Press, 1979.

[20]   J. Bardeen and W. Shockley, Physical Review 80 (1950) 72.

[21]   J. Bardeen and W. Shockley, Physical Review 80 (1950) 69.

[22]   D. J. Howarth and E. H. Sondheimer, Proceedings of the Royal Society of London. Series A. Mathematical and Physical Sciences 219 (1953) 53.

[23]   C. Uher, in Thermal Conductivity: Theory, Properties, and Applications (M. T. Terry, ed.), Kluwer Academic / Plenum Publishers, New York, 2005, p. 312.

[24]   R. W. Keyes, Physical Review 115 (1959) 564.

[25]   F. A. Lindemann, Physik,Z. 11 (1910) 609.

[26]   H. Julian Goldsmid, Introduction to Thermoelectricity, Springer, 2009.

[27]   H. Wang, J.-F. Li, M. Zou, and T. Sui, Applied Physics Letters 93 (2008) 202106.

[28]   A. Sommerfeld, Z. Physics 47 (1928)

[29]   H. J. Goldsmid and A. W. Penn, Physics Letters A 27 (1968) 523.

[30]   R. P. Cahsmar and R. Stratton, Journal of Electron Control 7 (1959) 52.

[31]   J. P. Fleurial, http://materialsforenergy.typepad.com.

[32]   G. J. Snyder and E. S. Toberer, Nat Mater 7 (2008) 105.

[33]   G. H. Jonker, Vol. 23, 1968, p. 131.

[34]   E. S. Toberer, C. A. Cox, S. R. Brown, T. Ikeda, A. F. May, S. M. Kauzlarich, and G. J. Snyder, Advanced Functional Materials 18 (2008) 2795.

[35]   G. A. Slack, Nature Publishing Group, 1995, p. 407.

[36]   S. M. Kauzlarich, S. R. Brown, and G. Jeffrey Snyder, Dalton Transactions (2007) 2099.

[37]   E. S. Toberer, A. F. May, and G. J. Snyder, Chemistry of Materials 22 (2009) 624.

[38]   B. C. Sales, D. Mandrus, and R. K. Williams, Science 272 (1996) 1325.

[39]   G. S. Nolas, D. T. Morelli, and T. M. Tritt, Annual Review of Materials Science 29 (1999) 89.

[40]   G. S. Nolas, J. L. Cohn, G. A. Slack, and S. B. Schujman, Applied Physics Letters 73 (1998) 178.

[41]   T. D. S. Skrabek E A, CRC Handbook of Thermoelectrics (1995) 267.

[42]   R. Venkatasubramanian, E. Siivola, T. Colpitts, and B. O'Quinn, Nature 413 (2001) 597.

[43]   S. Ogut and K. M. Rabe, Physical Review B 51 (1995) 10443.

[44]   P. Larson, S. D. Mahanti, S. Sportouch, and M. G. Kanatzidis, Physical Review B 59 (1999) 15660.

[45]   H. Hohl, A. P. Ramirez, C. Goldmann, G. Ernst, B. Wolfing, and E. Bucher, Journal of Physics: Condensed Matter 11 (1999) 1697.

[46]   F. G. Aliev, N. B. Brandt, V. V. Moshchalkov, V. V. Kozyrkov, R. V. Skolozdra, and A. I. Belogorokhov, Zeitschrift für Physik B Condensed Matter 75 (1989) 167.

[47]   F. G. Aliev, V. V. Kozyrkov, V. V. Moshchalkov, R. V. Scolozdra, and K. Durczewski, Zeitschrift für Physik B Condensed Matter 80 (1990) 353.

[48]   D.-Y. Chung, T. Hogan, P. Brazis, M. Rocci-Lane, C. Kannewurf, M. Bastea, C. Uher, and M. G. Kanatzidis, Science 287 (2000) 1024.

[49]   W. Xie, X. Tang, Y. Yan, Q. Zhang, and T. M. Tritt, Applied Physics Letters 94 (2009) 102111.

[50]   K. F. Hsu, S. Loo, F. Guo, W. Chen, J. S. Dyck, C. Uher, T. Hogan, E. K. Polychroniadis, and M. G. Kanatzidis, Science 303 (2004) 818.

[51]   S. H. Yang and et al., Nanotechnology 19 (2008) 245707.

[52]   J. P. Heremans, V. Jovovic, E. S. Toberer, A. Saramat, K. Kurosaki, A. Charoenphakdee, S. Yamanaka, and G. J. Snyder, Science 321 (2008) 554.

[53]   Z. Xiong, X. Chen, X. Huang, S. Bai, and L. Chen, Acta Materialia 58 (2010) 3995.

[54]   X. W. Wang, H. Lee, Y. C. Lan, G. H. Zhu, G. Joshi, D. Z. Wang, J. Yang, A. J. Muto, M. Y. Tang, J. Klatsky, S. Song, M. S. Dresselhaus, G. Chen, and Z. F. Ren, Applied Physics Letters 93 (2008) 193121.

[55]   C. Yu, T.-J. Zhu, R.-Z. Shi, Y. Zhang, X.-B. Zhao, and J. He, Acta Materialia 57 (2009) 2757.

[56]   X. Tang, P. Li, S. Deng, and Q. Zhang, Journal of Applied Physics 104 (2008) 013706.

[57]   X. Yan, G. Joshi, W. Liu, Y. Lan, H. Wang, S. Lee, J. W. Simonson, S. J. Poon, T. M. Tritt, G. Chen, and Z. F. Ren, Nano Letters 11 (2011) 556.

[58]   K. Biswas, J. He, Q. Zhang, G. Wang, C. Uher, V. P. Dravid, and M. G. Kanatzidis, Nat Chem 3 (2011) 160.

[59]   P. F. P. Poudeu, J. D'Angelo, A. D. Downey, J. L. Short, T. P. Hogan, and M. G. Kanatzidis, Angewandte Chemie-International Edition 45 (2006) 3835.

CHAPTER 2

CHARATERIZATION OF THERMOELECTRIC MTERIALS

2.1 Introduction

In order to integrate new materials into technological devices, the materials have to be characterized both qualitatively and quantitatively. The materials properties and performance depend on the crystal structure and chemical composition of the material. Hence, materials have to be characterized using various characterization tools. Crystal structure analysis can be extensively carried out by X-ray diffraction (XRD) methods, from basic phase identification to information on atomic positions, bonding etc. The chemical composition and microstructural features of the bulk material and interfaces can be obtained by Scanning/Transmission electron microscopy (SEM, TEM). A more detailed analysis on composition of the materials can be achieved from energy dispersive X-ray method (EDAX), which is integrated in SEM/TEM devices. The above mentioned methods are the basic characterization required for any material, but for thermoelectric materials the electronic; phonon transport characterization is the most essential. In this chapter we will describe the technique and instrumentation used for characterization of thermoelectric material.

After consolidation phase identification and crystallite size were obtained from powder-X-ray diffraction (PXRD).The structure and morphology was identified using Scanning election microscopy. Energy Dispersive X-ray spectroscopy (EDS) was used to determine the chemical composition. Electrical conductivity and Seebeck coefficient were also measured from room temperature to 500°C using a commercial instrument. Room temperature Hall effect measurements were performed to obtain carrier concentration and carrier mobility. The thermal

conductivity was measured indirectly using a laser-flash diffusivity technique. Structural, electrical and thermal properties characterization principles, techniques and instrumentation are described below.

2.2 Powder X-ray Diffraction

After synthesis phase identification and structural analysis of the material is the most important part of characterization. X-ray techniques uses X rays which are form of electromagnetic radiation of very short wavelength with typical energies in the ranger of 100ev - 100ev were discovered by Dr. Roentgen[1]. The wavelength of the X-rays is comparable to the size of atoms. The elastic scattering made by the interactions between X-ray and electrons of atoms in the material is used for probing the structural arrangement of atoms and molecules in powder X-ray.

Powder X-ray diffraction (PXRD) is one of the methods employed most extensively used tool to identify phases and atomic structure of the material. The peak identification is performed by checking updated libraries of powder diffraction patterns such as ICS (the inorganic Crystal Structure Data base) or ICDD (the international Center for Diffraction Data). The PXRD is useful for qualitative analysis and checking the purity of the sample approximately. However it cannot detect an amorphous phase or impurities of less than about 5%. Powder diffraction can be used to solve crystal structure with simple and high symmetry. It may be difficult to index overlapping peaks if the structure is complex.

2.2.1Principle and Uses

The principle of X-ray diffraction is very straightforward. A thin layer of crystalline material sample irradiated with X-rays at an angle θ and diffraction occurs when the distance by

rays reflected from successive planes differs by an integral multiple of wavelength of X-ray beam. Thus detector records the diffracted intensity as a function of an angle. Figure 2-1
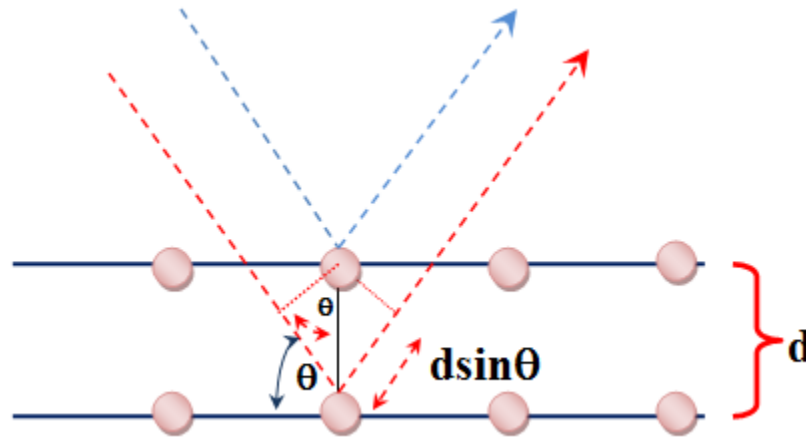
Figure: 2-1 X-ray diffraction from lattice planes.

illustrates the principle of X-ray diffraction. By changing the angle Bragg's condition is satisfied which is given by the formula

$$n\lambda = 2dsin\theta \tag{2-1}$$

where d is the spacing between the planes, n is an integer and λ is the wavelength of X-ray.

Since the peak positions in the Powder X-ray Diffraction (PXRD) pattern are related to the unit cell parameters as well as d values, and the intensities of the peaks are proportional to the square of atomic number of elements, i.e. the total number of electrons. The PXRD pattern can be regarded as the fingerprint for a material. The position and integrated intensities of a set of peaks in an X-ray powder diffraction pattern are compared to data base of known materials in order to identify the contents of the sample and to determine the presence or absence of any particular phase. Based the principle of X-ray crystalline size is determined from peak

broadening. According to Debye-Scherrer's equation crystalline dimension L is related to peak broadening β by[2]

$$\beta_l = \frac{K\lambda}{Lcos\theta} \tag{2-2}$$

where β_l is the line broadening due to the effect of small crystallites and is given by

$$\beta_l = \beta_{Obs} - \beta_{inst} \tag{2-3}$$

β_{Obs} being the breadth of the observed diffraction line at its half intensity maximum and β_{instr} is the instrumental broadening or β_l must be given in radians, K is shape factor which usually takes value of 0.9 [1].

The strain in a material produces two defects macro stress and micro strains. The contribution of these to particle size in Scherrer's formula must be subtracted. In micro strain, unit cell distances are increased due to uniform strains and result a peak shift. Micro strains produce peak broadening due to distribution of both tensile and resulting forces. Both effects produce symmetrical broadening. The peak broadening due to stress is related to residual strain ε by Stokes and Wilson formula:

$$\beta_\varepsilon = 4\varepsilon tan\theta \tag{2-4}$$

β_ε is the broadening of an observed diffraction peak caused by stress

To do an accurate analysis for size one must accurately account for instrumental, and strain broadening by assuming Gaussian or Lorentzian functions for both strain and size.

For Lorentzian observed broadening in peak is given as:

$$\beta_{Obs} = \beta_l + \beta_\varepsilon + \beta_{inst} \tag{2-5}$$

$$\beta_{Obs} - \beta_{inst} = \beta_l + \beta_\varepsilon \tag{2-6}$$

For Gaussian

$$\beta_{obs}^2 = \beta_l^2 + \beta_\varepsilon^2 + \beta_{inst}^2 \qquad (2\text{-}7)$$

$$\beta_{obs}^2 - \beta_{inst}^2 = \beta_l^2 + \beta_\varepsilon^2 \qquad (2\text{-}8)$$

Substituting (2-2) and (2-4) we get an equation to make Williamson-Hall plot[3] for Lorentzian peak.

$$\beta_{Obs} - \beta_{inst} = \frac{K\lambda}{Lcos\theta} + 4\varepsilon tan\theta \qquad (2\text{-}9)$$

Williamson-Hall plot is drawn by taking $(\beta_{Obs} - \beta_{inst})cos\theta$ on the y-axis (in radians) and $4cos\theta$ on the x-axis. The crystallite size and strain are evaluated from the linear regression Williamson–Hall plot such that y-intercepts of the linear fit give crystalline size and slope of the curve gives strain.

The Powder XRD of all samples in this study were recorded on PANalytical XPert Pro diffractometer using monochromatic CuKα radiation (λ=0.15406nm for the K_α characteristic line) with 2θ scanning range of 15-75˚ in steps of 0.05˚ and at rate of five seconds per step. The tube setting of 45 kV and 45 mA was used. PXRD was measured on the loose powder before consolidation and after consolidation. The phase and peaks identification was done by using software XPert High Score Plus which is supported with multiple reference databases.

2.3 SEM

The scanning electron microscope (SEM) is one of the most frequently useful investigative tools to analyze surface topography which texture features, material properties morphology and compositional differences by images of high magnification. The surface of material is scanned with beam of high energy electrons. The SEM signal includes secondary electrons, back scattered electrons (BSE) characteristic X-rays, light specimen current and transmitted electrons[4]. These types of signals all require specialized detectors. In most standard

detection mode, secondary electron imaging or SEI, the SEM can produce very high resolution images of sample surface, revealing details about 1 to 5 nanometers in size.

Backscattered electrons (BSEs) are electrons when the incident beam undergo elastic interactions with the sample, change trajectory, and escape the sample. These backscattered electrons are emitted by at high beam voltage, and their average energy is much higher than that of the secondary electron image(SEI) The intensity of the BSE signal is a function of the average atomic number (Z) of the specimen, with heavier elements (higher Z samples) producing more BSEs. It is thus a useful signal for generating compositional images, in which higher Z phases appear brighter than lower Z phases. The back scattered images of half Heuslers and their composites were taken when doomed to necessary by using conventional SEM.

2.4 EDX

Energy Dispersive X-ray analysis (EDX) is an ideal analytical technique used for both qualitative and quantitative analysis of the elements present in material over wide ragen.EDX is usually integrated with Scanning Electron Microscopy (SEM). When a high-energy electron beam (usually 10-20 kV) hits an atom of the sample, inner shell electrons of the atom within the sample are knocked out, as shown in Figure 2.2. The ejected electrons leave behind holes which are then filled with outer shell electrons of the same atom. The energy difference between the respective shells is emitted as X-rays, which have wavelengths specific to each element. This is the so-called characteristic X-ray. The energy of the emitted X-rays is measured by X-ray detector allowing the identification of the element. The intensities of the peaks in the EDX spectrum represent the concentration of the related element in the tested sample. By calculating the area under the peaks of each identified element (while considering the accelerating voltage of

46

the beam), quantitative analysis can be performed. In this research work EDX analysis on some

samples was performed using a JSM-5410 SEM integrated with EDX analyzer.
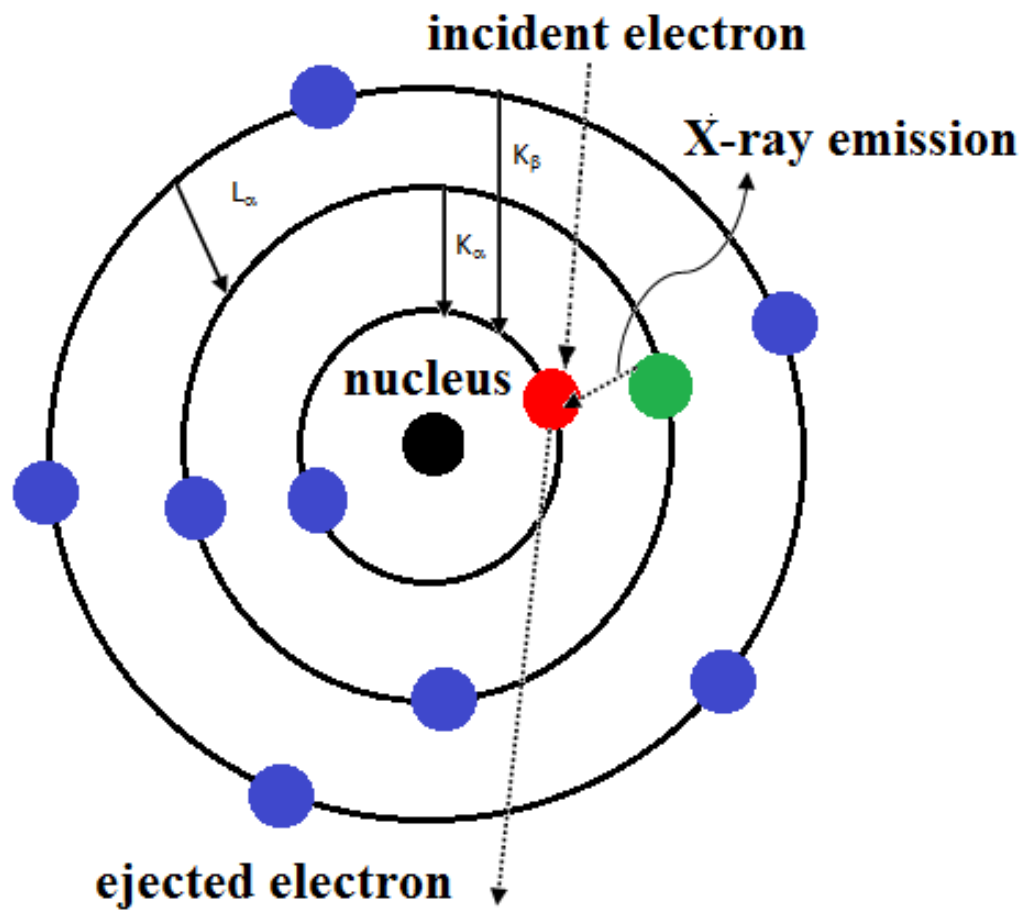
Figure: 2-2 Illustration of EDX principle

2.5 Electrical Resistivity and Seebeck Coefficient Measurement

2.5.1 Resistivity Measurement

A material's resistivity (ρ) is related to its ability to conduct electricity. Conductivity which is reciprocal of resistivity depends upon physical structure. For a rectangular slab of homogeneous material with length l, width w, and thickness t (in m), the resistance, R (in Ohms) along the length of the slab is related to the resistivity ρ (in Ω-m) by

$$R = \frac{\rho l}{tw} \tag{2-10}$$

In semiconductors, the quantity $\frac{\rho}{t}$ is termed the sheet resistance. The accurate determination of a material's conductivity can be critical for understanding material composition or device performance. The method use to determine conductivity depends on whether the material is a bulk sample or thin film. The samples fabricated for this research are bulk therefore we discuss bulk techniques for measuring resistivity. There are two methods most commonly used for measuring resistivity. The two- point probe measurement is simplest approach with limited accuracy and for fairly large samples and four-point probe measurement[5] is used for bulk sample slightly more complicated but yields much better accuracy Table 2.2 shows the comparison of both methods. Both of these methods can be potentially destructive to the sample depending upon how electrical contacts are made [6].

A four-probe method is typically used in which current flows through one set of current leads and voltage is measured using another set of voltage leads as shown in Fig. 2-3A.

Table 2- 3. Comparison of Two point probe and four point probe methods[6].

Method	Favored Material Type	Favored Material Form	Estimated Measurement Range (Ω)	Issues
Two-Point	High-resistance metals	Solid bar	10^2-10^9	Formation of oxide layers on surfaces and formation of p-n junction and can result in nonohmic voltages that lead to large resistivity
Four-Point	Metals	Solid bar	10^{-7}-10^4	Same as above
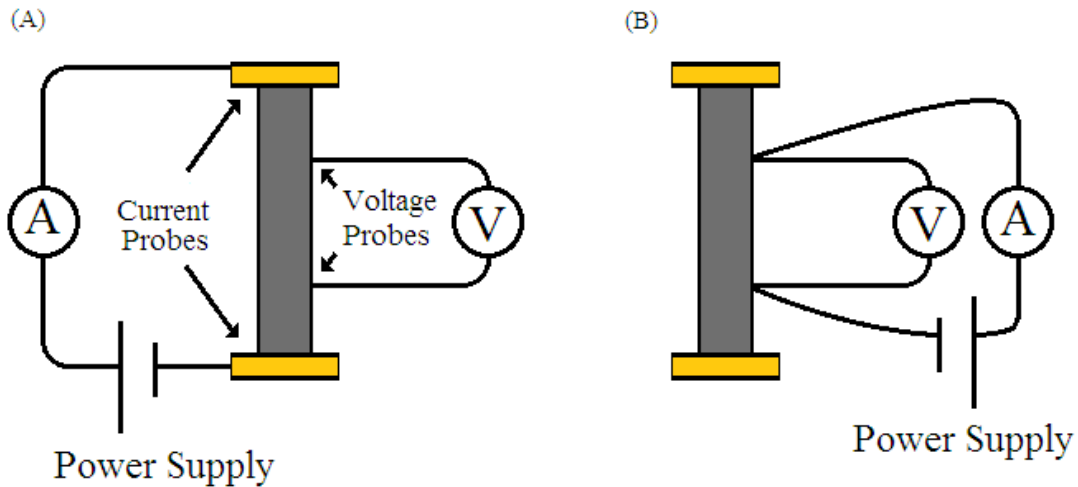
Figure 2-3. (A) Four probe measurement of resistivity (B) Two probe measurement of resistivity.

2.5.2 Seebeck Coefficient

The Seebeck coefficient can be positive or negative depending on the type of charge carrier and can be described as the entropy per carrier divided by the electronic charge[7]. Unlike the resistance, the Seebeck coefficient does not depend on the sample geometry and is simply given by a measurement of the voltage at two points on the sample divide by the temperature difference between these two points,

49

$$S_{SL} = \frac{\Delta V}{\Delta T} = \frac{(V_H - V_L)}{(T_H - T_L)} \qquad\qquad (2\text{-}11)$$

where S_{SL} is the experimentally measured value of the thermopower, which include both sample S_S and lead contribution S_L. The lead wire is typically Cu, gold, or Chromel and must be subtracted from each data point to get sample Seebeck coefficient of the material itself.

2.5.3 Principle

There are various instruments available commercially to measure Seebeck coefficient and there are two primarily two techniques that are used for measuring Seebeck coefficient. One of these involves fixing the sample temperature, T and varying a small temperature gradient across the sample. The sample voltage is recorded as a function of temperature difference and the slope yields S_{SL}. This technique is rather slow and is particularly adopted to investigate the temperature dependence of the Seebeck coefficient over a wide range of temperatures. An alternative approach involves applying a small fixed temperature gradient ($\frac{\Delta T}{T}$ a few percent) across the sample and slowly varying T. At each temperature of interest, several voltage measurements are made and Seebeck coefficient (S_{SL}) is calculated from the relationship ($S_{SL} = \frac{\Delta V}{\Delta T}$). To confirm linearity of ΔV vs ΔT and goes through $\Delta V = 0$ at $\Delta T = 0$, one should periodically sweep ΔV vs ΔT, and compare the slope of these measurements to the fixed measurement. Although this technique simpler and to some extent faster than the first one it is vulnerable to errors due to high resistance contacts.

2.5.4 Electrical Conductivity and Seebeck Coefficient Measurements

The samples used for this study $Zr_{0.5}Hf_{0.05}Ni_{1-x}Pd_xSn_{0.99}Sb_{0.01}$ are bulk thermoelectric and their composites. The powdery samples are hot pressed and cut into rectangular parallelepiped approximate dimension of 2mm × 2mm × 9mm for measurements of electrical resistivity and

Seebeck coefficient. Electrical resistivity and Seebeck coefficient are carried out simultaneously by using ULVAC ZEM-3 system shown in Fig 2-4.
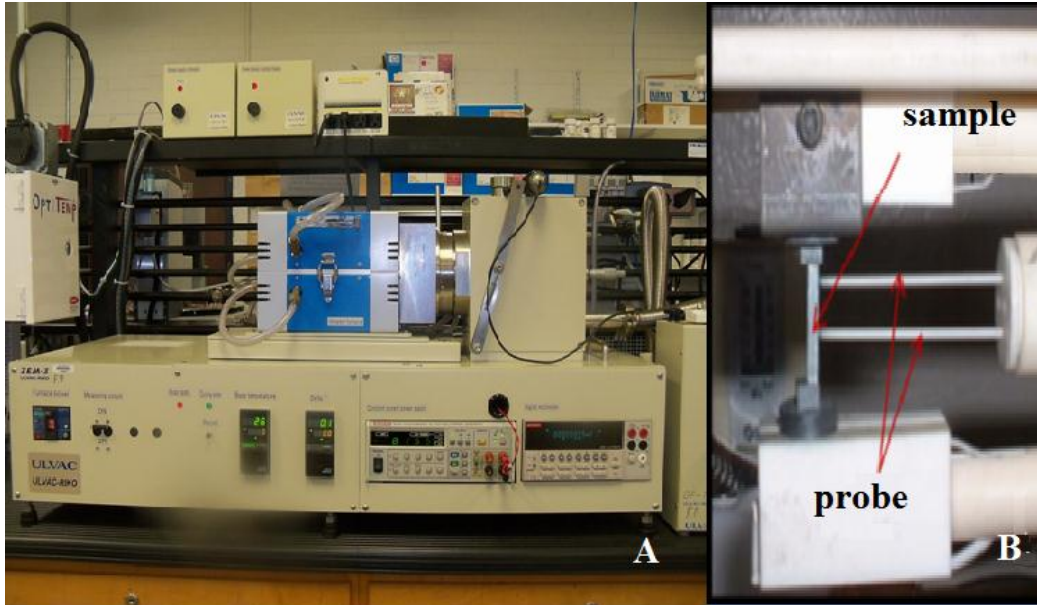
Figure: 2-4 ULVAC-ZEM3 system for the measurement of resistivity and the Seebeck coefficient.

The temperature range is preset by using computer, and all measurements are controlled by the computer and raw data is automatically saved. The conceptual diagram of ZEM-3 is shown in Fig 2-5. The space between the probes is fixed at 3 mm with small fluctuation. The sample is held between two jaws by pressure from the clamp springs. The pressure is advantageous and maintains a stable (thermal) contact resistance. Inside the lower jaw is an electrical resistance heater, which creates the temperature gradient along the sample. Probes A and B are R- type thermocouples made from Pt- vs Pt-Rh and measure both the voltage and temperature differences. These thermocouples are best known for exceptional stability at high temperature. To ensure the potential and temperature are uniform in the cross section

51

corresponding to the measuring contact points, the distance between the probes and the end plate should be 1.5 times larger than the sample width. An integrated microscope accessory assists in measuring the dimensions of the bar sample and the distance between the two probes accurately. An infrared light furnace is used to heat the environment.
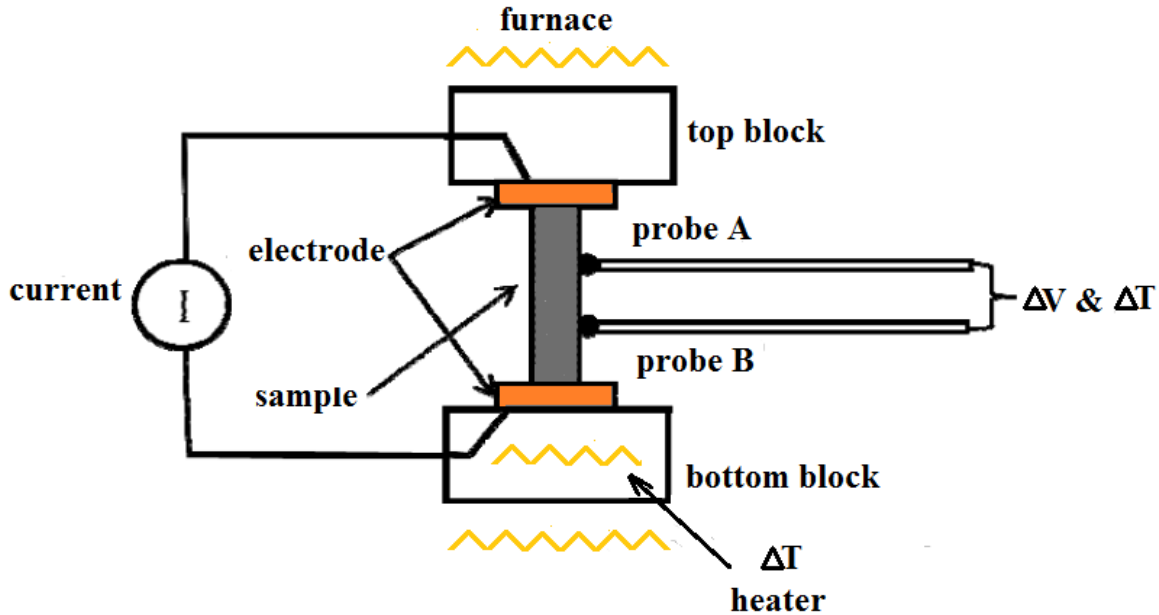
Figure: 2-5 Conceptual diagram for measuring voltage (ΔV) and temperature (ΔT) differences.

In order to quantify the systemic errors, a Constantan sample was used as a standard The measured Seebeck value of Constantan agrees with available data provided by the NETZSCH data within 5%, which proves the reliability of ZEM-3 system. The value of Constantan is 2 orders of magnitude lower in resistivity and 3 orders of magnitude lower in Seebeck coefficient than the half Heuslers materials we are interested in.

2.5.5 Procedure

The sample was loaded into the spring loaded posts and a graphite sheet was used to cover the holder in order to keep the environment temperature uniform and to avoid contamination. Then the furnace was closed and vacuumed. Prior to the start of measurement, a small amount of helium was filled into the chamber and the inside pressure was maintained at a pressure of several Torr. This is because Helium improves the thermal contact and shortens the time needed for the sample to reach thermal equilibrium. Before starting the measurement, V-I plots are quickly made to check whether the sample was properly contacted with the detecting probes. A linear plot guarantees a good ohmic contact. Seebeck and resistivity were measured simultaneously from room temperature to 500°C (773 K) with data point taken every 25°C In the electrical resistivity measurement, current was released from the current supply to the sample, and the voltage was measured by probes as shown in Fig. 2.4. To eliminate the effect of thermal asymmetry, two measurements were taken with opposite current polarity. The average result is regarded as the sample resistance.

In the Seebeck coefficient measurement, the current supply is open circuit with no current flowing through the sample. The temperature difference and potential difference are measured by probes as shown in Fig 2.5 (b). The equation used for computing the Seebeck coefficient is given as:

$$S = -\frac{\Delta V}{\Delta T} + S_{Probe} \tag{2-12}$$

where S_{Probe} is the Seebeck coefficient of the thermocouple. A typical Seebeck coefficient computation plot is shown in Fig. 2.6.

Note that there is a nonzero intercept of the regression with y axis, which is called dark EMF, the source of which is not known. In the ZEM-3 system, dark EMF is calculated at each temperature set-point. Only when the dark EMF is less than 10% of the Seebeck voltage, the measured Seebeck coefficient can be regarded as acceptable. The measured Seebeck value of Constantan agrees with established data within 5%, which proves the reliability of ZEM-3 system.

Equation	y = a + b*		
Adj. R-Square	0.99981		
		Value	Standard Error
E	Intercept	0.02912	2.3378E-4
E	Slope	-1.06671E-4	8.5281E-7
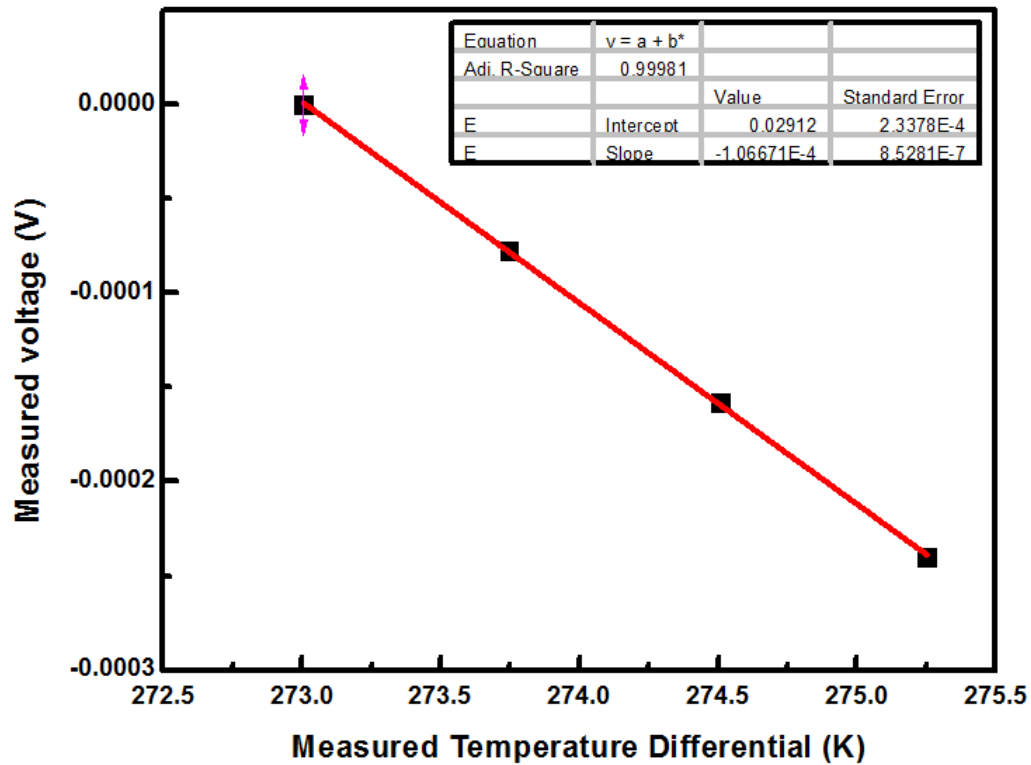
Figure: 2-6 Regression graph for computation of Seebeck coefficient by ZEM3 for Zr$_{0.5}$Hf$_{0.05}$Ni$_x$Sn$_{0.99}$Sb$_{0.01}$

2.6 Hall Effect

The Hall effect occurs when charge carriers are exposed to a magnetic field in a direction orthogonal to the carrier motion, thus causing a Lorentz force on the carriers, which deflects them enabling the calculation of the type of carrier, carrier concentration, and carrier mobility.[77,78] More concretely, if we consider charge carriers that are moving through a material with a certain velocity v_x in the x direction, v_x, due to a current when a magnetic field, B_z, is applied perpendicular to the motion of these charged particles in the z direction, a force in the y direction is exerted on the carriers perpendicular to both the direction of the motion of the particles and the magnetic field. This force on the charge carriers will cause them to deflect in that perpendicular direction. The positively charged carriers (holes) will deflect in one (right) direction and the negatively charged carriers (electrons) will deflect in the opposite direction as following the right hand rule using

$$\vec{F} = q\vec{v} \times \vec{B} \tag{2.13}$$

The separation of the charges carriers to different sides of the samples establishes a Hall voltage across the sample in the y direction given as[8]:

$$V_H = \frac{R_H I_x B_z}{d} \tag{2.14}$$

where V_H depends on the current, I_x, due to the movement of the carriers in the x direction, the thickness of the sample, d, and the Hall coefficient, R_H, which is a constant for a given material. For metals Hall coefficient is given by:

$$R_H = \frac{1}{ne} \tag{15}$$

where n is the carrier concentration and e is the charge of the electron. Due to the fact that the Hall effect is polarity sensitive with respect to the conduction type, the sign of the Hall constant

comprises the information of the dominating carrier type: negative sign–n-type (conduction is by electrons), positive sign–p-type (conduction is by holes). The Hall voltage can be measured and the current, magnetic field, and thickness can be known, therefore the carrier concentration can be estimated by using:

$$V_H = \frac{I_x B_z}{dne} \tag{2-16}$$

and considering acoustic phonon scattering in a degenerate system solving [9] we get:

$$n = \frac{I_x B_z}{de V_H} \tag{2-17}$$

Knowing electrical resistivity, the mobility, μ, can be calculated by:

$$\mu_e = \frac{\sigma}{ne} \tag{2-18}$$

Therefore the Hall Effect is a useful tool in determining majority charge carrier type, concentration, and mobility which cannot be found from a normal electrical conductivity measurement. For semiconductors or metals with more than one band of carriers or complicated Fermi surface topology these computations are more complicated.

Generally, the geometry of the sample used for hall measurement falls into two categories: long, narrow bars and second uses square or circular Van der Pauw geometries.

In Van der Pauw Fig 2-7 four in plane contacts are needed and are easily obtained through pressure contact. Two contacts measure the current and the other two are meant for measuring the emerging difference of potential. The disadvantage of this method consists in the fact that the only geometric parameter to be known is the thickness of the sample while there are no restricts on the shape of the sample. Another drawback of this method is problem of leakage current skewing the measured voltage.
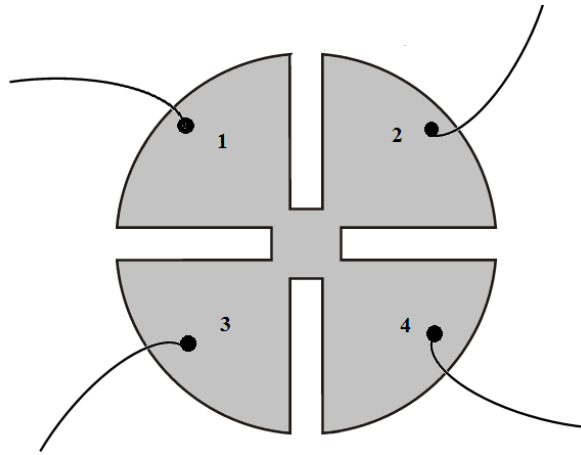
Figure: 2-7 Schematic of Van der Pauw sample geometry

The long narrow bar Fig 2.8 techniques uses geometry such that the electric potential difference between two points on the surface of the sample is linearly proportional to the distance between them. The hall voltage V_H is developed across the sample when the magnetic is field applied to the sample. The resistivity along the current direction can be easily calculated by measuring the resistance along that direction. Once the resistivity and carrier concentration are known, mobility can be calculated. The real problem in this geometry is that good voltage measurement contacts.are difficult to make, and various techniques are needed to negate the contact effect and the Ettingshausen Effect [10]. Van der Pauw geometry can easily overcome those difficulties[11]. The room temperature carrier concentrations and Hall motilities are measured on bar samples with five point contacts, with $V\rho_+$ and V_{Hall+} near the middle of the sample and directly across from each other. A magnetic field is swept from 0.5T to -0.5T taking data every 0.05T. At each field value an average over 30 data points is taken. The Hall coefficients are measured from the regression curve of the linear dependence field vs voltage and the carrier concentration is determined from the relation $n = {}^1\!/\!{R_H e}$. The accuracy of this technique is estimated to be less than 5% difference from the true value.
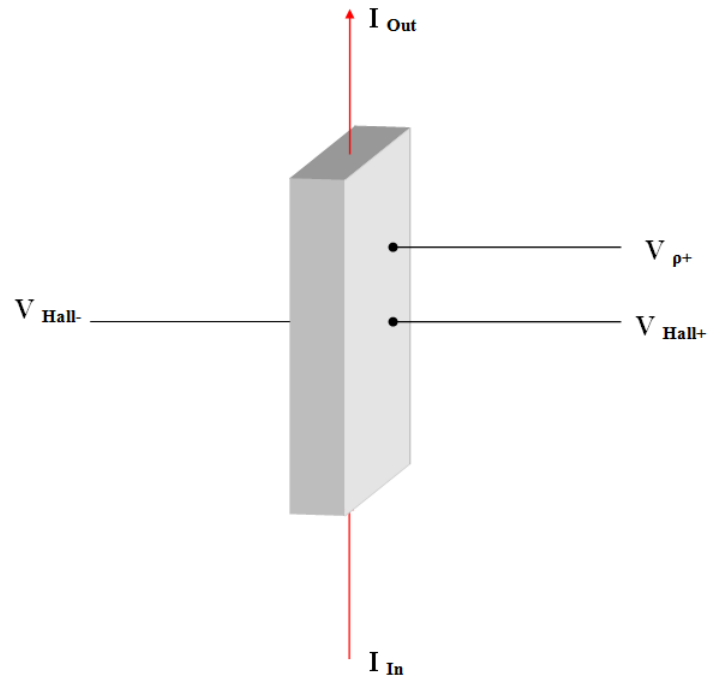
Figure: 2-8 Configuration of Hall effect. Electrical resistance is measured by $(V\rho_+ - V_{Hall+})/I$

2.6.1 Procedure

Hall effect measurements were done using a non-commercial system built in our lab. Room temperature carrier concentrations and Hall nobilities were measured on bar samples with five point contacts. The setup is shown in Fig. 2-9.The procedure is divided into two parts: contact fabrication and Hall measurement. The process of measuring the Hall Effect starts with applying reliable and uniform ohmic contacts to the material. One of the most common methods is to use a silver paste, PELCO® High Performance Silver Paste, to adhere five ohmic contacts to the sample. The Silver Paste is a
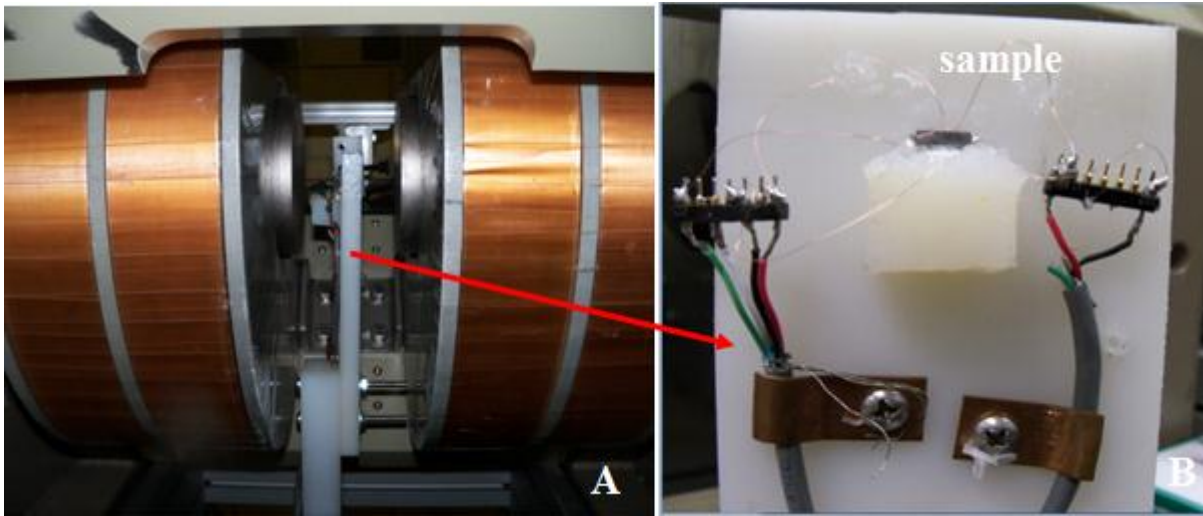
Figure: 2-9 Hall Effect Apparatus Sample holder for Hall Effect
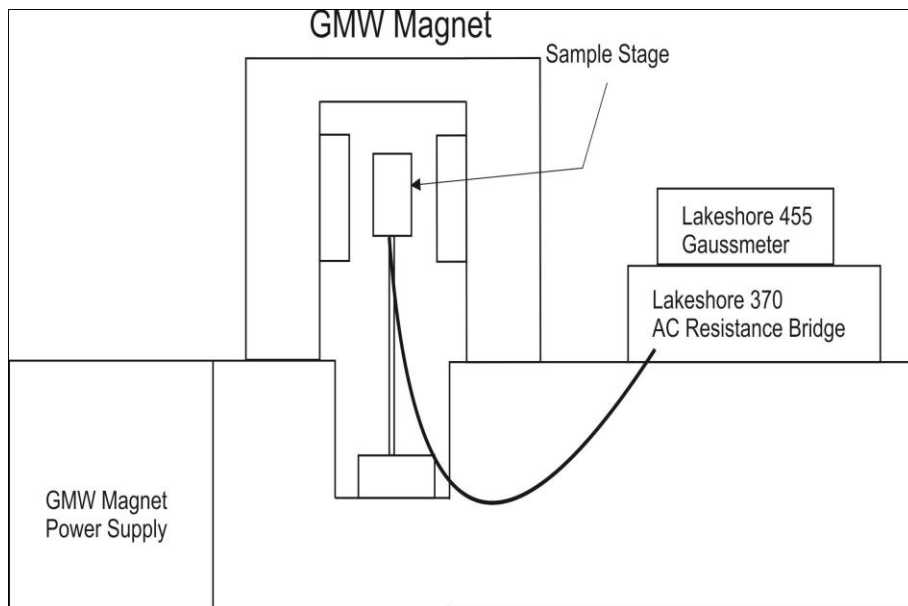
Figure: 2-10 Schematic of Hall Effect

one part epoxy used for temperature ranges from cryogenic to 1200K. The PELCO® High Performance Silver Paste was applied under a microscope to ensure as small as possible contact with the sample and to have minimal ohmic dependence. After the contacts were made they were annealed at 300 K for two hours and then at 360 K for two hours. These samples were prepared for the Hall Bar geometry with a five point contact to accurately measure the hall voltage and resistivity simultaneously, and then calculated the carrier concentration, hall coefficient, and mobility. All measurements were made at 300 K.

Once ohmic contact annealing took place the sample was then moved to the apparatus for measurement. This apparatus includes a GMW Magnet, GMW Power Supply, Lakeshore 370 AC Resistance Bridge, Lakeshore 455 Gaussmeter, and Labview programming software. The sample leads were soldered to the pre-existing wires from the resistance bridge and mounted firmly on the sample stage and the stage placed within the uniform magnetic field. The sample was oriented with the current being perpendicular to the magnetic field which produces a voltage that is perpendicular to both current and magnetic field. The Lakeshore 370 does the switching between resistivity and hall measurements. After sample was within the magnetic field, data was taken while sweeping the field from -0.5 Tesla to 0.5 Tesla. Positive and minus values of the magnetic field must be taken in order to cancel out any extra voltage from the leads being misaligned. The instruments and data taken were run by National Instruments Labview programming and provided seamless integration of the different instruments.

2.7 Thermal Conductivity Measurement

Thermal conductivity is the quantity of heat energy transferred per unit time and normally through unit surface area of unit thickness for unit temperature difference between the faces. It is more difficult to measure the thermal conductivity than electrical conductivity (σ)

with accuracy because thermal insulation can never be as good as electrical insulation. Heat loss through radiation, convection, and contacts always occurs, and can contribute to a significant portion of the total heat transferred. Thus for direct measurement of the thermal conductivity, extra care has to be taken to minimize those heat loss [12, 13].Thermal diffusivity is the parameter which determines the temperature distribution through a material in non-steady state conditions the material is being heated or cooled. It is the parameter that relates heat flow to temperature. Diffusivity is actually rather easier to measure experimentally than thermal conductivity because it is the only necessary to measure the change in temperature with time at two points in the material, whereas thermal conductivity needs knowledge of the heat energy.

2.7.1 Methods for the Measurement of Thermal Conductivity

There are two main methods used for the determination of thermal conductivity. These are steady-state and transient approach. The steady state means that the temperature at each point of the sample is constant i.e. not a function of time. The determination of thermal conductivity is based on the measurement of heat flux and a temperature gradient. i.e. mostly a temperature difference between opposite surfaces of sample.

The principle of one dimensional steady state methods are based on [6, 14]

$$\kappa = \frac{qd}{T_2 - T_2} = \frac{Pd}{A(T_2 - T_1)} \qquad (2\text{-}19)$$

The heat flux q is determined by the measurement of power P released in an electrical heater divided by the area A of the sample of thickness d. The temperature difference $T_2\text{-}T_1$ is determined between two opposite surfaces of the specimen. The sample geometry and configuration of a measurement system is important. Materials having low thermal conductivity the samples are usually cut into flat disks or plates. Samples which have high thermal

61

conductivity the, sample geometry is a cylindrical rod. The steady-state methods require long equilibrium time to reach steady state conditions and it is difficult to quantify heat losses.

The transient methods measurements are made during the process of heating. Numerous transient techniques as shown in appendix A[6] for the measurement of thermal conductivity are available depending upon the boundary conditions. We adopted the laser flash method for the measurement of diffusivity using transient technique in this research work. This method will be discussed in detailed in next section.

The major advantages of transient methods over the steady state are that less time is required for the experiment and that various thermal properties such as heat capacity and thermal diffusivity can be determined in the same measurement cycle. All transient methods measure diffusivity D which is a primary parameter in the complete differential equation for heat flow[6]:

$$D\left(\frac{\partial^2 T}{\partial x^2}\right) = \frac{\partial T}{\partial t} + \mu_{sur}T \qquad (2.20)$$

where μ_{sur} is the coefficient of surface heat loss which takes into account heat loss by radiation conduction and convection.

2.7.2 Laser Flash Method

The laser flash method developed by Parker in 1961[13] is the most frequently used method for measuring the thermal conductivity of bulk samples at high temperature. This method does not need thermal contact since a laser flash serves as the heat source. In addition, the heat loss through sample boundaries and radiation is minimized by a quick measurement time. In contrast to other methods, the laser flash technique is mostly widely used for different classes of materials such as polymers, glasses, ceramics and metals and can be applied without significant limitations on the achievable measurement uncertainty. The Laser Flash Method is the ASTM standard

Figure: 2-11 LFA 457 MicroFlash designed by Netzech for the measurement of diffusivity.

E1461-01[15] but actual execution of measurement may be subjected to random or systematic errors. Therefore it is important to quantify the apparatus so that the errors can be accounted for in the data.

The figures 2-11 and 2-12 show the Laser flash apparatus LFA 457 and its schematic. The thermal diffusivity and specific heat are directly measured in this research work were measured by LFA 457 and Pyroceram reference was used alongside each sample. Thermal conductivity was calculated from the thermal diffusivity data by using relation:

$$\kappa = DC_p\, d \tag{2-21}$$

The thermal diffusivity D obtained depends on sample thickness and the time required for the rear surface temperature rise to reach 50% of its maximum value. Specific heat capacity Cp is

the measure of the heat energy required to increase the temperature of a unit quantity of a substance by a certain temperature interval and depends upon sample density d
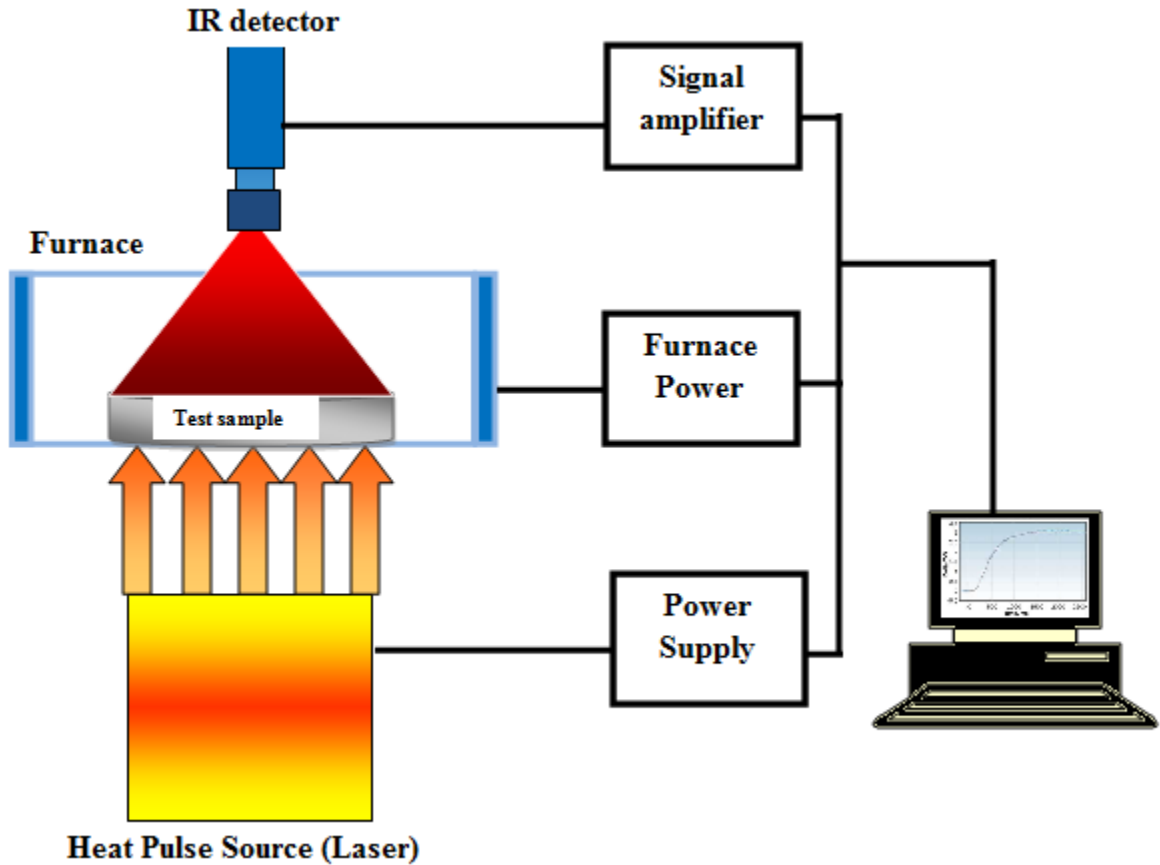
Figure: 2-12 Schematic of a Laser Flash System

2.7.3. Princeiple of Laser Flash

The working of laser flash is based on a simple principle. One face of a flat disc sample is irradiated by a short pulse of heat from a laser irradiation of times being ≤ 1 msec. The resultant temperature rise of the opposite surface is recorded by IR detector, from which the thermal diffusivity is computed with temperature rise vs. time profile. Numerous mathematical models such as Parker Model, Cape Lehmann, Clark Taylor, Cown, Radiation Ratio and Finite Pulse

width concerning the temperature rise vs. time have been built by factoring in heat loss from the front and back side and non-uniform heating. By fitting the experimental data with these models, diffusivity with errors less than 3% can be obtained. Only two models Parker and Cowen will be discussed. For this research work we used Cowen model.

2.7.4. Parker Model

According to Parker et al [1] the whole radian energy is absorbed instantaneously (zero pulse width) on sample surface facing the heat pulse source and the material properties are constant over the small step of the measurement. In addition it is assumed that heat conduction in the sample is one dimensional and that heat losses could be neglected. Basic equations for one dimensional transient heat transfer are[6]:

Boundary condition:

$$\frac{\partial T}{\partial t} - D \frac{\partial^2 T}{\partial x^2} = 0 \qquad (2\text{-}22)$$

Initial condition

$$\frac{\partial T}{\partial t} = 0 \ ; \ \frac{\partial T(L.t)}{\partial x^2} \qquad (2\text{-}23)$$

Under these conditions the temperature at the rear face of the material at any time is given by[14]

$$T(L, t) = \frac{q}{d C_p L} \left[1 + 2 \sum_{n=1}^{\infty} (-1)^n \, e^{-n^2 \pi^2 \frac{Dt}{L^2}} \right] \qquad 2.24)$$

where q is the heat flux resulting from the light pulse, d is the density , Cp specific heat capacity and D the thermal diffusivity of the material. Consider non dimensionless parameters

$$\Theta = {T(L,t)}/{T_m} \qquad 2\text{-}25)$$

$$\alpha = Dt/L^2 \qquad (2\text{-}26)$$

where T_m is the maximum temperature rise at the rear surface $[T_m = T(L, t \to \infty)]$ .Equation 2-24 can be rewritten as:

$$\Theta(\alpha) = \left[1 + 2\sum_{n=1}(-1)^n e^{-n^2\pi^2\alpha}\right]$$ (2-27)

Using (2-27) the thermal diffusivity can determined by plotting non dimensional temperature $\Theta(\alpha)$ against non-dimensional time α , Fig 2-14.A where $\Theta(\alpha)$ is equal to 0.5 α is equal to 0.1388. From 2-26 it is followed that diffusivity is

$$D = 0.1388L^2/t_{0.5}$$ (2-28)

where $t_{0.5}$ is the time required for the back surface temperature rise to reach half of its maximum. Thermal diffusivity depends only on the shape of the temperature vs time curve Fig 2.14[16] and the thickness of the solid. According to this model it is not essential to know the amount of energy absorbed in the front surface in order to determine the thermal diffusivity. The maximum deviations of the data obtained from this model are order of 5%. Instantaneous pulse heating in the front surface of the material is assumed. Heat losses are neglected and are more significant when testing low conductivity thick samples at high temperatures

2.7.5 Cowan Model

Cowan designed a model for the identification of thermal diffusivity using the amplitude and phase measurements of the surface temperature variation [16]. The main difference between Parker's model and Cowan model is, former model was concentrated on the practical implementation of the flash method with simple mathematical model and later model is one dimensional mathematical model with instantaneous absorption of the energy from the source on one the sample surfaces. In Cowen model, heat losses from the sample surfaces are considered in the form of linear radiation boundary condition and the energy of beam is analyzed either as a square wave or as sine wave.

66

When the heat is lost from the sample surface, the temperature vs time curve touches its maximum. After peak the solid temperature falls off due to the cooling effect imparted by the heat loss as illustrated in Fig 2-14 B. The expression for the rear surface derived by Cowan[17]

$$\Theta(\alpha) = \frac{q}{dC_p L}\left[e^{-a\alpha} + 2\sum_{n=1}^{\infty}(-1)^n e^{-n^2\pi^2\alpha}\right] \qquad (2\text{-}29)$$

where $\Theta(\alpha) = T(L,\alpha) - T_o$ and T_o is the initial temperature in the medium and a is non-dimensional parameter accounts for the heat losses and is given by[16, 17]:

$$a = L\left[\frac{1}{\kappa}\left(\frac{dW}{dT}\right)_{x=0} + \frac{1}{\kappa}\left(\frac{dW}{dT}\right)_{x=L}\right] \qquad (2\text{-}30)$$

where W is the heat flux at the surfaces x= 0 and x=L and κ is the thermal conductivity. In the case there is no heat loss from the solid surface of the material to be investigated a =0 and equation (2-29) reduces to (2-27) of Parker's Model. The Cowen model requires heat loss
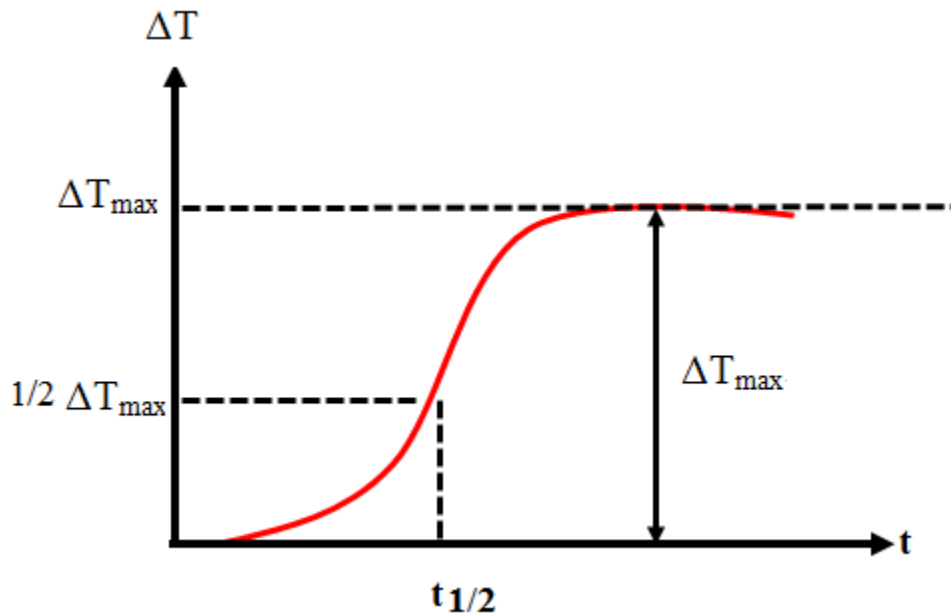
Figure: 2-13 Theoretical Plot of temperature rise at the rear surface of the sample
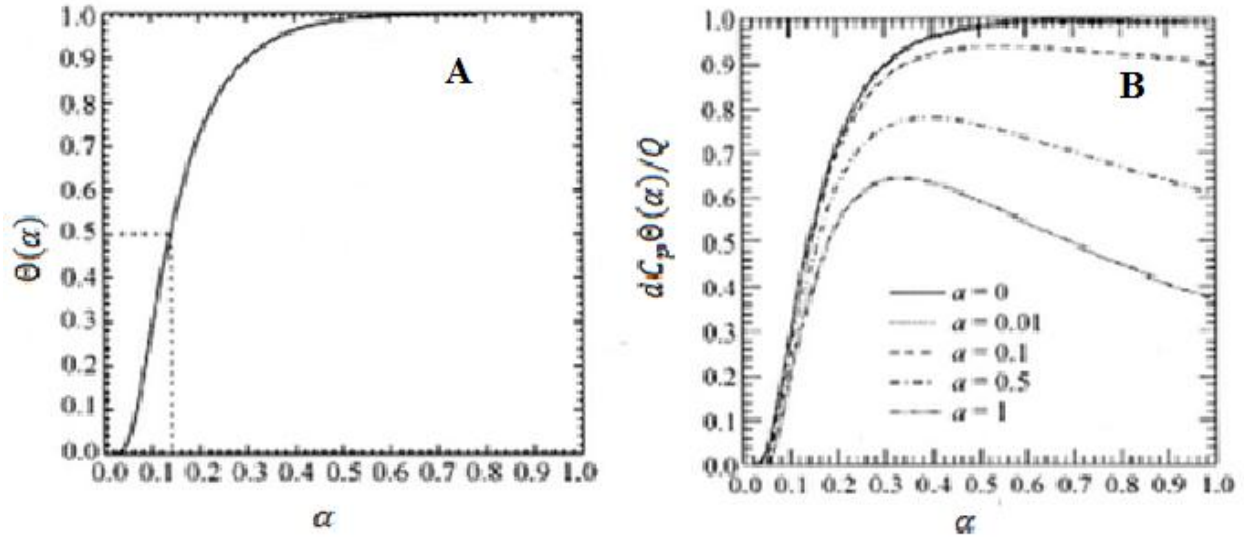
Figure: 2-14(A) Thermal diffusivity measurement results according to Parker et al [13]. (B)Heat losses effects on the real surface temperature according to Refs. [16,17].

parameter to get a with sufficient accuracy. Considering heat loss by radiation, emissivity ε can give a in the form as [16, 17]:

$$a \approx 2.3 \times 10^5 \left\{ \left[1 + \left(\frac{T_L}{T_0} \right)^3 \right] \left(\frac{T}{1000} \right)^3 \left(\frac{\varepsilon L}{\kappa} \right) \right\}$$

(2-31)

2.7.6 Description of LFA 457 MicroFlash Apparatus

The LFA 457 MicroFlash R designed by Netzech is shown in Fig 2.11. This apparatus is capable of measuring for thermal diffusivity measurements up to a higher temperature regime from 25-1370C°. The Laser-Flash flashes a laser shots into a sample and measures the rate the heat emitted from the sample. No calibration is required for the determination of diffusivity. This method can be used for material with thermal diffusivities between 0.01 and 100mm^2/s. The laser flash apparatus comprises mainly of a laser (Nd-glass laser), a furnace, and an IR detector (InSb detector) and is controlled by the data acquisition program known as LFA measurement. The Nd-glass-laser has maximum pulse energy of 15 J and pulse length of 0.33 ms .In order to promote even heating of the surface as well as to inhibit the reflection of incident radiation the

entire sample is coated with graphite prior mounting on the sample carrier. The sample is placed in a sample puck, which fits into a sample carrier. This sample carrier can carry three samples or one large sample. As the laser flash acquires data it is automated to rotate the sample carrier in order to measure three samples simultaneously. The laser flash system is able to accommodate samples of various geometries. We used circular sample carrier for samples of 10.07 mm in diameter between 2.6-2.9 mm in thickness. Pyroceram is used as standard material placed alongside of samples and SiC sample holders are used. The sample should be made flat by using gird paper make sure there is no traces of graphite sheet sticking to it. This step is essential to due to the fact that the laser flash should enter the sample at a 90 degree angle in order to promote a uniform heat flow through the sample. Temperature is controlled by a thermocouple located inside the furnace. At each temperature, the sample is measured 3 times; the results are averaged to minimize errors.

2.7.7 Procedure

High temperature thermal conductivity is measured using thermal diffusivity in the Nezstch 457 Microflash system as seen in Fig. 2.11 Half Heusler alloys have high melting point < 1100C˚ but we obtained data from 25°C up to 500°C.

Disk samples of size approximately 10.07 mm in diameter and 1.8-2.5mm thick were cut using wire saw and prepared for the laser flash method by thorough polishing, cleaning and then spraying a light coating of graphite using on top and bottom surfaces. Because graphite has a high thermal conductivity, this layer of graphite insures that the entire surface is heated evenly when flashed and then is evenly measured on the other side. The samples were placed in SiC sample holders, then mounted on the sample carrier and aligned between the laser beam and IR
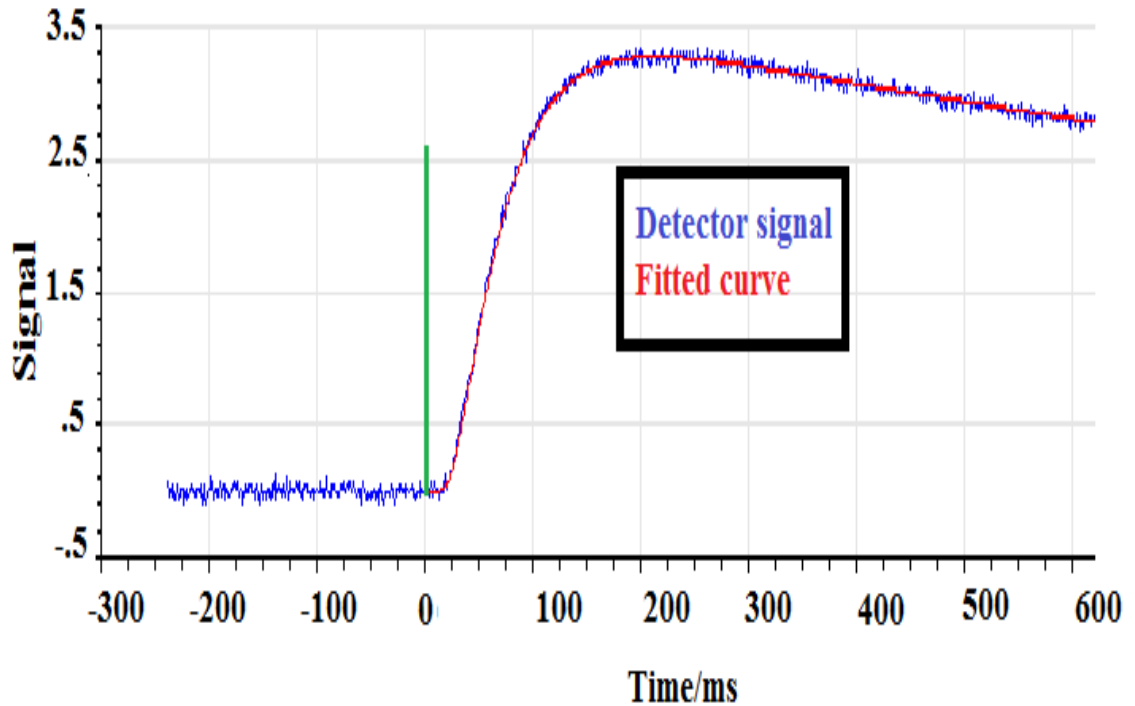
Figure: 2-15 Detector signal (in V) as function of time fitted to Cowen model.

detector. The system was pumped down, flushed with N_2, and this process was repeated three times, and then left to have a 75 mL/min flow rate of N_2. The inert atmosphere helped the samples not react to air molecules or anything else trapped in the chamber at higher temperatures. As the system is vacuumed and purged important information about materials (density, mass and thickness) to obtain the data were entered into the laser flash program. The system is set to ramp up to temperature at 10 K/min and stabilizes at the desired temperature. Once the temperature and baseline were stabilized the Nd-glass-laser was flashed onto the bottom of the sample which heated up the bottom side of the sample. The heat induced permeated through the sample and caused the temperature to increase on the top surface of the sample, was measured using a liquid nitrogen cooled indium antimonide (InSb) infrared detector. The LFA 457 use Proteus software to carry out measurement and analyze the data. Thus Proteus

evaluated the rise in temperature is from temperature vs time curves. Proteus also estimated half time from the Cowan--pulse correction data. The program calculates the diffusivity using half time method governed by equation

$$D = 0.1388 \frac{L^2}{t_{\frac{1}{2}}}$$ (2-32)

where D is the thermal diffusivity is the sample's thickness, and $t_{\frac{1}{2}}$ is the half time. Because the temperature and detector data are proportional, the Proteus program calculates the maximum detector signal and cuts it into half to find the half time. At each temperature the thermal diffusivity was measured 3 times and averaged. By measuring the density, d, and specific heat, Cp, of the sample the thermal conductivity, κ, is estimated using (2-21). The density is calculated using the sample's mass and dimensions and confirmed using a gas pycnometer. The specific heat is estimated using the LFA Analysis. The program assumes that laser pulse energy and its coupling with the sample is stabilized (remains unchanged) and estimates the specific heat of the sample by the equation:

$$C_p(sample) = \frac{(mC_p\Delta T)_{ref}}{(m\Delta T)_{sample}}$$ (2-11)

C_P measurement data from the laser flash system is only approximate. The results of laser flash are both reliable and reproducible within 5% when measuring the thermal diffusivity.

2.8 References

[1]   H. P. Klug and L. E. Alexander, Ray Diffraction Procedures for Polycrystalline and Amorphous Materials, Wiley, New york, 1974.

[2]   P. Scherrer, Nachr Ges Wiss Gottingen (1918) 96.

[3]   G. K. Williamson and W. H. Hall, Acta Matall 1 (1953) 22.

[4]   Joseph Goldstein , Dale E. Newbury, David C. Joy, and E. Charles, Scanning Electron Microscopy and X-ray Microanalysis, Springer, 2003.

[5]   G. S. Nolas, J.Sharp, and J. Goldsmid, Thermoelectrics: Basic Principles and New Materials Developments, Springer, 2001.

[6]   C. Horst;, Saito Tetsuya, and E. Smith Leslie, Springer Handbook of Materials Measurement Methods, Springer, 2006.

[7]   T. M. Tritt and V. M. Browning, in Semiconductors and Semimetals, Vol. Volume 69 (M. T. Terry, ed.), Elsevier, 2001, p. 25.

[8]   N. W. Ashcroft and M. D. Mermin, Solid State Physics, Brooks Cole, Philadelphia, PA, 1976.

[9]   C. A. Kukkonen and P. F. Maldague, Physical Review B 19 (1979) 2394.

[10]   T. Krylov and V. VMochan, Journal of Teachanical Physics, (USSR) 25 (1955) 2119.

[11]   L. J. Van der Pauw, Philips Techanical Review 20 (1958) 220.

[12]   R. Bowers, R. W. Ure, J. E. Bauerle, and A. J. Cornish, Journal of Applied Physics 30 (1959) 930.

[13]   W. J. Parker, R. J. Jenkins, C. P. Butler, G. L. Abbott, and Journal of Applied Physics 32 (1961) 1679.

[14]   D. M. Rowe, Nature Publishing Group, 1995.

[15]   Test Method E1461-01, "Standard Test Method for Thermal Diffusivity of Solids by the Flash Method", ASTM, 2001.

[16]   R. D. Cowan, Journal of Applied Physics 32 (1961) 1363.

[17]   R. D. Cowan, Journal of Applied Physics 34 (1963) 926.

CHAPTER 3

OVERVIEW OF HEUSLER AND HALF HESULERS

3.1 Introduction

The search for new functional materials having noteworthy properties is of tremendous importance in material science. Important classes of materials with potential for application in sustainable energy technologies are the Heusler compounds. The Heuslers are a remarkable class of intermetallic materials discovered in 1903 by Friedrich Heusler[1] and comprise more than 1500 members. Heusler alloys, on account of their promising thermoelectric properties are given much interest in research. Heusler compounds are classified into two main groups, the full Heusler and half Heusler compounds. The full-Heusler compounds are metallic in nature and exhibit chemical formula (XY_2Z), X and Y are usually transition metals (see Fig. 3-1) and Z is Sn, Sb, or Bi etc. having low melting point as compared to X and Y elements. The half-Heusler were discovered by W. Jeitschko [2]. These compounds are also called Nowotny-Juza compounds [3, 4] particularly for example such as LiZnP and AgMgAs. Our goal of this research work is to study the transport properties of ZrNiSn based half Heusler system. In this chapter a brief over view of half -Heusler compounds will be discussed.

3.1.1 Crystal Structure

The half-Heuslers have general formula XYZ (usually Y=T, Zr, Hf etc,X=Ni, Co, Ir etc and Z= Sn, Sb, Bi, or Se The typical elements are shown in Fig. 3.1 The ordered crystal structure of these alloy is fcc and crystallize in MgAgAs type structure [5] with three filled and one vacant interpenetrating fcc sub lattices.
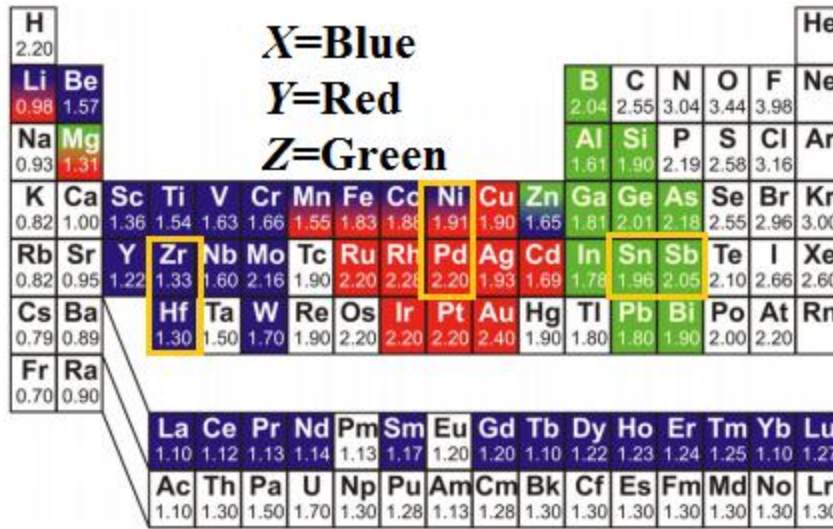
Figure:3-1Half Heusler elements used in present study are bounded by yellow lines in the chart[6].

It is the vacancy sub lattice which separates half-Heusler from full-Heusler alloys. These alloys belong to space group $F\overline{4}3m(216)$[2].Lattice constant of these compounds mostly lies in the range of 5.7 to 6.3 Å and had been found experimentally 5.69 Å for TiNiSn, 6.22 Å for ZrNiSn and 6.066A for HfNiSn[7]. The typical X-ray diffraction patterns of half-Heusler solid solution bear resemblance to fcc lattice such that the reflection indices hkl are either all even or all odd. The mostly investigated half Heusler base compounds are XNiSn type. Figure 3.2 shows crystal structure of one of such alloy where X =Zr., Y=Ni and Z=Sn with conventional Wyckoff atomic positions are 4a(0.0,0) for 4b(0.25.0.25,0.25) for Ni, 4c(0.5, 0.5, 0.5) for Sn and vacancy at 4d(.75,.75,.75).and these atomic sites have same point-group symmetry $F\overline{4}3m$ .The Ni site is called unique site since it has eight nearest neighbors(NN) atoms and (four Zr atoms and four Sn atoms) while Zr and Sn have four Ni atoms as NN. One of the perceptible facet of this structure is site exchange among the constituent elements results in different electronic properties [8-10], changing from a narrow gap semiconductor to a zero gap semiconductor or metals and it is
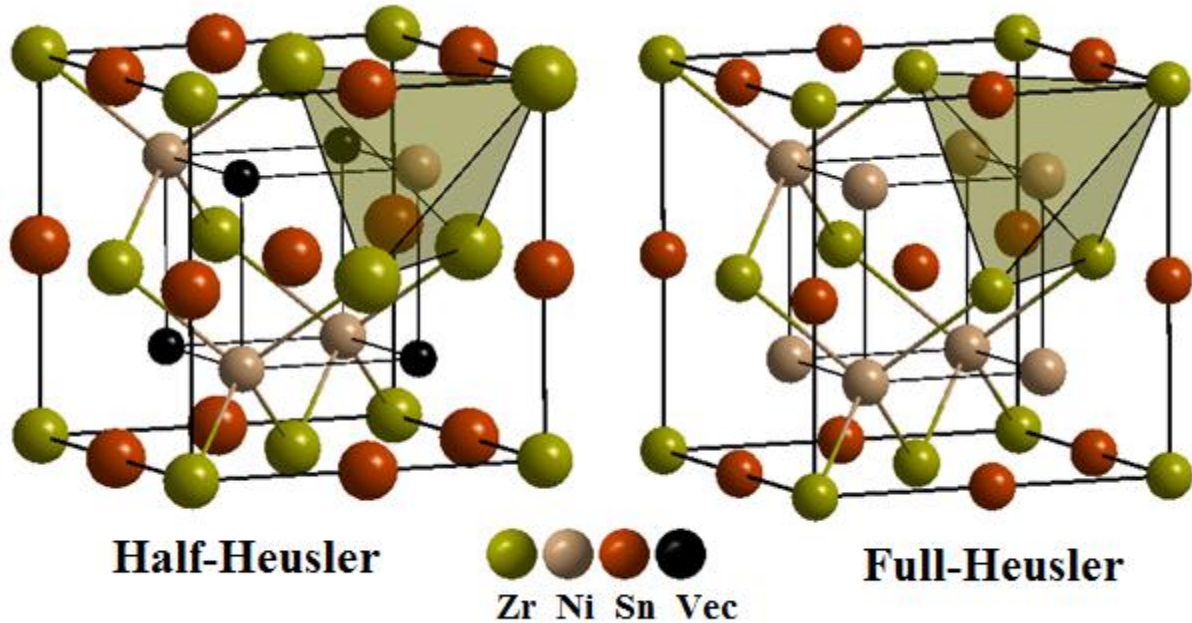
Figure:3-2 Ni is tetrahyderally coordinated to Zr. Hesuler closely resemble to Zinc blend and Full Heusler to CaF$_2$

therefore critical identify the correct configuration of atoms with the lowest energy. Ogut and

Rabe[11], using local density approximation method concluded that in ZrNiSn-type, that Ni-

atoms inserted into octahedrally coordinated positions ZrSn arranged in NaCl type basis

structure had energetically little effect on the stability of the final compound[12]. Thus Ni atom

enters into this octahedral coordination as neutral atoms and do not participate in any sort of

bonding with Zr and Sn atoms[12]. The main sources of structural stability in half-Heusler

compounds containing Ni is stability *YZ(Y=Zr,Hf,or Ti, Z=Sb, Sn Sc)* in NaCl substructure over

the diamond substructure and the fact that the effect of Ni, while responsible for the emergence

of the band gap, has little effect on the stability of the half-Heusler structure [12].

3.1.3 Effect of Valence count on Band gap

Dwight[13] has reported that total number of valence electron per formula unit cell or

valence electron cunt is an effective criterion in regards to the occurrence of specific crystal structure in these compounds.

The cubic MgAgAs type structure encompasses the VEC range 18, 19 or 20. These compound with VEC 18 electron compounds are closed shell species, nonmagnetic and semiconducting[14].Thus properties of half Heusler compounds can be envisaged by electron count[15] which effect the crystallographic and narrow band phenomenon. It is known VEC in half Heusler compounds such as ZrNiSn[16],TiCoSb [17]. and LnPdSb[18] plays important role in band structure as well as behavior of Hesuler and half-Heusler[19, 20], have VEC of 18 and show semiconducting behavior because of the gap at the Fermi energy. As VEC decreases or increases Fermi energy is falls below the top of the highest occupied valence band or rises above the bottom of the conduction band which results in a p-type or n-type metallic state, respectively. As can be seen from the electronic configuration of Zr ($4d^25s^2$), Ni ($3d^84s^2$) and Sn ($5s^25p^2$) and total number of valence electron is 18.All samples with various concentration of Pd $Zr_{0.5}Hf_{0.5}Ni_{1-x}Pd_xSn_{0.99}Sb_{0.01}$ we study in this research retain VEC of 18.The valence count for $Zr_{0.5}Hf_{0.5}Ni_{1-x}Pd_x Sn_{0.99} Sb_{0.01}$ is calculated by using simple formula:

3.1.4 Band Gap

It was determined by density of states measurements and experimental measurements that there is a gap near the Fermi energy in half-Heusler compounds with valence electron count (VEC) of 18 indicating compounds are semiconductors[8, 9, 21] Alieve measured the band gap in half-Heusler compounds of type YNiSn(Y= Zr, Hf, Ti) in the range 0.1-0.2 eV[8]and found it to be indirect type band gap. Later it was determined that the band gap energy of this type of half Heusler base system depends on the degree of hybridization of d orbitals of the X or Y element and p-orbital of Z element [11, 21]. Density functional calculation for 18 VEC system when X in

(*XYZ*) in electropositive such as in yttirum band gap varies from 0.16 to 0.53eV [8]. The band gap of 8-eletron compounds of Li*YZ* half Heusler varies from 0.45 to 2.51ev[22].

3.1.5 Properties of Half-Heusler

Thermoelectric Properties

The fabrication of thermoelectric module depends upon the properties of both n-type and p-type materials. Presently several benign half-Heusler alloys have been investigated. The most studied n-type half-Heusler materials are XNiSn based and XCoSb-based compounds with X=Ti,Zr, or Hf. Thermoelectric properties of the p-type compounds such as ZrPtSn, HfPtSn. ErPdSb, Er Pd Bi, NbIrSn,[23, 24] and Lathandies based LnPdZ (Ln=Lanthanadies, Z=Bi or Sb) and LnNiSb(Ln=Td, Dy, Ho, Er, Tm and Lu) have also been studied [25]. The properties of n-type half Heusler compounds are generally superior to those of the p-type counterparts because of their small band gap[26]. The most attractive feature of half-Heusler alloys as promising nontoxic thermoelectric materials is the large room temperature Seebeck coefficient of approximately -200 to- 400 μVK^{-1} [8-10, 27]]and high electrical conductivities of around 1000-10,000 Ω-cm^{-}1 [16, 28-32].However half Heuslers alloys have high thermal conductivities greater than 10 W/m-K. The total thermal conductivity as we have seen from Chapter 1 is the sum of two contributions the lattice thermal conductivity and electronic thermal conductivity. The lattice thermal conductivity for most the half Heuslers is much larger than the electronic thermal conductivity. The task of improving the figure of merit of a these thermoelectric materials lies upon reducing the lattice thermal conductivity. The half Heusler crystal structure with vacant and lattices provides great affinity for tuning lattice properties via substitution. Uher et al [16] were able to reduce the thermal conductivity of ZrNiSn half Heusler compound by alloying on the Zr site utilizing mass fluctuation. Shen et al [33]extended
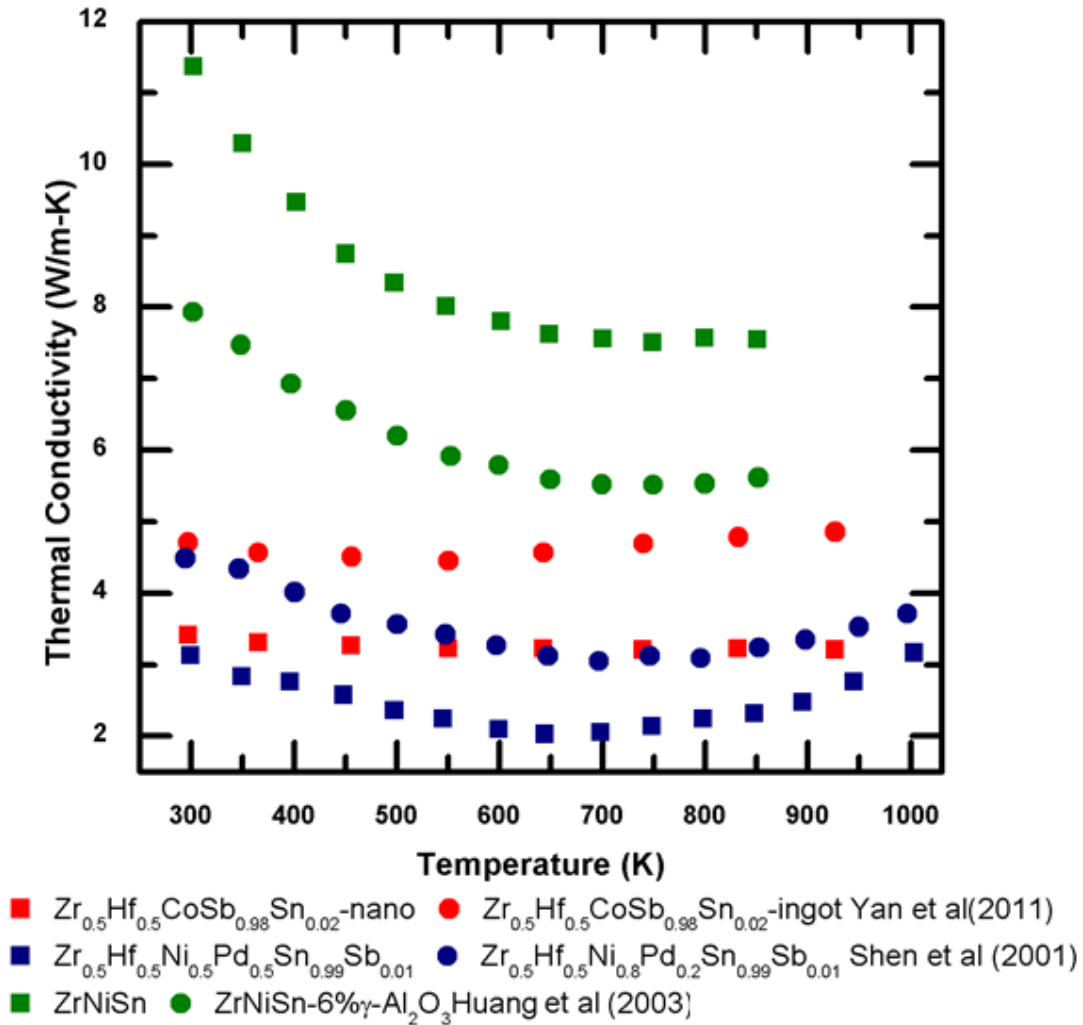
Figure:3-3 Reduction in temperature dependent thermal conductivity of various half Heusler compounds [30,31,32]

Uher's study by substituting Hf at Zr site and Pd on the Ni site. His study showed that thermal conductivity is greatly reduced in $Zr_{0.5}Hf_{0.5}NiSn$ type system to ~2.2 W/m-K by substituting 50% Pd at Ni and 1% Sb at Sn[33] as shown in Fig 3.3 (blue circles and squares).

Thermal conductivity is also reduced significantly by introducing more phonon scattering sites. This can be achieved by two routes. The first route is to introduce nanoinclusions into bulk material. X.Y Huang [34] incorporated γ-Al_2O_3 nano-particles into ZrNiSn and observed reduction in lattice thermal conductivity from 10.8 to 7.59W/m-K at 300 K in ZrNiSn by

introduction of 6vol% γ-Al_2O_3 nano Fig 3.3(green circles and squares).The Second route to reduce their thermal conductivity is to consolidate a fine powder to form a composite encompassing many nanometer-scale grains. This is commonly known as "nanostructuring". With the decreasing grain size the grain boundary scattering increases the thermal resistance thereby reducing the overall thermal conduction of the nano composites. Adopting this approach of fabrication of nanocomposite Xiao Yan[32] is successful in reducing thermal conductivity of $Zr_{0.5}Hf_{0.5}CoSb_{0.8}Sb_{0.2}$ to 4.71W/m-K by ball milling the required material Fig 3.3(green circles and squares).

Magnetism

The electrical and magnetic properties of half Heuslers are ruled by valence counts depending the location of paramagnetic gap at or close the Fermi level[35]. When the VEC is 18 these compounds are nonmagnetic semiconductors. However, when the VEC is different from 18, the compounds are metallic. For example TiIrSn, TiCoSn ZrIrSn have VEC= 17, TiNiSn has VEC=19 and MnNiSb has VEC=22 and all have metallic behavior. Using electronic structure calculations,de Garoot found NiMnSb to be half metallic ferromagnetic with unusual electronic properties [36]. CuMnSb is one of the most known antiferromagent at low temperature in the Mn-based half-Heusler. The study of this half-Heusler have shown Néel temperature T_N vary from 50 K to 62 K[37-39] TiCoSn and VCoSb are weak ferromagnets with Curie temperature of 135 and 58 K and saturation magnetic moments to 0.35 and 0.18μ_B respectively[40]

Superconductivity

The Heusler compounds constitute not only metallic and semiconducting material but also superconducting compounds. Generally the superconductivity is found in Heusler compounds with VEC >18.Though superconductivity has been observed in Ni rich alloys

NbNi$_2$C (C= Al, Ga Sn)[42, 43] but no clear understanding and interpretation of the origin of superconductivity has been been made so far. G. Goll [44]discovered superconductivity in semimetallic half Heusler LaBiPt, below $T_c \approx 0.9K$ by using resistivity and magnetization measurements. He assumes that occurrence of superconductivity in LaBiPt is due to exceptionally low charge carrier concentration of $n = 6 \times 10^{18}$ cm^{-3}. The charge carrier concentration is 1–2 orders of magnitude lower than in the classical low-carrier-density superconductors GeTe, SnTe and n-doped SrTiO$_3$.

3.2 Recent Developments in Half-Heusler Alloys

Improvements have been made in the thermoelectric properties and figure of merit of half-Heusler compounds in recent years. Various theoretical and experimental studies of half Heuslers have shown that these compounds exhibit diverse tunable features. It has been seen that half-Heusler alloys that show semiconducting behaviors at high temperature are found to be semi metallic at low temperature[45]. As we know the chemistry and transport properties of half-Heuslers can be conveniently controlled by selective substitution on the of three sub lattices in crystal structure. Browning and her coworkers in 1998 explored the effect of chemical substitution on both Zr and Ni sub lattice and in the effects of varying Sn composition were also studied[46]. However they were not successful into enhancing the thermoelectric figure of merit. It was later reported that that the properties of half-Heuslers are strongly impacted by annealing conditions[41]. Prolonged annealing not only affected the resistivity but also the thermal conductivity, both affects are attributed to sensitivity of the electron and pohonon transport to the structural disorder which is altered by annealing duration. These results are shown in Fig 3.4

80
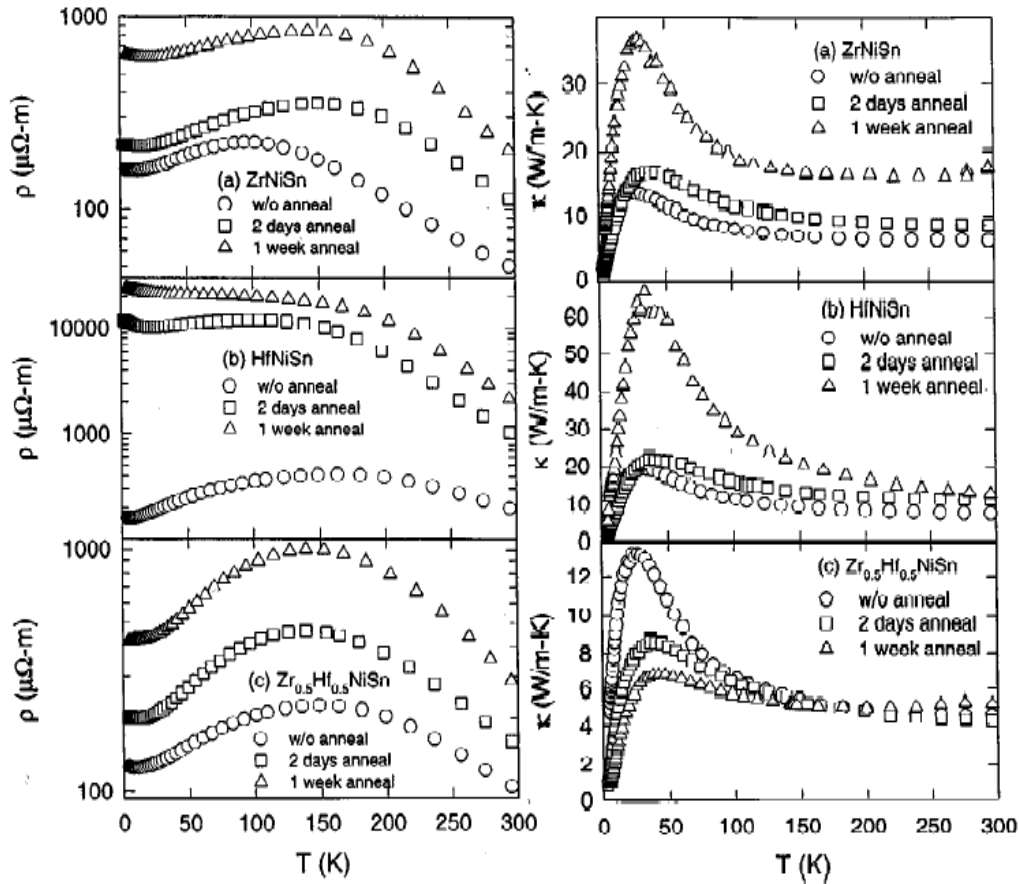
Figure 3-4 Half Hesuler properties are affected by annealing conditions[41]

Studies by Q.Shen studies also explored the enhancement of ZT by isoelectronic alloying of Hfat

Zr and Pd at Ni with1% Sb at Sn site [33].This resulted in reduction of thermal conductivity

without deterioration of power factor Consequently by multiple substitutions at Zr, Ni and Sn

sites highest value Q.Shen achieved dimensionless figure of merit is reported to be 0.7 at

700K[33] Hiroaki Muta instead was successful in improving ZT 0.48 at 900 K by substitution Ti

at Zr[47]. With the development of n type half Heusler compounds studies are also focused on

into search of p-typ half Hesuler compounds as candidates of advanced bulk thermoelectric

materials. The most extensively studied type half Heusler compounds are ZrPtSn, ErPdSB and

ErPdBi[23, 24]. Lanthanide based half Heusler, LnNiSb(Ln=Td Dy,Ho Er Tm) are also known

to show p-type characteristic with promising thermoelectric properties[24, 25]. Ting Wu reported

the effect of substitution of Fe to Co on TiCoSb with in situ introduction of TiO_2 particles during

the synthesis with increasing Fe content[51]. The maximum ZT of $TiFe_{0.15}Co_{0.85}Sb$ at 850 to be

0.45. Chemical substitution of Sn. in ErNiSn type increases the carrier concentration with

subsequent decrease in resistivity and increase in power factor[52]. Recently Xiao Yan and co-

workers have been successful in .boosting ZT in $Zr_{0.5}Hf_{0.5} CoSb_{0.8}Sn_{0.2}$ to 0.8 at 700˚C [32].By

nano structuring they are able to increase thermopower and decrease thermal conductivity by

30% relative of cast ingot of $Zr_{0.5}Hf_{0.5} CoSb_{0.8}Sn_{0.2}$ .A summary of the thermoelectric

performance of the state-of-the-art half Heusler materials fabricated by different techniques is

shown in Fig 3.5.
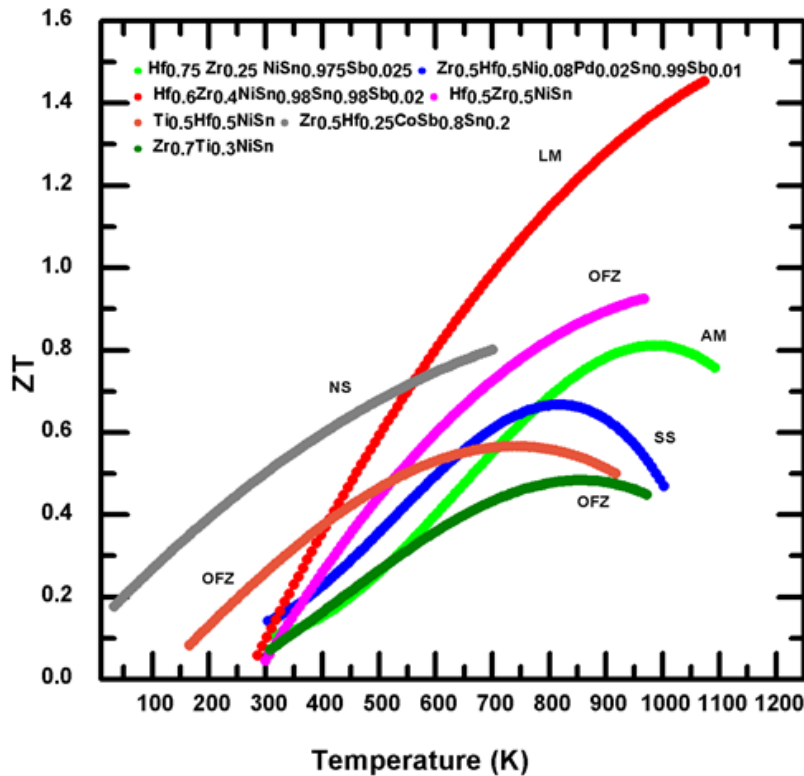
Figure:3-5 Temperature dependent figure of merit half- Heuslers fabricated by various methods. (LM= Levitation method, AM= Arch melting, OFZ=Optical floating zone, SS=Solid state, and NS= Nano structuring)[26, 32, 33, 48-50]

3.3 References

[1]   F. Heusler, W.Strack, and Haupt, Verh.Deutch. Phys. Ges 5 (1903) 219.

[2]   W. Jeitschko, Metallurgical and Materials Transactions B 1 (1970) 3159.

[3]   Nowotny H and B. K, Monatsh.Chem 81 (1950) 488.

[4]   R. Juza and F.Hund, Anorg. Allg. Chem (1948) 257.

[5]   R. H. Forster, G. B. Johnston, and D. A. Wheeler, J. Phys. Chem. Solids 29 (1968)

[6]   T. Graf, S. S. P. Parkin, and C. Felser, Magnetics, IEEE Transactions on 47 (2011) 367.

[7]   P. Villars, L. D. Calvert, and W. B. Pearson, Pearson's handbook of crystallographic data for intermetallic phases, American Society for Metals, Metals Park, Oh, 1985.

[8]   F. G. Aliev, N. B. Brandt, V. V. Moshchalkov, V. V. Kozyrkov, R. V. Skolozdra, and A. I. Belogorokhov, Zeitschrift für Physik B Condensed Matter 75 (1989) 167.

[9]   F. G. Aliev, V. V. Kozyrkov, V. V. Moshchalkov, R. V. Scolozdra, and K. Durczewski, Zeitschrift für Physik B Condensed Matter 80 (1990) 353.

[10]   B. A. Cook, J. L. Harringa, Z. S. Tan, and W. A. Jesser, in Proceeding ICT1996:15th Int. Conf. on Thermoelectrics, IEEE, Piscataway, NJ, 1996, p. 122.

[11]   S. Ogut and K. M. Rabe, Physical Review B 51 (1995) 10443.

[12]   P. Larson, S. D. Mahanti, and M. G. Kanatzidis, Physical Review B 62 (2000) 12754.

[13]   Dwight A E, Journal of Less Common Metals 34 (1974) 279.

[14]   K. Hem Chandra and et al., Journal of Physics D: Applied Physics 39 (2006) 776.

[15]   V. Ponnambalam, Y. Xia, S. Bhattacharya, A. L. Pope, S. J. Poon, and T. M. Tritt, in Int. Conf. Thermoelectr., Vol. 24th, 2005, p. 379.

[16]   C. Uher, J. Yang, S. Hu, D. T. Morelli, and G. P. Meisner, Physical Review B 59 (1999) 8615.

[17]   Y. Xia, V. Ponnambalam, S. Bhattacharya, A. L. Pope, S. J. Poon, and T. M. Tritt, Journal of Physics-Condensed Matter 13 (2001) 77.

[18]   K. Mastronardi, D. Young, C. C. Wang, P. Khalifah, R. J. Cava, and A. P. Ramirez, Applied Physics Letters 74 (1999) 1415.

[19]   J. Pierre, R. V. Skolozdra, J. Tobola, S. Kaprzyk, C. Hordequin, M. A. Kouacou, I. Karla, R. Currat, and E. Leliévre-Berna, Journal of Alloys and Compounds 262-263 (1997) 101.

[20]   J. Tobola and J. Pierre, Journal of Alloys and Compounds 296 (2000) 243.

[21]   J. Tobola, J. Pierre, S. Kaprzyk, R. V. Skolozdra, and M. A. Kouacou, Journal of Physics: Condensed Matter 10 (1998) 1013.

[22]   Hem Chandra Kandpa, Claudia Felser, and d. R. Seshadri, JOURNAL OF PHYSICS D: APPLIED PHYSICS 39 (2006) 776.

[23]   Y. Kimura and A. Zama, Applied Physics Letters 89 (2006) 172110.

[24]   T. Sekimoto, K. Kurosaki, H. Muta, and S. Yamanaka, Journal of Applied Physics 99 (2006) 103701.

[25]   T. Sekimoto, K. Kurosaki, H. Muta, and S. Yamanaka, Applied Physics Letters 89 (2006) 092108.

[26]   C. Yu, T.-J. Zhu, R.-Z. Shi, Y. Zhang, X.-B. Zhao, and J. He, Acta Materialia 57 (2009) 2757.

[27]   C. Kloc, K. Fess, W. Kafer, K. Friemelt, H. Riazi-Nejad, and E. Bucher, in Proceeding ICTP96, IEEE, Piscataway, NJ, 1996, p. 155.

[28]   Y. Xia, S. Bhattacharya, V. Ponnambalam, A. L. Pope, S. J. Poon, and T. M. Tritt, Journal of Applied Physics 88 (2000) 1952.

[29]   S. Bhattacharya, A. L. Pope, R. T. Littleton Iv, T. M. Tritt, V. Ponnambalam, Y. Xia, and S. J. Poon, Applied Physics Letters 77 (2000) 2476.

[30]   H. Hohl, A. P. Ramirez, C. Goldmann, G. Ernst, B. Wolfing, and E. Bucher, Journal of Physics: Condensed Matter 11 (1999) 1697.

[31]   S. Sportouch, P. Larson, M. Bastea, P. Brazis, J. Ireland, C. R. Kannewurf, S. D. Mahanti, C. Uher, and M. G. Kanatzidis, in Mater. Res. Soc. Symp. Proc., Vol. 545, MRS, Warrendale, PA, 1999, p. 421.

[32]   X. Yan, G. Joshi, W. Liu, Y. Lan, H. Wang, S. Lee, J. W. Simonson, S. J. Poon, T. M. Tritt, G. Chen, and Z. F. Ren, Nano Letters 11 (2011) 556.

[33]   Q. Shen, L. Chen, T. Goto, T. Hirai, J. Yang, G. P. Meisner, and C. Uher, Applied Physics Letters 79 (2001) 4165.

[34]   X. Y. Huang, Z. Xu, L. D. Chen, and X. F. Tang, Key Engineering Materials 249 (2003) 79.

[35]   B. R. K. Nanda and I. Dasgupta, Journal of Physics-Condensed Matter 15 (2003) 7307.

[36]   R. A. de Groot, F. M. Mueller, P. G. v. Engen, and K. H. J. Buschow, Physical Review Letters 50 (1983) 2024.

[37]   J. Boeuf, University of Karlsruhe, 2003.

[38]   K. Endo, J. Phys. Soc. Jpn. 29 (1970) 643.

[39]   R. B. Helmholdt, R. A. de Groot, F. M. Mueller, P. G. van Engen, and K. H. J. Buschow, Journal of Magn and Magn Mater 43 (1984) 249.

[40]   K. Kaczmarska, J. Pierre, J. Beille, J. Tobola, R. V. Skolozdra, and G. A. Melnik, Journal of Magnetism and Magnetic Materials 187 (1998) 210.

[41]   C. Uher, J. Yang, S. Hu, D. T. Morelli, and G. P. Meisner, Physical Review B 59 (1999) 8615.

[42]   J. H. Wernick, G. W. Hull, T. H. Geballe, J. E. Bernardini, and J. V. Waszczak, Materials Letters 2 (1983) 90.

[43]   S. Waki, Y. Yuji, and K. Mitsugi, J. Phys. Soc. Jpn 54 (1985) 1673.

[44]   G. Goll, M. Marz, A. Hamann, T. Tomanic, K. Grube, T. Yoshino, and T. Takabatake, Physica B: Condensed Matter 403 (2008) 1065.

[45]   G. J. Poon, in Semiconductors and Semimetals, Vol. Volume 70 (M. T. Terry, ed.), Elsevier, 2001, p. 37.

[46]   V. M. Browning, S. J. Poon, T. M. Tritt, A. L. Pope, S. Bhattacharya, P. Volkov, J. G. Song, V. Ponnambalam, and A. C. Ehrlich, MRS Online Proceedings Library 545 (1998)

[47]   H. Muta, T. Yamaguchi, K. Kurosaki, and S. Yamanaka, in Thermoelectrics, 2005. ICT 2005. 24th International Conference on, 2005, p. 351.

[48]   S. R. Culp, S. J. Poon, N. Hickman, T. M. Tritt, and J. Blumm, Appl. Phys. Lett. 88 (2006) 042106.

[49]   Yoshisato Kimura, Tomoya Kuji, Akihisa Zama, Taiki Lee, and Y. Mishima., in 2006 MRS Fall Meeting,MRS Symposium Proceedings, Vol. 980, Boston, MA, USA, 2007, p. 211.

[50]   Y. Kimura, H. Ueno, and Y. Mishima, Journal of Electronic Materials 38 (2009) 934.

[51]   T. Wu, W. Jiang, X. Li, Y. Zhou, and L. Chen, Journal of Applied Physics 102 (2007) 103705.

[52]   K. Kawano, K. Kurosaki, T. Sekimoto, H. Muta, and S. Yamanaka, in Thermoelectrics, 2007. ICT 2007. 26th International Conference on, 2007, p. 267.

CHAPTER 4

SYNTEHSIS AND CONSOLIDATION

4.1Introduction

Properties of thermoelectric materials beside the quality of samples also depend upon the alloying or synthesis methods even with same composition. Synthesis methods are mainly divided into two main categories: mechanical methods which include ball milling and chemical methods such as are arch melting and ceramic[1] (solid state reaction at high temperature).We will use the term Direct method for ceramic synthesis because reactants are directly heated to produce the product without passing through the melt .There are many factors which are given consideration in the fabrication of materials such as cost and time required to complete the synthesis is important from the commercial and research point of view. If a method is time consuming it cannot be preferred for manufacturing. It has been investigated, diamond requires high pressures during synthesis, but graphite does not[2]. Due to the extreme synthetic conditions and high cost of synthetic diamond, it is not industrialized. Stoichiometric is another key factor in the preparation of solid synthesis because properties like carrier concentration and thermal conductivity are affected to a great extent. Furthermore purity and the quality of starting materials is also essential to ensure that the right products will be obtained[3, 4].Considering all these factors, synthesis reported in this work was done by Direct method inside the glove box in the presence of argon. One part of our study is focused to investigate the behavior of NiO nano powder in half Heusler matrix by using different mixing methods. We mixed NiO nanopowders and half Heusler host matrixes by ball milling for short interval of time. In this chapter we will give brief introduction of Direct method, Ball Milling and consolidation methods such as Isotatic

hot pressing and Spark plasma. Later we will give explanation the procedure we adopted for the synthesis of $Zr_{0.5}Hf_{0.5}Ni_{1-x}Pd_xSn_{0.99}Sb_{0.01}$. All the composites samples were consolidated by uniaxial hot pressing.

4.1.1 Direct method

Solids are not usually ready to react with each other at room temperature, and thermoelectric and most of the refractory solids require high temperature typically 500°C - 2000°C to complete the synthesis without use of pressure[1]. This is the most common method used in the synthesis of thermoelectric material and solids from solids. Moreover this solid state synthesis is beneficial for less cost and does not require any solvents.

Besides economical reason this synthesis approach is favorably employed to fabricate great number of compounds that are not stable with respect to oxygen and water. These compounds include half Heusler mixed metal oxides, sulfides, nitrides, aluminosilicates and many others[3] and are used both research purpose and industry. Furthermore not only reactants are sensitive to oxygen and moisture but also product. Therefore direct synthesis requires inert atmosphere for mixing and heating depending on the temperature required for the synthesis. Argon is used to inhibit oxidation to higher oxidation state, hydrogen when low oxidation state is needed and oxygen to assist the formation of high oxidation state.[3].

4.1.2Reaction Vessels

In the synthesis process caution must be given to the reaction vessels which are used use for mixing. They have to be sufficiently inert so that they do not participate in any reaction. They should also be able to withstand high temperature in order to provide a safe environment for reactants.

Figure:4-6 Commercial inert atmosphere chamber(glove box) used for mixing half-Heusler samples

There are various reaction vessels which are available commercially such as made of quartz (to1273 K),silica (to 1430 K), alumina (to 2000 K), zirconia (to 2300 K) or magnesia (to 2700 K) commonly used[3]. Depending on the reactant, metals such as platinum, tantalum, and graphite linings are also used in some cases[4]. Usually, reaction vessels need to be evacuated and sealed before reactions. Figure 4.2 shows an evacuation system with silica reaction tubes we used in in this research study. Different furnaces are available for the synthesis at different temperatures. Tube furnaces are used for the reaction at high temperature around<1900K. For moderate temperature reactions <1273 box furnace is favorable. For compounds which require higher temperatures up to 2274K for synthesis induction furnace is best choice

Figure:5-7 An evacuation system with silica tubes connected to the vacuum line

4.1.3 Procedure

The purity of the starting material is extremely important because once the reaction is completed there is no method available to purify the product. To ensure the product/sample should not have unwanted impurities, the stoichiometric ratio of starting materials are weighed accurately, mixed thoroughly by hand grinding and mechanically inside the glove in the presence of inert atmosphere and the homogenous mixture is then heated until they reaction is completed[4, 5]. In solid state, it is not easy to achieve a homogeneous mix of the reactants even after thorough grinding. If the diffusion rate is slow it might also take infinite time to obtain a pure phase by single cycle of heating. Hence, after first heating, products can be collected, ground to fine powder and annealed again. During the second annealing, fresh surfaces which might have been far away from each other in the first heating can be in contact more closely after being reground. This procedure can be repeated several times until the targeted compound is

obtained without any side products. The standard method to determine the extent of reaction and formation of required phase is powder X-ray diffraction.

4.1.4 Principle

In the formation of solid solutions the solid state reactions usually take place at the interface of the two or more solids, and the reactants continuously diffuse toward the interface and finally form a homogeneous new solid phase. The Figure 4.1 illustrates a solid-state reaction between two solids A and B with a contact across one face. The reaction proceeds with the nucleation of product C at the interface of A and B. It is to be noted that the reaction can only start at the contact points if there is no melting phase present. In case there is such phase present at the contact the process may become difficult and requires some degree of structural reorganization. After nucleation, new interfaces are formed with the formation of product layer C. The two interfaces which are formed are, one between A and C and the other between B and C. For additional reaction to take place ions or atoms of A or B must diffuse through the product C layer[5].The product layer C grows and becomes thicker as the reaction continues and this increases diffusion time with slower rate of reaction. For simple cases, where the rate of the reaction is controlled by lattice diffusion through a planar layer, the rate can be expressed by Fick's Law[6]:

$$\frac{dx}{dt} = -\frac{k}{x} \qquad\qquad (4\text{-}1)$$

where x is the thickness of the product layer, t is the time and k is the rate constant. In order to have a good rate of reaction high temperature is beneficial. According Tamman's general rule[3], the temperature of solid-state reactions should be above two-thirds of one component's melting temperature to activate the diffusion, since ions or atoms are usually trapped on their appropriate lattice.
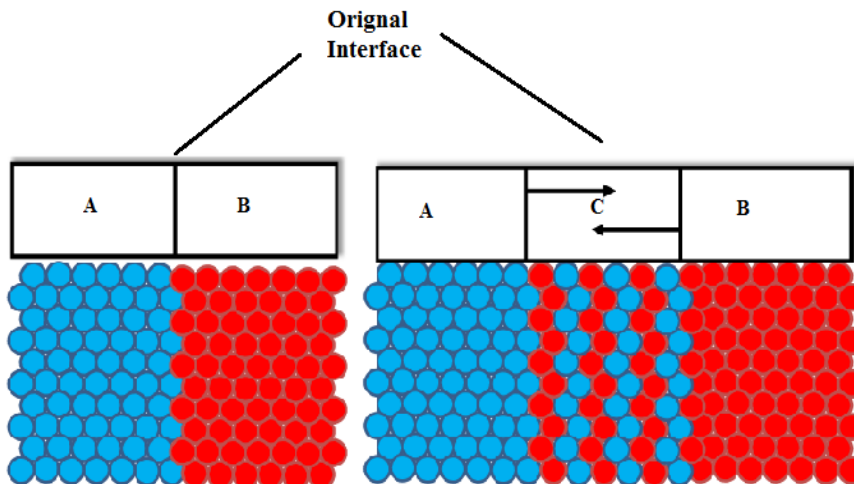
Figure:4- 8Reaction of between A and B and formation of product C

Thus we can conclude that the rate of a solid-state reaction is mainly depends on three factors[5]

i. The contact area between the reacting compounds.

ii. The nucleation rate of the product.

iii. Diffusion rates of ions through different phases, especially the product phase.

In the solid state synthesis diffusion is the limiting step in the whole reaction process so to overcome this thorough grinding of starting material to get fine homogeneous powder is required to achieve a reasonable rate of reaction. If the fine powdery compound obtained after mixing is sensitive to water or oxygen sensitive decomposition will be accelerated. Nevertheless direct method synthesis at high temperature should be carried out in the presence of inert atmosphere.

4.1.5 Disadvantages

The direct method though cost effective method but suffers from several disadvantages. The major drawback of this synthesis method is that there is no way to screen the progress of reaction. When no melting phase is formed during the course of reaction, the entire reaction has to occur in the solid state, by a phase boundary reaction at the points of contact between the

reactants and later by diffusion of the reactants through the product phase. As the reaction advances diffusion paths become progressively longer and the reaction rate slows down. The product interface between the reacting particles acts as obstacle. The reaction may be accelerated up to certain extent by intermittent grinding between heating cycles. It is only by trial and error method y that one decides on appropriate conditions that lead to completion of the reactions of the reactions. Because of this difficulty one frequently ends up with mixtures of reactant and products which will form various phases. Separation of the desired product from these mixtures is generally complicated. Consequently if not impossible it is sometimes difficult to obtain a compositionally homogenous product by direct method even when the reaction proceeds almost to completion.

4.2.1 Mechanical Alloying

This approach is employed to fabricate solid state solution without using high temperature. Furthermore in the direct method rate of diffusion is enhanced if particle size is small. Sometimes after the product is performed by direct synthesis mechanical alloying also called mechanical attrition is employed to reduce particle size. Mechanical alloying is based on comminuation process, a process by which small particles are produced by crushing grinding and milling by mechanical forces. This is most frequently used method to achieve and single phase compound with size reduction by material scientists and to improve the thermoelectric transport properties. The size reduction in the thermoelectric material is advantageous to decrease the thermal conductivity [7]. J. D. Germond investigated ZrNiSn alloy synthesized by mechanical alloying and found that this material has lower thermal conductivity than the arc melted sample of same composition Fig (4-4) [7]. The mechanical alloyed samples were consolidated by two methods: 1) uniaxial hot press and 2) spark plasma sintered. This has been recognized that

93

thermoelectric figure of merit of materials synthesized by ball milling followed by sintering is comparable to that prepared by arc melt [8, 9]
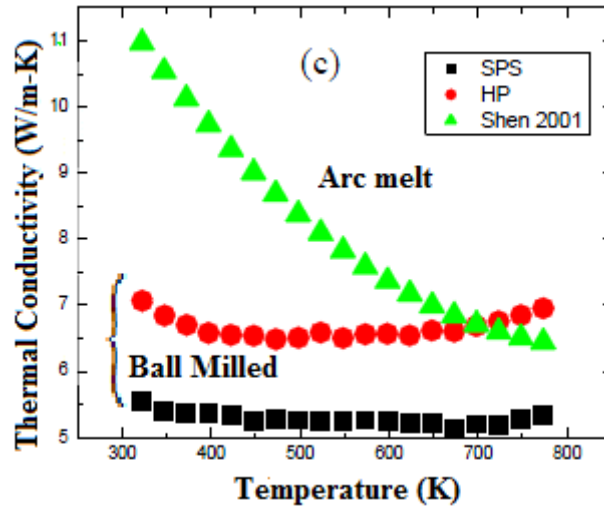
Figure: 4-9. Temperature dependent thermal conductivity of ZrNiSn fabricated by mechanical alloying using traditional shaker ball is lower as compared to arc melted sample by Shen [10]

Ball mills are categorized into various types such as tumbler, vibrator or agitator depending on the method used to impart motion to the balls. Ball milling is usually used to produce particle sizes ranging from ~10μm to as low as a fraction of a micrometer Grinding jars and balls are available in several different materials such as agate silicone nitrite, zirconia, chrome steel, chrome-nickel steel and tungsten carbide.

The comminuation of solid material depends upon utilization energy utilization defined as ratio of the new surface area created to the total mechanical energy supplied [1]. High utilization energies have high rate of grinding and particle size of given range is achieved in shorter time. In ball mill commination occurs by compression, impact and shear between the moving ball and the particles. The grinding particles travel at different velocities. Therefore collision force, direction and kinetic energy between two or more elements vary greatly.

The rate of grinding depends upon several factors such as mill parameters, the properties of grinding medium (balls or rods) and amount of material to be grounded[1]. Small milling balls are better than the bigger one mainly for two major reasons: 1) several smaller balls provide a larger number of contact points as compared to fewer larger balls and 2) smaller balls reduce danger of overheating. Ball mills that run at low speeds contain large balls in order to get high enough kinetic energy for transfer to the particles. High speed mills can contain small balls to provide a similar amount of kinetic energy. The most commonly formula to estimate the milling rate showing the dependence of milling on particle size and ball size is given by[1]

$$Rate\ of\ milling \approx A a_{mill}^{1/2} \frac{\rho_{ball} d_{particle}}{r_{ball}} \qquad (4\text{-}2)$$

Where A is constant that is specific to the mill being used and material being milled a_{mill} is the radius of the mill, ρ_{ball} density of the balls r_{ball} radius of the balls and $d_{particle}$ is the particle size. The Equation 4-2 shows that the rate of grinding also depends on the particle size of material to be milled. This is important because the grinding limit is achieved when there is no further reduction in size is noticeable and makes grinding difficult [11] Thus the rate falls off with decreasing particle size

Whereas mechanically alloying has advantage of fabricating the material without requiring extreme high pressure and temperature but alloying by ball milling it has shortcomings such as

1. Wear of grinding medium fairly high.

2. Particles get clogged at the base of milling cylinder.

3. Noise during working

4. Friction heating of material.

The planetary ball mill is good for mixing and solids are ground by large centrifugal force. The intensity of acceleration can be controlled. The jar containing the grinding media rotates about two separate parallel axes. The jar rotates in the direction opposite to the planetary with speed different from planetary arm.

.

Figure :4-10 Planetary mill consists of revolving base disk and rotating jars

To compare how the mixing method influence the transport properties we used planetary ball mill to disperse and break the agglomerate NiO nanoparticles in half Heusler by, planetary ball mill and compare the thermal conductivity with those composite samples prepared without milling.

4.3 Compaction

Powder metallurgy employs various methods for compacting and shaping of powders. The most popular methods are rigid die compaction metal injection molding, extrusion, spark plasma, hot isostatic compaction, and uniaxial hot pressing. Spark Plasma Sintering (SPS) anduniaxial hot pressing (HP) techniques are commonly used for the densification of thermoelectric materials. We will discuss only these two with some important details

4.3.1 Uniaxial Hot Press

The primary consolidation route which was adopted in this research work is uniaxial hot pressing. Modeling of the HP process typically focuses on the densification of the powders, and not the transformations taking place within the powders. The densification has been described as a three-step process, beginning with loose packing of powder in the die, elimination of connected porosity due to the growth of necks at contact points between adjacent particles, and reduction of the size of individual pores. The growth of necks and filling in of pores at each stage is takes place primarily through plastic deformation of the particles, the so-called power-law creep, and mass diffusion between the particles' free surfaces.

### 4.3.2 Description of hot-pressing unit

The matrix phase and the nanocomposites were consolidated by uniaxial hot pressing unit, Thermal Technology, Inc [12] which is designed for simultaneous application of high temperature and high pressure. The hot press unit is capable of reaching temperatures as high at 2000^{0}C and pressure as high as 100MPa. The system has two vertically aligned steel rams with threaded extensions to which high-density custom made pyrolytic graphite attachment are screwed into pyrolytic graphite has low thermal expansion coefficient and high compressive strength and the press ram is easily machinable into a cylinder. The hot press chamber is

enclosed by a vertical furnace that uses graphite heating element so that very high temperatures can be attained. The furnace chamber can be raised and lowered by the hydraulics. The furnace chamber rests upon an O-ring seal on the bottom when in the lowered position.

Three set screws are used to seal the chamber and give a control over the quality of vacuum in the chamber. Roughing and turbo pump allows the chamber to be evacuated to the order of 10^{-5} Torr. The gate valve of the turbo is opened/closed using neumatic valves, controlled by pressure of the compressed air. It is possible to perform hot pressing under high vacuum or under flowing inert gas or even under positive pressure. For the experiments carried out for the present work, temperatures as high as 1000^0C were sufficient. Optical pyrometer is also used as a primary sensor and a thermocouple is used as a secondary sensor to read the temperature inside the chamber. At the highest temperature the difference in temperature read by the two sensors were ~10^0C. The sample dies are also manufactured using pyrolytic graphite cylinders and are machined to have lengths of 101 mm, outer diameter (OD) of 76mm and inner diameter (ID) of 10mm. The graphite dies are aligned in line with the two vertically aligned pressing and eject rams, and the alignment is a crucial parameter to be monitored before starting the hot-pressing. A small misalignment can cause a crack in the plunger or die and damaged fragments of the broken die can damage the graphite heating element.

The hydraulics in the hot press unit exerts force (measure in kg) on the die and depending on the area of cross-section of the die on which the force is being exerted, the pressure exerted on the die is calculated as $P=F/A$. For example, a force of 800 kg applied on a plunger of 10mm diameter corresponds to a force of 100 MPa. The diagram of the hot press unit used for the hot pressing of samples reported in this thesis is shown in the Fig 4-6.
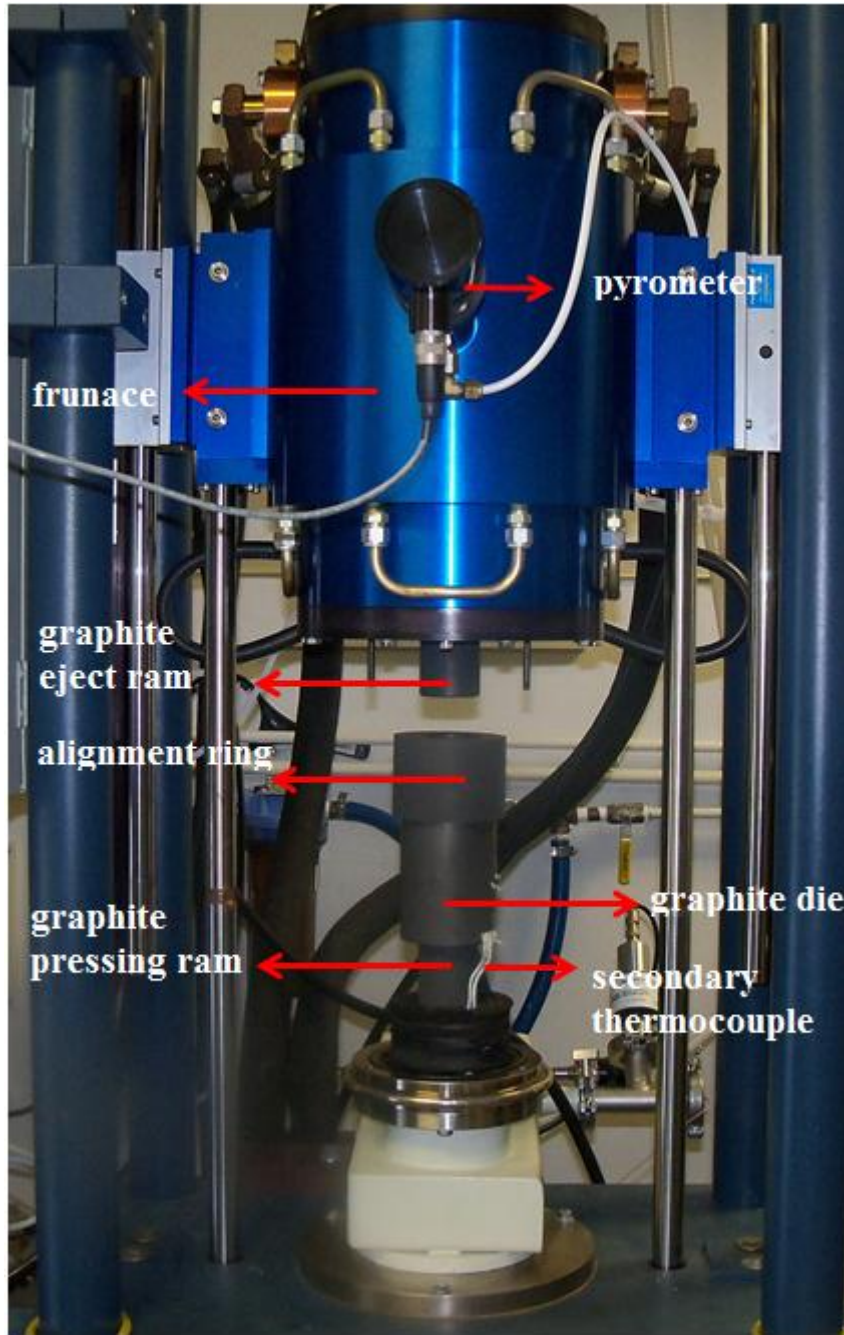
Figure: 4-11 Uniaxial hot press by Thermal Technology, Inc used for hot pressing of Half Heusler and nanocomposites.

4.3.3 Procedure

The sample powder is sandwiched between two graphite anvils, inside a graphite die. In order to avoid the pellet sticking to the anvil and prevent contamination, anvils are coated with boron nitride solution and thin graphite having a diameter slightly above the ID of the graphite die, is inserted into the die to serve as a buffer between the sample and the graphite anvils. The graphite die is placed inside the furnace chamber and held between pressing and eject ram, and the pressure is applied using the hydraulic system. The graphite die with sample is aligned in line with pressing and eject ram. The furnace is lowered to and sealed using the set screws, and evacuated to attain a 10^{-6} torr vacuum. The temperature ramping and pressure ramping are controlled by a dual programmer, which has the ability to ramp both the temperature and pressure simultaneously. The temperature is ramped to the maximum temperature of (850^0C-900^0C) at a rate of 10^0C/min and force is ramped to the maximum of 801Kg at 15Kg/min. The pressure reaches 100 MPa in 50 min which equates to 801Kg of force. The sample is heated inside the evacuated chamber to the maximum temperature. The temperature is allowed to dwell at the maximum temperature for 120 min. The pressure is allowed to dwell at 100 MPa for 300 min to ensure that while the temperature is ramping down, the graphite die is still under the maximum pressure. This ensures higher densities of the pellet observed from our experiments.

The nanocomposite samples were consolidated by adding appropriate volume fraction of nanoinclusions into the matrix phase. The nanoparticles and the matrix phase were intimately mixed by hand grinding for 30 min and the resultant powder was hot pressed under conditions similar to the matrix phase for comparison of thermoelectric properties.

4.3.4 Spark Plasma Sintering (SPS)

Spark plasma sintering (SPS), as the name shows, is a unique thermal consolidation environment assisted by inducing electric spark by microwave or induction field .This plasma heating is high speed consolidation and sintering process is expected to find increased application for processing ceramic and thermoelectric materials. SPS' operational temperatures (200-2400°C) are commonly 200 to 500°C lower than with conventional sintering[12]. In contrast to the HP which uses heat and pressure to increase grain sizes, SPS uses a large pulsed current and the contact resistance between sample grains to weld the powders together without significant grain boundary growth. The relatively low temperatures in SPS combined with fast processing time (pressure and temperature ramping up and hold time) has potential of tight control over grain growth and microstructure. This results in the consolidation of homogeneous high density and high quality samples in significantly less time because of uniform and fasting heating than those processed by a hot pressing. Half Heusler matrixes with 20% and 40% Pd content were consolidated by SPS techniques for comparison. These samples were consolidated by our collaborator at GM motor. The same sintering profile was followed for both matrices. The sample was placed under uniaxial pressure of 50 MPa in a sintering die. The temperature was ramped from 25°C at rate of 75°C/min to reach the final temperature of 825°C. The sample was held at 825°C for an addition 7 minutes until thermal expansion was observed on the specimen displacement readout. The consolation was done under a dynamic vacuum of less than 2 Pa.

4.4 Synthesis of $Zr_{0.51}Hf_{0.5}Ni_{1-x}Pd_xSn_{0.01}Sb_{0.01}$

Half-Heusler samples of Pd series with formula $Zr_{0.5}Hf_{0.5}Ni_{1-x}Pd_xSn_{0.01}Sb_{0.01}$ were prepared by the method described in section 4.1.1.
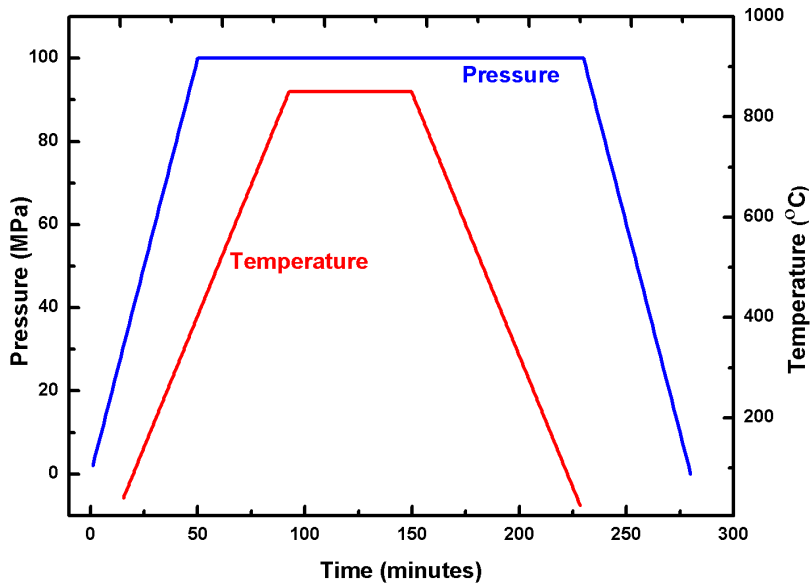
Figure: 4-12 Heating profile for pressing half Heusler and composites samples

Starting materials, zirconium (powder, -100 mesh, 99.95%), nickel (powder, -200 mesh, 99.9%) hafnium (powder, 99.99%), antimony (powder, -100 mesh, 99.5%), and in (powder, -100 mesh, 99.5%) and were acquired from Alfa Aesar; palladium (powder, -50 mesh, 99.9%) and Ni(powder, -100 mesh, 99.9%) were purchased from Aldrich. All the elements were weighed in the desired stoichiometric ratio according to reaction equation:

$$(0.05)Zr + (0.05)\,Hf + (1-x)Ni + x(Pd) + (0.99)Sn + (0.01)Sb \rightarrow Zr_{0.5}Hf_{0.5}Ni_{1-x}Pd_xSn_{0.99}Sb_{0.01} \qquad (4\text{-}3)$$
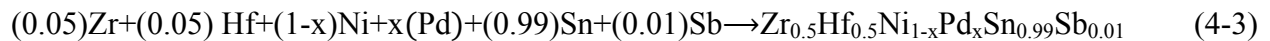
under exclusion of oxygen and moisture in an argon filled glove box then mixed and loaded into into silica tubes inside the glove box. These tubes were covered tightly with Parafilm M and taken out from the glove box. To avoid the presence of oxygen and moisture the tubes were sealed under vacuum. The vacuum needed for sealing the tubes was obtained by Edward's rotary oil pump. The vacuum pressure was in the order of 10^{-3} mbar. Sealing of the tubes is followed by

heating in box furnaces to final temperature of 900˚C over a period of 72 hours. The ramping rate was 75˚C /hour. Heating profile is shown in Fig 4-8.
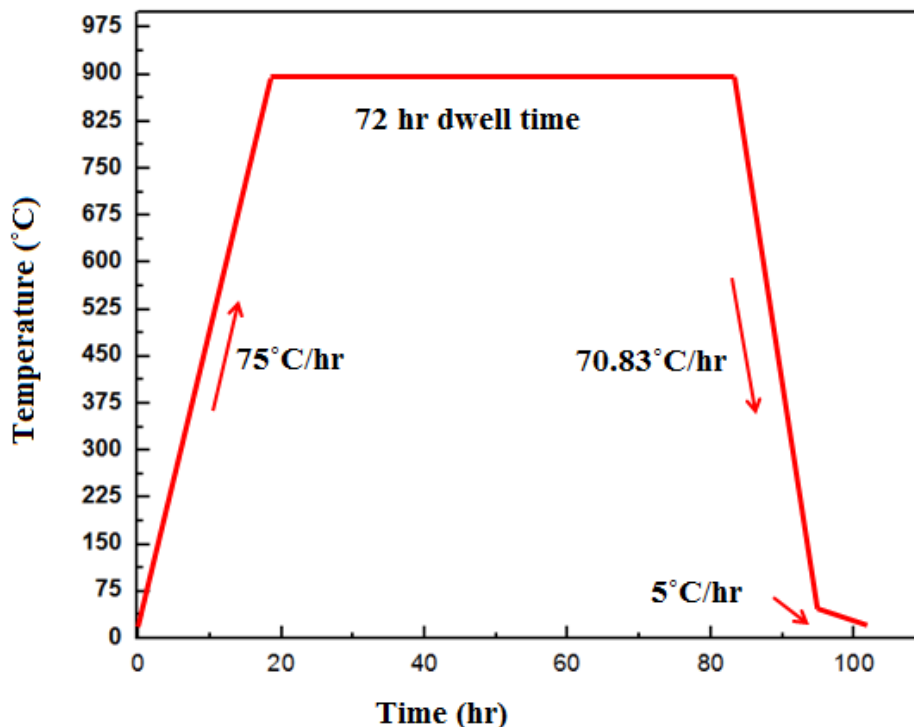
Figure:4-13 Heating profile for the synthesis of half-Heusler by Direct Method

Allowing long reaction times increases the possibility of obtaining a homogenous sample. At the end of first heating cycle the samples were thoroughly ground and powder X-ray diffraction was recorded utilizing PANalytical Xpert powder diffractometer using CuKα radiation. We scanned 2θ range of 15-75˚ in steps of and at a rate of five seconds per step. The solid solutions of half Heusler crystallized in cubic MgAgAs- type structure. The presence of any side peaks other than half Heusler peaks indicates the presence of either other phases or reaction is incomplete. When extra peaks were seen in PXRD, the samples were reground, sieved, reloaded into the tube and repeated the whole synthesis using the same heating profile as in Fig. 4-8 In most cases, side

peaks are gone after second heating cycle. After the completion of heating process the grey, fine powdery samples were hot-pressed and high density pellets were obtained. The method of making pellets from hot pressed is explained in section 4.3.3. Half Heusler samples $Zr_{0.5}Hf_{0.5}Ni_{1-x}Pd_xSn_{0.99}Sb_{0.01}$ with x= 0.4 and x=0.2 were also consolidated by SPS method for comparison; this spark plasma sintering was done by a collaborator at General Motors.

4.5 Synthesis of NiO Nanoparticles

NiO nanoparticles were synthesized using $Ni(NO_3)_2.6H_2O$ as precursor and NaOH as a precipitating agent. The precursors were combined in 1:2 molar ratios in separate aqueous solutions. The reaction occurs in two steps and is given by

$$Ni(NO_3)_2 6H_2O+NaOH \rightarrow Ni(OH)_2+2NaNO_3 \tag{4-4}$$

$$Ni(OH)_2 \rightarrow Ni+H_2O \tag{4-5}$$
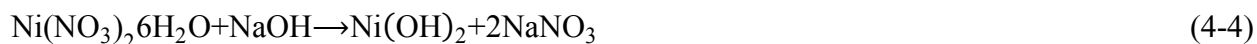
In the synthesis process, the sodium hydroxide solution was added slowly with constant stirring to the nickel nitrate hexahydrate solution until the precipitation of nickel hydroxide and sodium nitrate. The precipitate was washed with distilled water to dissolve all sodium nitrate from the $Ni(OH)_2$ gel. The sample was then rinsed with ethanol and dried in drying oven at 120°C. The resulting $Ni(OH)_2$ powder was calcined at 300°C to produce NiO nanoparticles. These surfactant free NiO nanoparticles were characterized using X-ray powder diffraction, transmission electron microscopy (TEM) and physiosorption/surface area analysis (Micromeritics ASAP 2020). A representative TEM image (Fig. 1) shows particles in the size range of 2-7 nm.
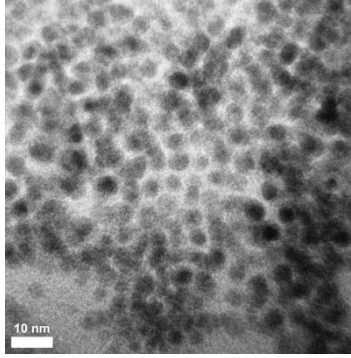
Figure:4-14 High magnification TEM Image of NiO nanoparticles after calcination at 300°C indicating the average size of the particles is in the range of 2-7 nm

4.6 Synthesis of HfO₂Nanoparticles:

The synthesis of HfO_2 nanoparticles was accomplished by a wet chemical technique known as "reverse micelle synthesis." 80 ml of cyclohexane was placed in a 125 ml flask with a magnetic stir bar. 0.5 ml Igepal CO-520 was injected into the flask and the mixture was stirred for 30 min under nitrogen atmosphere. 0.2 ml of NH_4OH was injected to the flask and stirred for another 5 min or until the reaction mixture became transparent. 0.4 ml of hafnium (IV) tert-butoxide was injected drop-wise with vigorous stirring. The reaction mixture was kept stirring for different intervals of time under continuous flow of nitrogen. The color transition from transparent to milky white suggested the formation of nanoparticles. The white product was precipitated by adding ethanol and centrifuged to separate the product. The product was first dried in air and then in an oven at 70 °C for one day.

4.7 Prepartion of Composites

The denisities of nano particles ρ_{nano} and half Heusler ρ_{nano} were meausred by using Pycnommetric apparatus and nano powder mass needed for required volome percentage is calculated by the equation

$$M_{nano} = \frac{V\% M_{req} \rho_{nano}}{\rho_{HH} - [V\%(\rho_{HH} - \rho_{nano})]} \qquad (4\text{-}6)$$

where $V\%$ is the volumetric % percent of nanopowder (3vol%, 6vol% and 9vol%) M_{req} total mass of composites required to make pellet.

4.7.1 NiO Half-Heusler Composites

The synthesized $Zr_{0.5}Hf_{0.5}Ni_{1-x}Pd_xSn_{0.99}Sb_{0.01}$ powders (see section 4.4) were mixed with 3 -6% (vol) NiO nanoparticles. The resulting powders were homogenized by using planetary ball mill (BM) for 20 minutes or dry mixing (DM) using a conventional mortar and pestle. The samples were labeled as Pd=0 if the host matrix is $Zr_{0.5}Hf_{0.5}NiSn_{0.99}Sb_{0.01}$ and Pd=0.2 for $Zr_{0.5}Hf_{0.5}Ni_{0.8}Pd_{0.2}Sn_{0.99}Sb_{0.01}$. The samples were also labeled according to the concentration of NiO nanoparticles, for example Pd=0.2/6%NiO-DM indicates $Zr_{0.5}Hf_{0.5}Ni_{0.8}Pd_{0.2}Sn_{0.99}Sb_{01}$ with 6% (vol) NiO nanoparticles homogenized by ball milling. Total yield of the mixture after mixing the nano powders was 2.9 g and total mass of the ball was 38 g.

4.7.2 HfO$_2$ Half-Heusler Composites

The mass of HfO$_2$nanopowders requried for making 3-9% vol composites of half-Heusler was estiamted from equation All the HfO$_2$ half-Hesuler powders were mixed for 30 minutes by hand thoroughly in an agate mortar inside the glove box.

Once the sysnthesis was completed the samples were ready for consolidations.All the half-Heusler samples of $Zr_{0.5}Hf_{0.5}Ni_{1-x}Pd_xSn_{0.99}Sb_{0.01}$ series and their composites with NiO and HfO$_2$ prepared in sections 4.4, 4.7.1 and 4.7.2 were consolidated by the method explained in section 4.3.3. After densificatin the disk shaped pellets were mirror polished and were ready for thermal diffusivity measurement.(Section). Disks were later on cut with wire saw into bars of ~2×2×8mm for Seebeck and Hall effect measurements.

4.8 References

[1]   M. N. Rahaman, Ceramic Processing, CRC Press, 2006.

[2]   K. E. Spear and John P. Dismuhes, In Synthetic Diamond: Emerging CVD Science and Technology, Wiley-Interscience, 1994.

[3]   A. R. West, Solid State Chemistry and Its Applications, John Wiley and Sons, New York, NY, 1990.

[4]   L. E.Smart and Elaine A. Moore, Solid State Chemistry: An Introduction, CRC press, Boca Raton, FL, 2005.

[5]   U Schubert;N Hüsing, Synthesis of Inorganic Materials, Wiley-VCH, Weinheim Germany, 2005.

[6]   E. L. Knuth, Physics of Fluids 2 (1959) 339.

[7]   J. D. Germond, P. J. Schilling, N. J. Takas, and P. F. P. Poudeu, in Thermoelectric Materials-Growth, Properties, Novel Characterization Methods, and Applications, Mater. Res. Soc. Symp. Proc., Vol. 267 (J. D. Baniecki, ed.), MRS, Warrendale, PA, 2010 p. 1267.

[8]   T. Tokiai, T. Uesugi, K. Fukumoto, A. Hirayama, K. Ito, T. Ohta, and T. and Kajikawa, in Proc. 1992 Spring Meeting of the Japan Institute of Metals, Tokyo, 1992
.

[9]   B. A. Cook, B. J. Beaudry, and J. L. Harring, and Barnett, W.J.,, in Proc. IX Int. Conference on Thermoelectrics, California Institute of Technology,Pasadena1990.

[10]   Q. Shen, L. M. Zhang, L. D. Chen, T. Goto, and T. Hirai, Journal of Materials Science Letters 20 (2001) 2197.

[11]   J. K. Beddow, Particulate Science and Technology, Chemical Publishing Comany, NewYork, 1980.

[12]   L. Thermal Technology, 1911 Airport Blvd Santa Rosa,CA 95403.

CHAPTER 5

EXPERIMENTAL RESULS AND DISCUSSION

5.1 Overview

As discussed in the beginning of this study that our goal is to investigate the thermoelectric properties of $Zr_{0.5}Hf_{0.5}Ni_{1-x}Pd_xSn_{0.99}Sb_{0.01}$ and incorporate NiO and HfO_2 nano-particulate in the half Heusler matrixes of this series having superior properties. To achieve our goals, the synthesis of $Zr_{0.5}Hf_{0.5}Ni_{1-x}Pd_xSn_{0.99}Sb_{0.01}$ alloy with compositions of $0 \leq x \leq 1$ was performed by a solid-state reaction as discussed section 4.4. NiO nanoparticles prepared by hydrothermal process see section (4-5) 3% and 6% by volume were mixed into half Heusler matrix with no Pd and 20% Pd concentration by dry mixing, wet mixing and ball milling. Nanometer-sized HfO_2 inclusions ($\approx$4 nm) in diameter were also added into same host matrices to make comparison of transport properties among the host half Heusler phases, NiO half-Heusler composites and HfO_2 half Heusler composites. All compounds were densified by unidirectional hot press (see section 4.3.3). For comparison samples with composition x=0.2 and x=0.4 were also pressed by spark plasma. The resulting pellets were cut with wire saw into bars $\approx 2 \times 2 \times 8$ mm and 2 mm thick disks to measure Seebeck coefficient, electrical resistivity and room temperature Hall effect measurements. Electrical resistivity and Seebeck coefficient measurement were carried out using a commercial system (ZEM 3 ULVAC). Thermal conductivity was estimated from thermal diffusivity data obtained from laser flash using Netzsch 457.Microflash system, on the disk shape samples The relative densities of all hot pressed $Zr_{0.5}Hf_{0.5}Ni_{1-x}Pd_xSn_{0.99}Sb_{0.01}$ pellets were measured with respect to theoretical density.
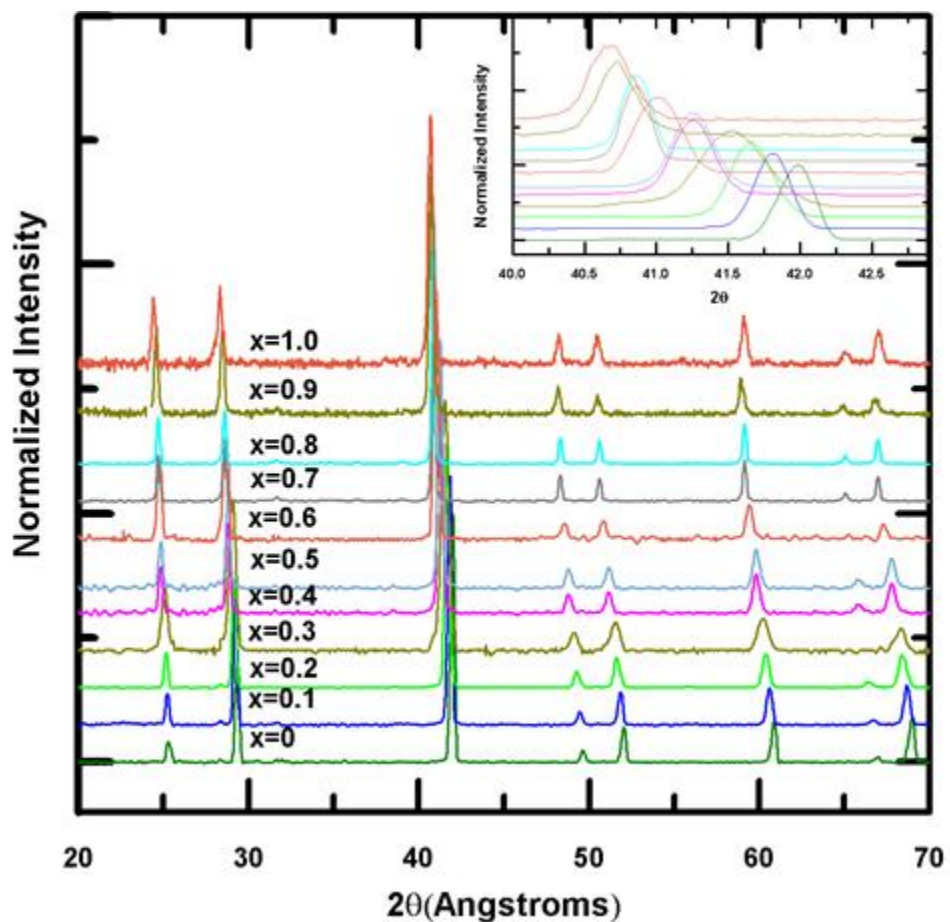
Figure: 5-15. XRD pattern of $Zr_{0.5}Hf_{0.5}Ni_{1-x}Pd_xSn_{0.99}Sb_{0.01}$ phase using PanAnalytic Xpert Pro diffractometer using Cu K_α radiation. The inset graph shows the enlarged section of the main half Heusler peaks.
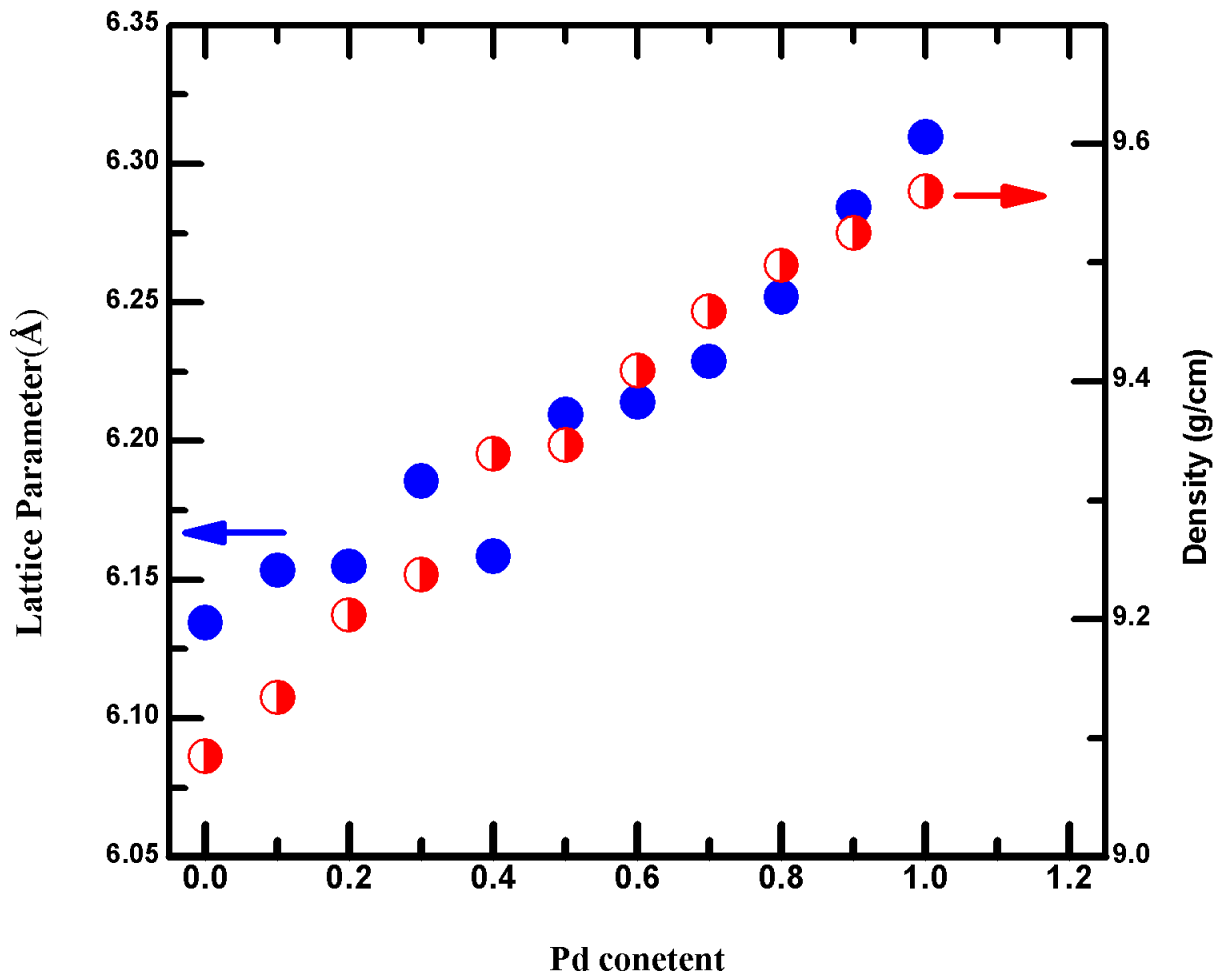
Figure:5-16 Vegard's law shows the effect of substitution of Pd on the lattice parameter and density of $Zr_{0.5}Hf_{0.5}Ni_{1-x}Pd_xSn_{0.99}Sb_{0.01}$

Theorectical density was calculated from PXRD data. In this chapter we will proceed with data analysis and discuss the experimental results.

5.2. High Temperature Thermoelectric Properties of $Zr_{0.5}Hf_{0.5}Ni_{1-x}Pd_xSn_{0.99}Sb_{0.01}$

After the hot pressing the samples, small piece from cut part of the samples were finally grounded to perform PXRD. Detailed analysis of X-ray diffraction data, Fig 5.1 does not reveal reflection of any spurious phases in the samples. All bulk materials have single phase and diffraction peaks correspond to cubic MgAgAs type crystal structure. Identical pattern of diffraction peaks of $Zr_{0.5}Hf_{0.5}Ni_{1-x}Pd_xSn_{0.99}Sb_{0.01}$ indicate that addition of Pd does not change the crystal structure. The peaks position move towards smaller angle with increasing concentration of Pd, as shown in the inset plot Fig .5.1. With the exception of sample containing 40% Pd the lattice parameter increases by increasing Pd content because the atomic radius of Pd(137pm) is bigger than that of Ni (124pm) which will decrease the lattice volume. Consequently the density of $Zr_{0.5}Hf_{0.5}Ni_{1-x}Pd_xSn_{0.99}Sb_{0.01}$ phase increases by substitution Pd at Ni site Fig 5.2.It is noted sample with x=0.4 deviates from the linearity in Vegard 's plot has lowest compaction and this has influenced the thermoelectric properties of this sample.

Figures (5-3), (5-4) and (5-5) show electrical properties are very sensitive to partial substitution of Pd. An overlay of resistivity vs-T curves of $Zr_{0.5}Hf_{0.5}Ni_{1x}Pd_xSn_{0.99}Sb_{0.01}$ alloys Fig 5-3 shows that partial substitution of Pd for the Ni site causes profound change in ρ and increases by alloying Pd at Ni site. All samples in the series exhibit metal like characteristic $(d\rho/dT>0)$. The resistivity increases with increase in temperature because the of the increased electron-electron interactions with increasing temperature and this slows down the motion of charge carriers.

111
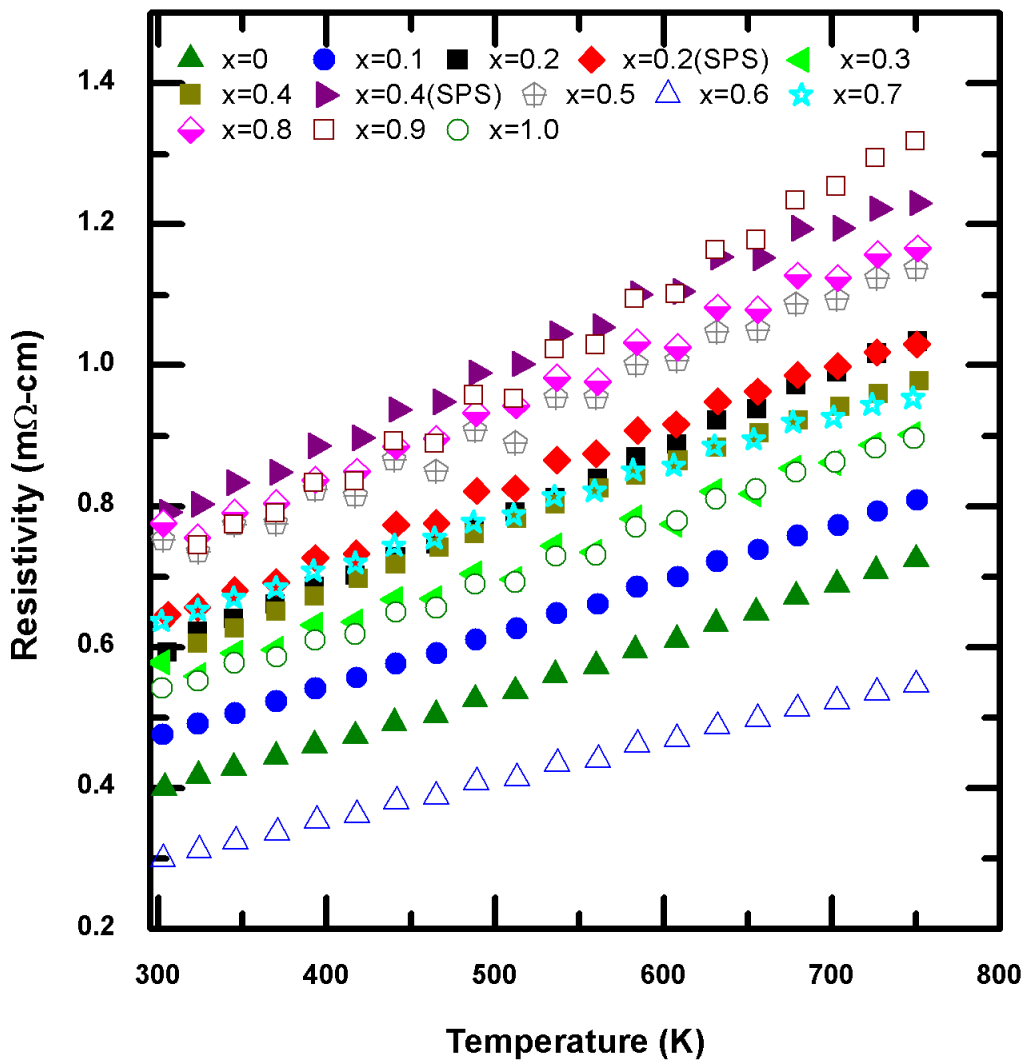
Figure:5-17 Temperature dependence of resistivity of $Zr_{0.5}Hf_{0.5}Ni_{1-x}Pd_xSn_{0.99}Sb_{0.01}$. The SPS and hot pressed samples doe not show any significant difference in resistivity.

Resistivity values are of the order of 10^{-6} Ω-m.The result of Hall measurements are shown in Table 5-1. It is noticed that hall mobility decreases with increasing Pd this results an increase in resistivity which is consistent with result shown in Fig (5-2). Resistivity values obtained from ZEM measurement (Fig. 5-1), for x= 0 and x=0.2 are reduced ~ 5% from the previously reported samples by Q. Shen [1] over the entire range of measurement. The resistivity of $Zr_{0.5}Hf_{0.5}NiSn_{0.99}Sb_{0.01}$ is 3.9×10^{-4} (Ω -cm) at room temperature and is decreased ~95% in comparison to $Zr_{0.5}Hf_{0.5}NiSn$ $8.3 \times 10^{-3}\Omega$-cm [2]. Furthermore, the resistivity of $Zr_{0.5}Hf_{0.5}Ni_{0.6}Pd_{0.4}Sn_{0.99}Sb_{0.01}$ SPS pressed sample with compaction of 8.872 g/cm^3 , slightly higher than hot pressed sample with had a compacted density of 8.59 g/cm^3. Also we noticed that the powder density of this sample Fig (5-2) is lowest in the series so there must be compositional disorder produced during synthesis. The band gap energy E_g of all the solid compounds was estimated from the linear slope of ln(ρ) vs 1/T curve using the relation:

$$\rho \sim e^{E_g/k_B}$$ (5-1)

where E_g is the effective band gap and k_B is the Boltzmann constant. This simple relationship is most useful for estimating the band gap of nondegenerate semiconductors, so here we refer to an effective band gap or activation energy. Addition of Pd does not significantly change this band gap energy as shown in Table 5-1. The temperature dependence of Seebeck coefficient Fig 5-4 and Hall Measurements Table 5-1 show that all compounds in $Zr_{0.5}Hf_{0.5}Ni_{1-x}Pd_xSn_{0.99}Sb_{0.01}$ series are n-type thermoelectric materials. The absolute value of S increases with temperature for all samples indication of degenerate behavior in these materials. There is not much difference in Seebeck coefficient of SPS and hot pressed samples for $Zr_{0.5}Hf_{0.5}Ni_{0.8}Pd_{0.2}Sn_{0.99}Sb_{0.01}$ but in $Zr_{0.5}Hf_{0.5}Ni_{0.6}Pd_{0.4}Sn_{0.99}Sb_{0.01}$ the hot press sample has higher Seebeck coefficient as compared
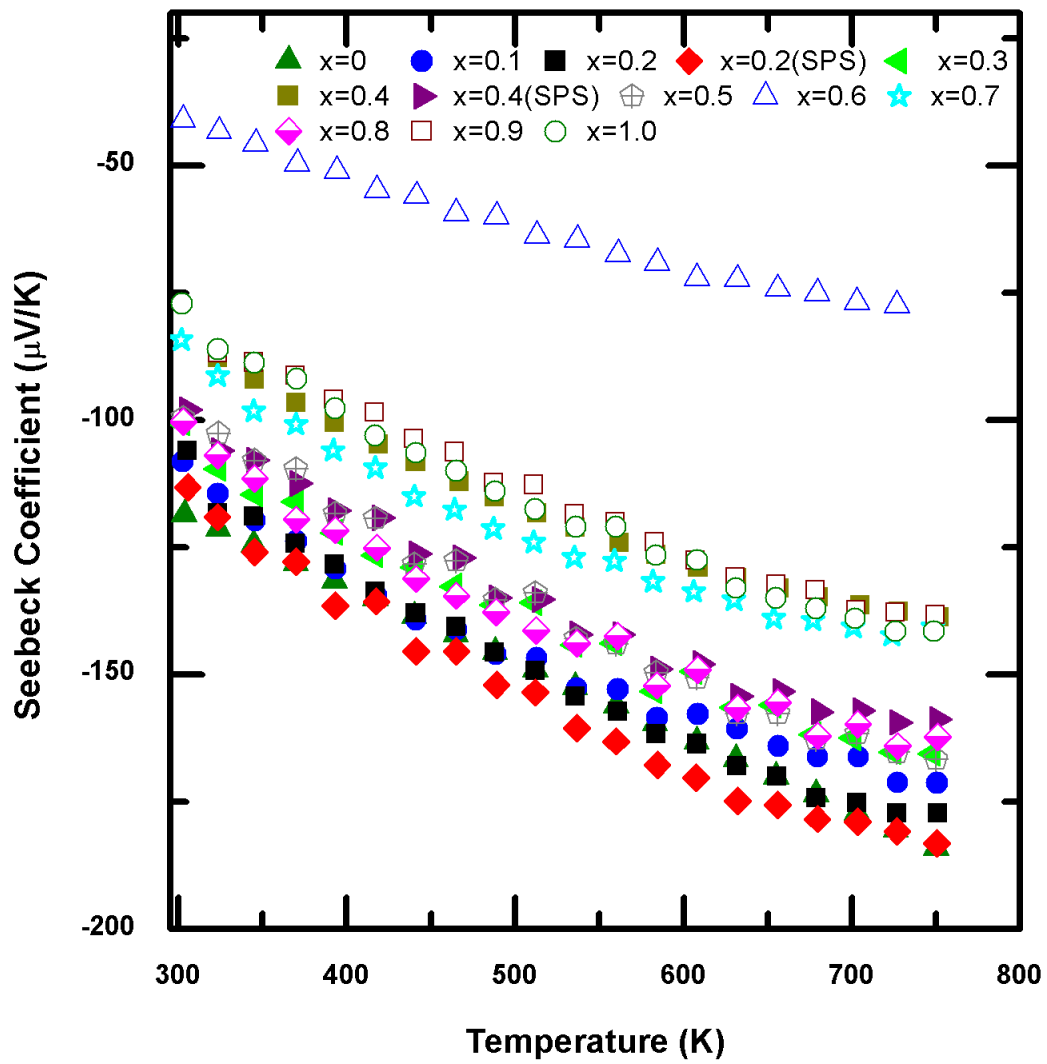
Figure:5-18 Temperature dependent Seebeck Coefficient

to SPS press sample with same composition The Seebeck coefficient decreases by isolectronic alloying of Pd at Ni site beyond x=0.2 and prominent decrease in the absolute value of Seebeck coefficient for Pd=0.6 is noticed. At present, we are working to understand this anomalous behavior.

The room temperature Seebeck coefficient is -118μV/K and reaches to -184μV/K at 750 K for $Zr_{0.5}Hf_{0.5}NiSn_{0.99}Sb_{0.01}$. These values are 10% higher than previously reported by Q Shen [1]. Effective mass m_{eff} is another important variable that has great impact on electrical properties of the carrier. Using a simple parabolic band model, and considering the acoustic phonon scattering to be dominant, from equations (5.1) and (5.2) [3] effective mass m_{eff} was estimated from the experimental values of Seebeck coefficient and carrier concentration n data obtained from Hall measurement. The plot for Seebeck dependence on reduced Fermi energy ($\eta = \frac{E_B}{k_B T}$.) is given in Appendix C. The following equations are used to find effective mass.

$$S = \frac{k_B}{e}\left[\eta_F - \frac{2F_1(\eta_F)}{F_0(\eta_F)}\right] \tag{5-1}$$

$$n = 4\pi\left[\frac{2mk_BT}{h^2}\right]^{3/2} F_{1/2} \tag{5-2}$$

where η_F is the reduced Fermi energy, a Fermi integral of order x. Fermi Integral is solved using the degenerate limit.[[3] K_b is Boltzmann constant and h is Plank's constant. The effective mass varies from $2.2m_e$. to $6.7m_e$ as shown in Table 5-1. Large effective mass renders the carriers to be less mobile. For most of the $Zr_{0.5}Hf_{0.5}Ni_{1-x}Pd_xSn_{0.99}Sb_{0.01}$ compositions moderate values of motilities are obtained. The composition $Zr_{0.5}Hf_{0.5}Ni_{0.99x}Pd_{x0.01}Sn_{0.99}Sb_{0.01}$ has highest mobility.

The temperature dependence of power factor (S/ρ^2) of $Zr_{0.5}Hf_{0.5}Ni_{1-x}Pd_xSn_{0.99}Sb_{0.01}$ is shown in Fig. 5-5. Large values of power factor are observed for sample with no Pd sample over the investigated temperature range. Power factor of this sample is $34.7\mu W/cm$-K^2 at 300K and

Table 5-4. Room temperature values of the transport parameters and result of Hall Effect measurement of $Zr_{0.5}Hf_{0.5}Ni_{1-x}Pd_xSn_{0.99}Sb_{0.01}$. Unit cell density is calculated from PXRD data and m_e is the mass of electron.

Composition	Unit Cell Density (g/cc)	Electrical Resistivity (mΩ-cm)	Seebeck Coefficient (μV/K)	Energy Gap eV	Effective mass (m_{eff})	Hall Coefficient (RH) (m^3/C)10^{-8}	Hall Carrier Concentration (m^{-3})10^{26}	Hall Mobility (cm^2/Vs)
$Zr_{0.5}Hf_{0.5}NiSn_{0.99}Sb_{0.01}$	9.196	0.475	-117.90	.079	$4m_e$	-1.27	-4.89	26.90
$Zr_{0.5}Hf_{0.5}Ni_{0.99}Pd_{0.01}Sn_{0.99}Sb_{0.01}$	9.241	0.799	-107.92	.069	$2.7\,m_e$	-1.99	-3.13	38.9
$Zr_{0.5}Hf_{0.5}Ni_{0.8}Pd_{0.2}Sn_{0.99}Sb_{0.01}$	9.244	.550	-108.99	.074	$3.2m_e$	-1.73	-3.59	31.5
$Zr_{0.5}Hf_{0.5}Ni_{0.7}Pd_{0.3}Sn_{0.99}Sb_{0.01}$	9.316	0.705	-106.41	.064	$2.2m_e$	-2.07	-2.52	29.4
$Zr_{0.5}Hf_{0.5}Ni_{0.6}Pd_{0.4}Sn_{0.99}Sb_{0.01}$	9.253	0.787	-82.68	.056	$2.4m_e$	-1.44	-4.33	18.3
$Zr_{0.5}Hf_{0.5}Ni_{0.5}Pd_{0.5}Sn_{0.99}Sb_{0.01}$	9.372	0.864	-98.60	.060	$3m_e$	-1.35	-4.61	15.57
$Zr_{0.5}Hf_{0.5}Ni_{0.4}Pd_{0.6}Sn_{0.99}Sb_{0.01}$	9.382	0.296	-26.15	.072	------	-.269	-23.2	9.07
$Zr_{0.5}Hf_{0.5}Ni_{0.3}Pd_{0.7}Sn_{0.99}Sb_{0.01}$	9.417	0.661	-87.22	.050	$3.62\,m_e$	-.867	-7.01	13.1
$Zr_{0.5}Hf_{0.5}Ni_{0.2}Pd_{0.8}Sn_{0.99}Sb_{0.01}$	9.491	1.568	-100.85	.056	$2.60\,m_e$	-1.89	-3.30	16.3
$Zr_{0.5}Hf_{0.5}Ni_{0.1}Pd_{0.9}Sn_{0.99}Sb_{0.01}$	9.546	0.498	-83.29	.077	$6.7m_e$	-0.31	-20.2	6.15
$Zr_{0.5}Hf_{0.5}PdSn_{0.99}Sb_{0.01}$	9.605	1.395	-80.45	.066	$2.3m_e$	-1.43	-4.35	10.30
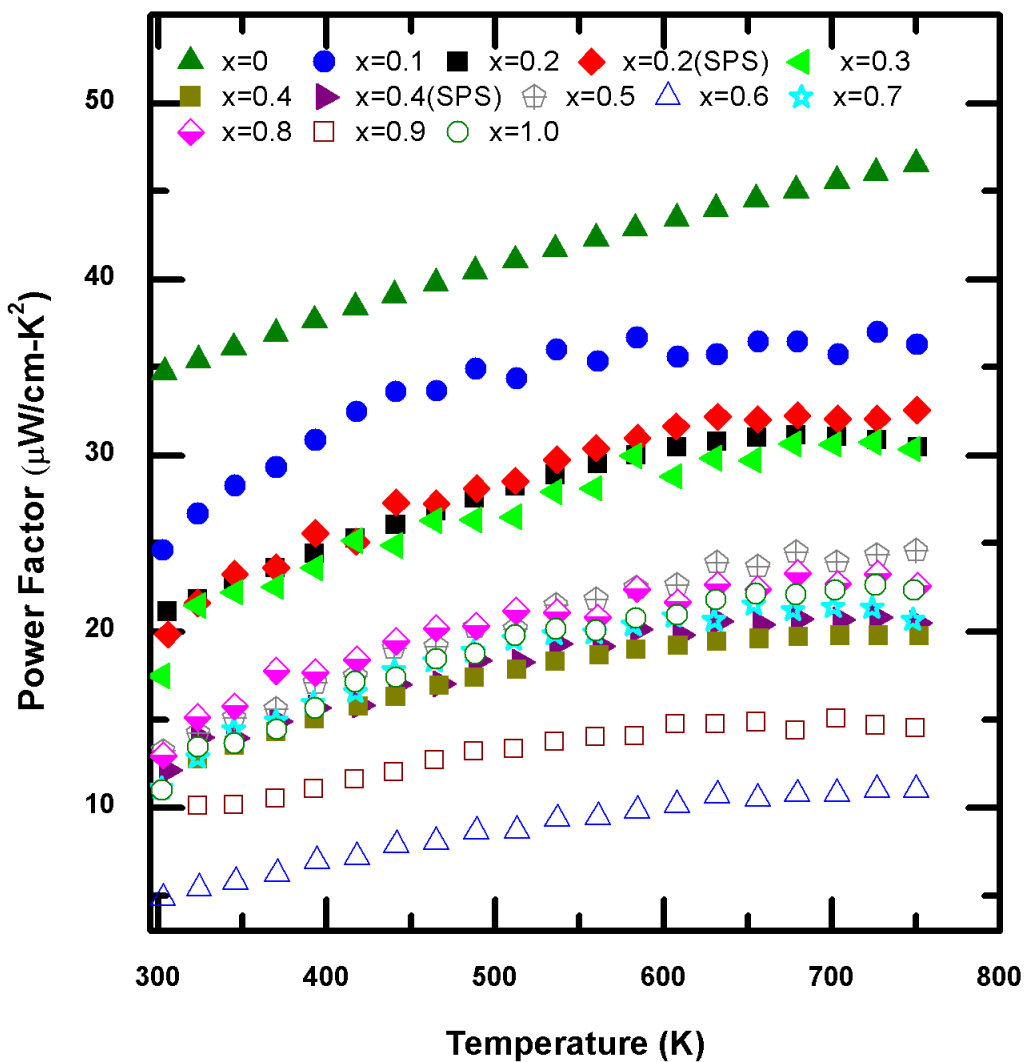
Figure:5-19 Temperature dependence of Power factor in $Zr_{0.5}Hf_{0.5}Ni_{1-x}Pd_xSn_{0.99}Sb_{0.01}$. No enhancement in power factor is noticed by isoelectronic alloying at Ni with Pd.

reaches a maximum value of 46.5μW/cm-K^2 at 750K whereas Q Shen [1] [reported the value of 34μW/cm-K^2 for this sample composition, synthesized by arc-melting. This is an increase in power factor of 27%.results is due to reduction in resistivity. S/ρ^2 values are identical for composition with 70% and 100 % Pd content. Despite the lowest resistivity the sample with 60% Pd content has lowest Seebeck coefficient and this composition has lower power factor in $Zr_{0.5}Hf_{0.5}Ni_{.1-x}Pd_xSn_{0.99}Sb_{0.01}$. It is inferred from Fig. 5-5 power factor decreases by isoelectronic alloying at Ni site and Pd substitution above x$\geq$0.3 is not very effective for improving electrical performance of $Zr_{0.5}Hf_{0.5}Ni_{1-x}Pd_xSn_{0.99}Sb_{0.01}$.

The thermal conductivity is another key parameter in determining the usefulness of thermoelectric materials. Figure 5-6 shows the temperature dependent thermal conductivity increases with increasing temperature but reduces substantially with increasing Pd content and goes up for 60% Pd content and then falls off. There is no answer for this anomalous rise in the thermal conductivity. Although the resistivity data shows this sample has higher electrical conductivity. The minimum value of thermal conductivity is obtained for sample with 50% Pd content 3.9 W/m-K at 750K which is relatively higher than previously reported by Q Shen [1] 2.1 W/m-K for similar composition. The only reasons for higher value of thermal conductivity from Q Shen data are difference is compactness factor and grain size. It is noted that the hot pressed sample $Zr_{0.5}Hf_{0.5}Ni_{0.8}Pd_{0.2}Sn_{0.99}Sb_{0.01}$ has lower resistivity than corresponding sample pressed by SPS. The sample with no Pd has the largest thermal conductivity of 7.89 (W/m-K) at room temperature and reduces to ~ 5W/m-K at 750 K. The thermal conductivity is typically described as the sum of electronic and lattice contribution. The Wiedmann-Franz law permits an estimation of the electronic component κ_e of the thermal conductivity. κ_e is frequently estimated using the metallic limit of the Lorentz number, 2.45$\times$10^5 WΩ K^{-2}; this is also commonly used

118

for degenerate semiconductors. Lattice thermal conductivity of all samples is obtained by subtraction of electronic contribution from the total thermal conductivity by using $\kappa_{t=}\ \kappa_e + \kappa_{lattice}$. The electronic thermal conductivity of $Zr_{0.5}Hf_{0.5}Ni_{1-x}Pd_xSn_{0.99}Sb_{0.01}$ alloys is not large. The calculated value of κ_e is almost 20% of the total thermal conductivity κ_t. This suggests that the main contribution to the total thermal conductivity is due to phonon part i.e. lattice component ($\kappa_{lattice}$). Thus Figure 5-8 suggests that the dominant intrinsic scattering mechanism is high temperature U-process scattering of phonons. The Pd substitution substantially decreases the lattice thermal conductivity at 300K. The lattice thermal conductivity decreases monotonically from x= 0 to x= 0.5 above 300K This explains that the high temperature lattice thermal conductivity is sensitive to the point-defect scattering. Isoelectronic substitution does not introduce charge disorder in the crystal lattice but creates point defect scattering for phonons due to mass fluctuation, size and strain fluctuation. The strain field scattering arises due to difference in size and inter-atomic coupling forces between the doping and host atoms. Meisner reported substitution of Pd at Ni sites causes strain filed fluctuations, and it is this effect which leads to reduction in lattice thermal conductivity by alloying at Ni site [4]. The lattice thermal conductivity reduces to 30.5% for un-substituted half Heusler to 40% substituted with Pd at Ni site at room temperature. The lattice component of thermal conductivity for composition $Zr_{0.5}Hf_{0.5}Ni_{0.6}Pd_{0.4}Sn_{0.99}Sb_{0.01}$ does not change much beyond 650K. In addition the lattice thermal conductivity of compositions $Zr_{0.5}Hf_{0.5}Ni_{0.2}Pd_{0.8}Sn_{0.99}Sb_{0.01}$ and $Zr_{0.5}Hf_{0.5}PdSn_{0.99}Sb_{0.01}$ lie on top of each other over the entire temperature range whereas they have difference in electrical conductivity.
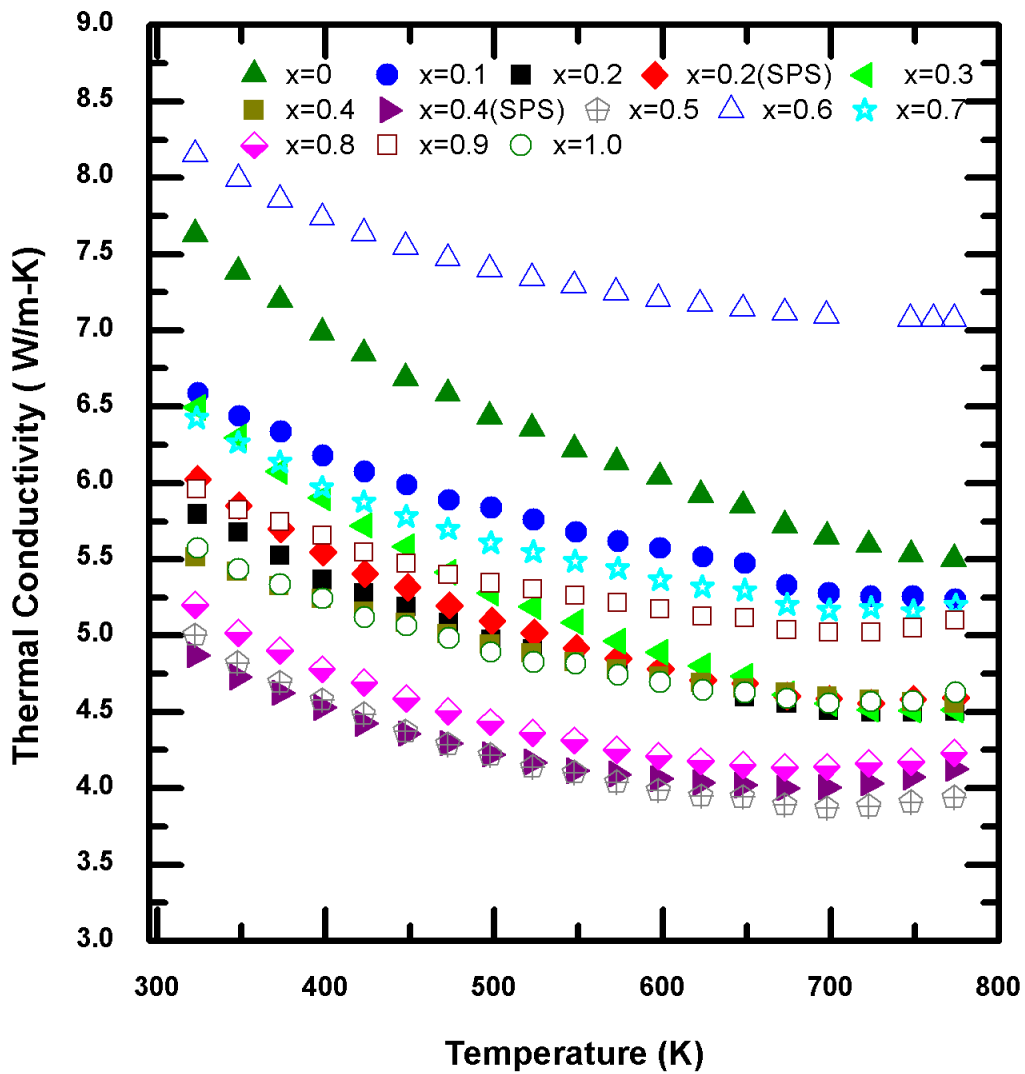
Figure:5-20 The total thermal conductivity ($\kappa_t = \kappa_l + \kappa_e$, where κ is contribution due to lattice vibration and electronic component of thermal conductivity) decreases with increasing temperature in $Zr_{0.5}Hf_{0.5}Ni_{1-x}Pd_xSn_{0.99}Sb_{0.01}$
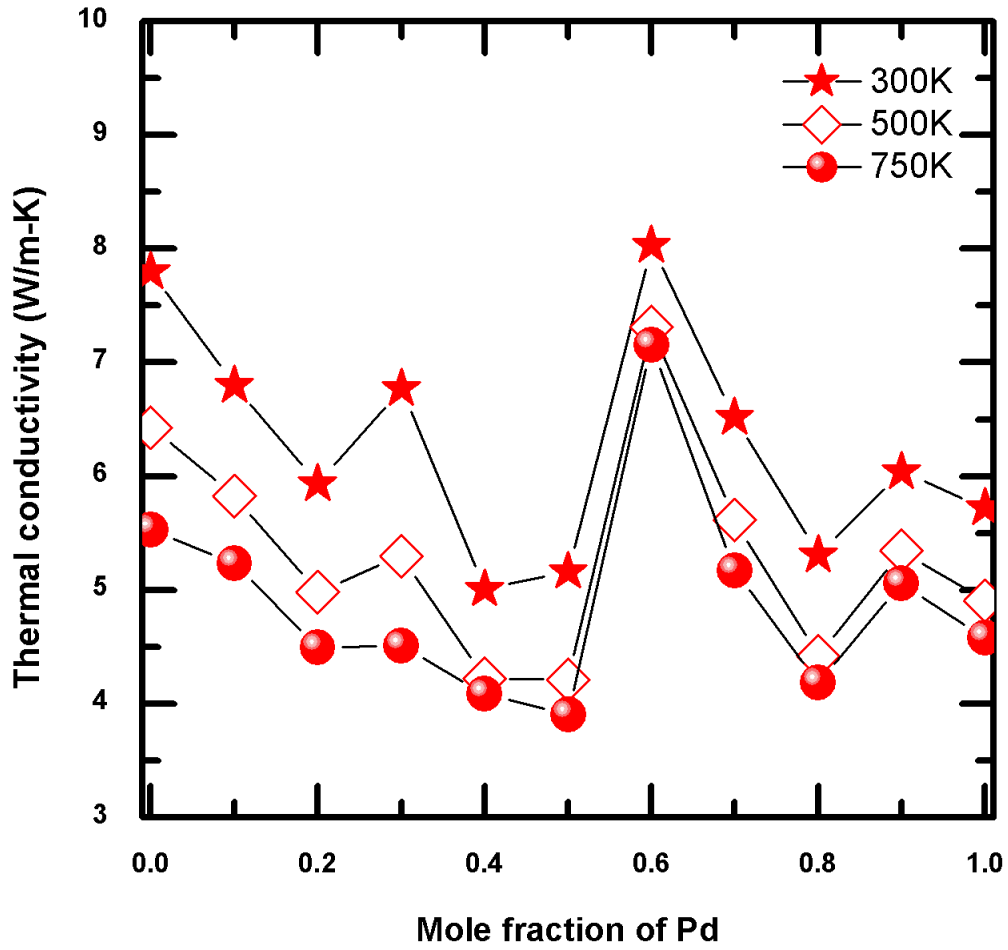
Figure:5-21 Total thermal conductivity of $Zr_{0.5}Hf_{0.5}Ni_{1-x}Pd_xSn_{0.99}Sb_{0.01}$ at 300 K, 500 K and 750 K as a function of Pd content.
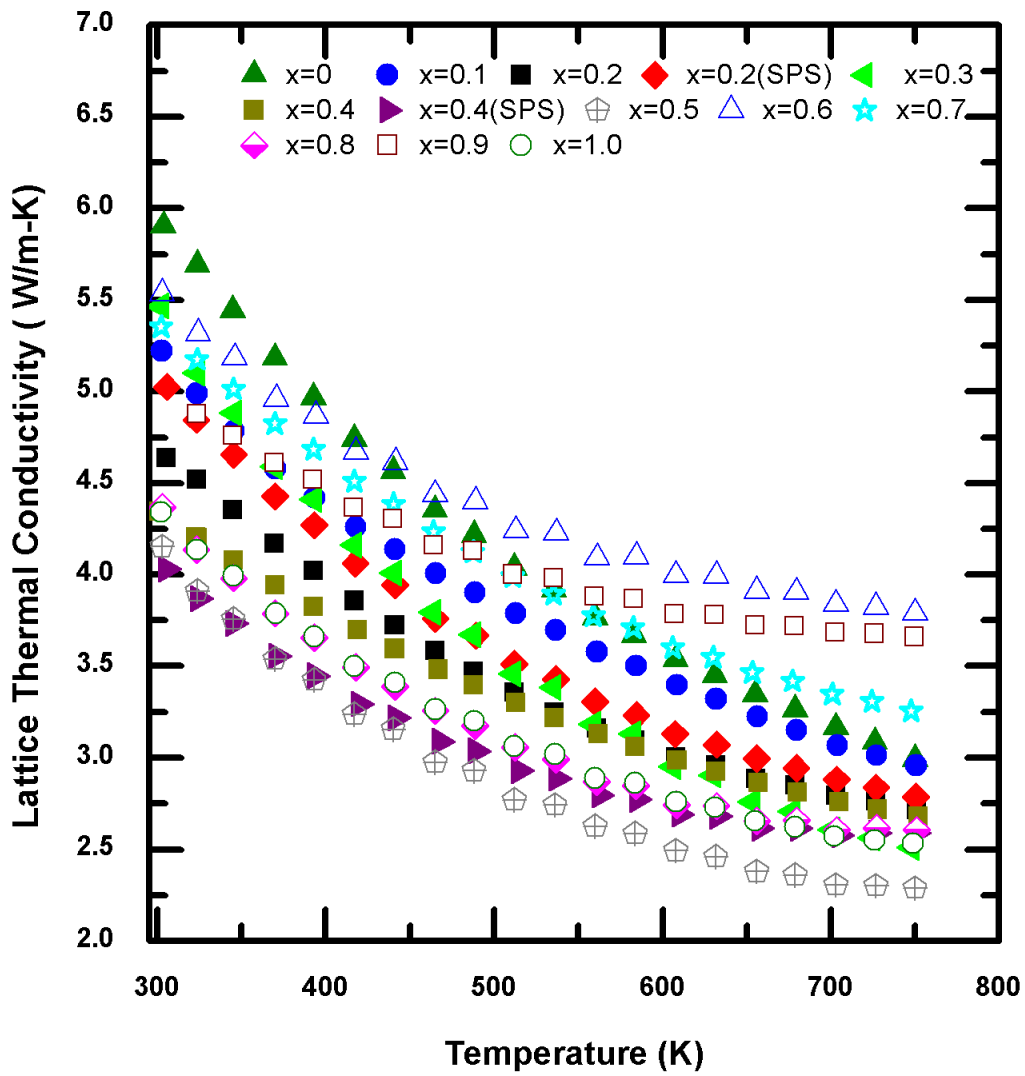
Figure:5-22 Substitution of Pd decreases lattice thermal conductivity in $Zr_{0.5}Hf_{0.5}Ni_{1-x}Pd_xSn_{0.99}Sb_{0.01}$ until x=0.5
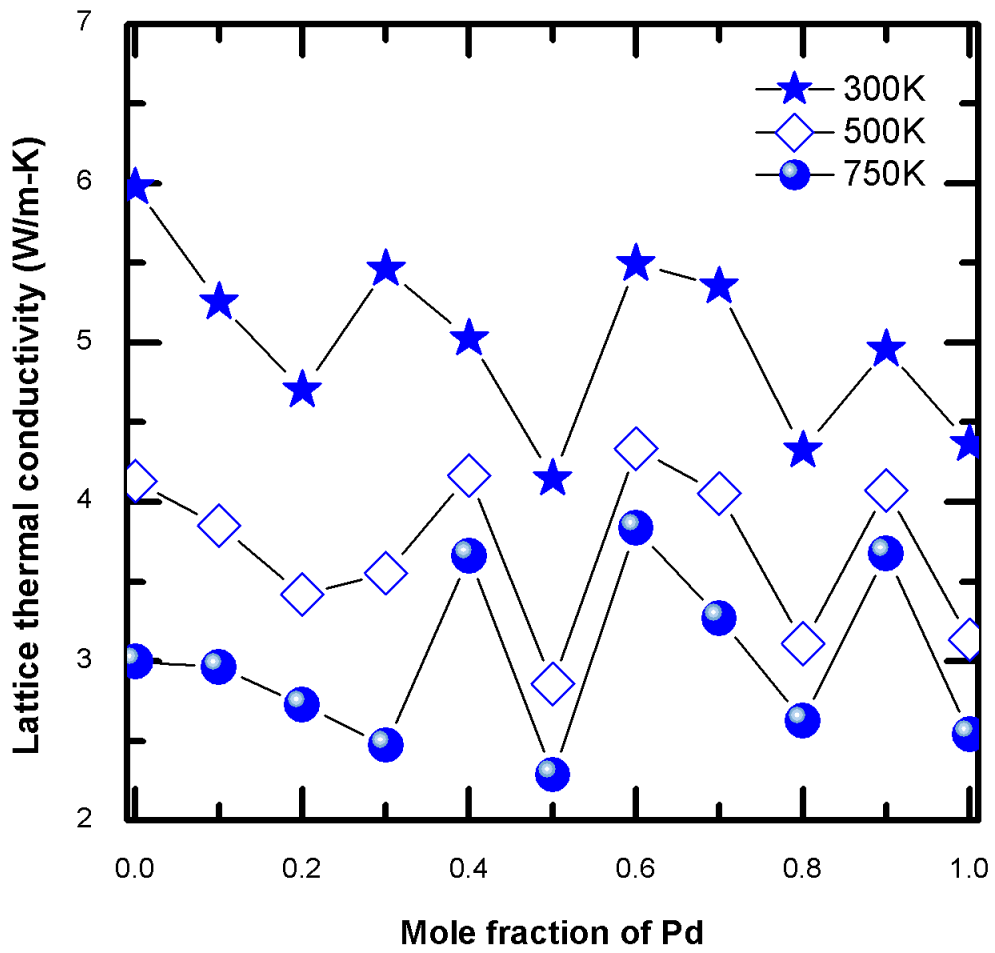
Figure:5-23 Lattice thermal conductivity of at 300 K, 500 K and 750 K as a function of Pd content
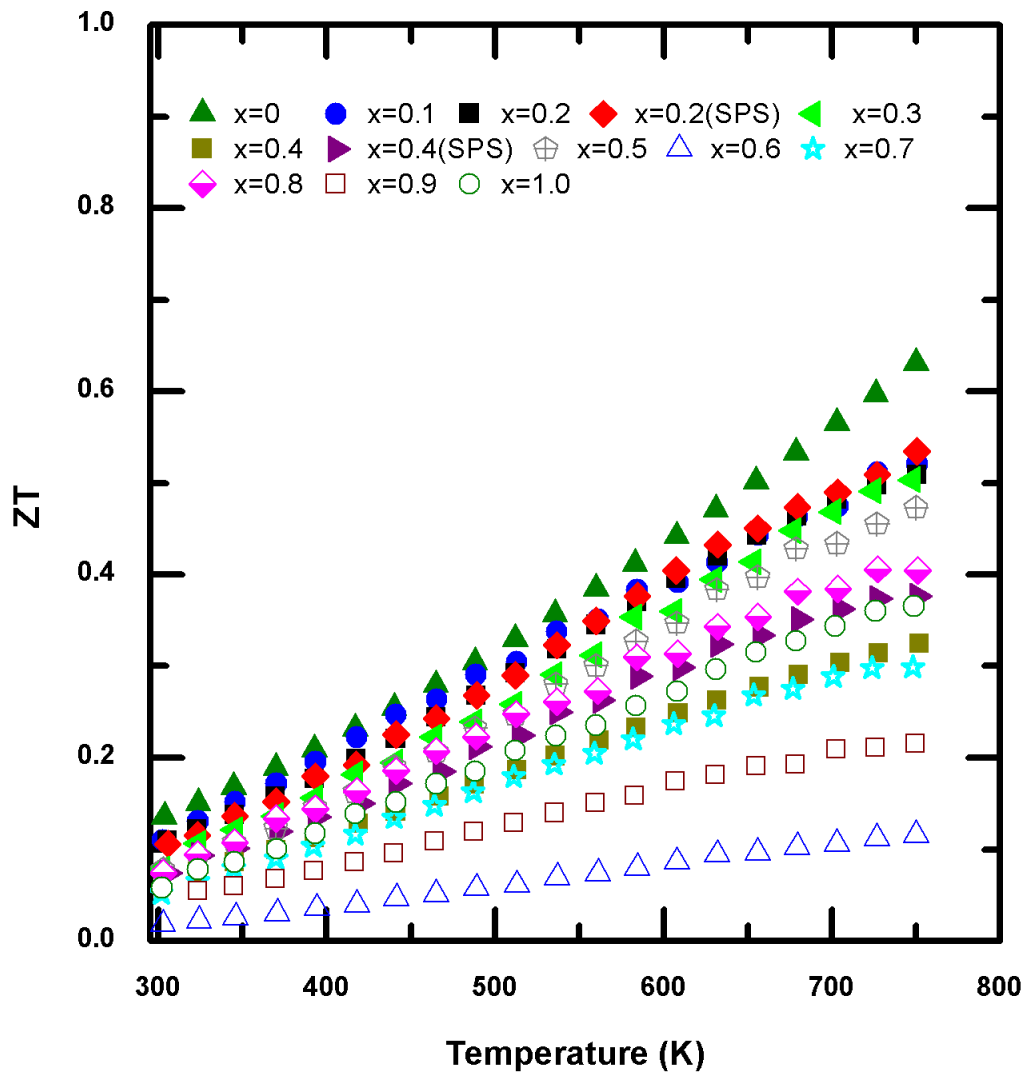
Figure:5-24 Temperature dependence of figure of merit ZT of $Zr_{0.5}Hf_{0.5}Ni_{1-x}Pd_xSn_{0.99}Sb_{0.01}$
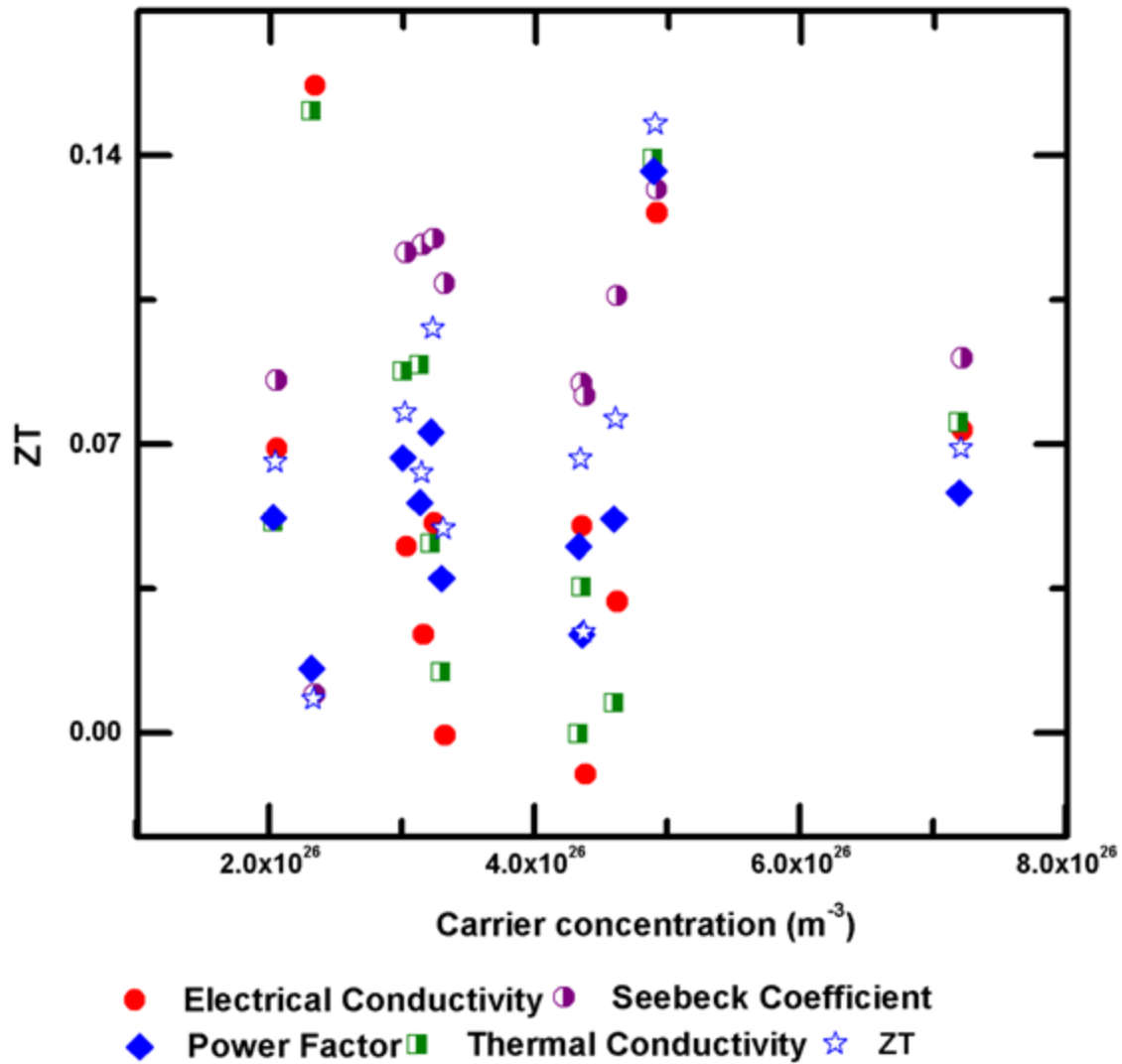
Figure:5-25 **Variation of thermoelectric properties and ZT at 300K of $Zr_{0.5}Hf_{0.5}Ni_{1-x}Pd_xSn_{0.99}Sb_{0.01}$ as function of carrier concentration measured by Hall apparatus.**

ZT is estimated by $T = \frac{S^2\sigma}{\kappa}$. Figure 5.10 shows the best ZT~0.63 at 750K is obtained for $Zr_{0.5}Hf_{0.5}NiSn_{0.99}Sb_{0.01}$. This value is higher than 0.56 at 750 K previously reported [1]. The ZT of compositions x=0, 0.1.0.2 and 0.3 lie very close at high temperature i.e. 0.5 to 0.53 at 750 K. Although thermal conductivity decreases with increasing Pd content $0 \leq x \leq 0.5$, the ZT decreases because the power factor also falls off with increasing Pd concentration. But after $0 \leq x \leq 0.5$ thermal conductivity goes up without following any trend. For all the samples ZT increases with temperature and shows no sign of saturation. Further improvement in ZT can be expected by achieve by decreasing the grain size which comes from reduction in thermal conductivity without bringing any change in electric properties.

Result of thermoelectric properties of series of $Zr_{0.5}Hf_{0.5}Ni_{1-x}Pd_xSn_{0.99}Sb_{0.01}$ samples give a clear picture that thermoelectric properties varies greatly with substitution of Pd at Ni site but no net enhancement in the figure of merit, ZT is noticed.

All the compounds in $Zr_{0.5}Hf_{0.5}Ni_{1-x}Pd_xSn_{0.99}Sb_{0.01}$ are n-type semiconductor with Seebeck coefficient ranging from -41to-184µV/K at room temperature. Moreover Figure 5.11 shows that improvement in power factor, electrical conductivity and ZT is obtained at carrier concentration $4.89 \times 10^{26} m^{-3}$.

5.3 Role of NiO nanoinclusions

In this part we will discuss the effect of introducing NiO nanoinclusions on the thermal and electrical transport properties of $Zr_{0.5}Hf_{0.5}$. $Ni_{1-x}Pd_xSn_{0.99}Sb_{0.01}$ (x=0 and 0.2). The half Heusler matrix materials were prepared by solid state reaction and is combined with NiO nanoparticles separately synthesized by wet-chemical methods[6] After consolidation by hot-pressing it was found that the NiO reacted with the matrix materials for form a composite

consisting of half-Heusler and full Heusler constituents. Thermal and electrical transport measurements show an increase in electrical conductivity and decrease in Seebeck coefficient for the composites relative to their controlled matrix (no nanoparticles). Lattice thermal conductivity was also found to increase with the addition of NiO nanoparticles. The thermal and electrical properties of the hot-pressed matrix compounds are found to be consistent with, or in some cases exceed, the values for similar compounds synthesized by arc-melting or spark-plasma sintering.

The synthesized $Zr_{0.5}Hf_{0.5}Ni_{1-x}Pd_xSn_{0.99}Sb_{0.01}$ powders were mixed with 3 -6% (vol) NiO nanoparticles. The resulting powders were homogenized by ball milling (BM) for 20 minutes or dry mixing (DM) using a conventional mortar and pestle. Densification of the composite was accomplished by pressing for uniaxial vacuum hot press described in section (4.3). The sample are labeled as Pd=0 if the host matrix is $Zr_{0.5}Hf_{0.5}NiSn_{0.99}Sb_{0.01}$ and Pd=0.2 for $Zr_{0.5}Hf_{0.5}Ni_{0.8}Pd_{0.2}Sn_{0.99}Sb_{0.01}$. The sample is also labeled according to the concentration of NiO nanoparticles, for example Pd=0.2/6%NiO DM indicates $Zr_{0.5}Hf_{0.5}Ni_{0.8}Pd_{0.2}Sn_{0.99}Sb_{0.01}$ with 6% (vol) NiO nanoparticles homogenized by ball milling.

The powder x-ray diffraction profiles of hot pressed of the six different compositions are shown in Fig.5.12. The solid solution of $Zr_{0.5}Hf_{0.5}Ni_{1-x}Pd_xSn_{0.99}Sb_{0.01}$ crystallizes with MgAgAs crystal structure; the indices of the major peaks are given in the figure. While the XRD pattern of matrix material (no NiO) exhibits a single phase, impurities and composition deviations are observed after addition of NiO nanoparticles Fig5.1 2. Small peaks (indicated by arrows in Fig. 2) are identified at as the full-Heusler phase, $Zr_{0.5}Hf_{0.5}(Ni_{1-x}Pd_x)_2 Sn$. Additional impurity peaks indicated in Fig.(2) by an asterisk (*) are consistent with both ZrO_2 and HfO_2. There is peak shift towards larger angle with increasing concentration of vol% of NiO into half Heusler matrix. The grain size measured from these XRD patterns using the Debye-Scherrer method is 18-25 nm.

The theoretical density of all materials and composites is > 96% with the exception of Pd=0/6%NiOBM and Pd=0.2/6%NiO-BM, which have theoretical densities of 78% and 89%, respectively.

The temperature dependent electrical conductivity is given in Fig.5.13 which indicates semiconducting behavior for all samples (pure and composite materials). Isoelectronic alloying of 20% Pd at Ni site reduces electrical conductivity. With the introduction of NiO inclusions in the bulk half Heusler, the electrical conductivity of all samples except Pd=0/6%NiO-BM becomes drastically higher and monotonically increases with increasing concentration of NiO. For example, the room temperature electrical conductivity of the Pd=0.2 compound increases by at least a factor of 2 from 1.5 $(\mu\Omega\text{-cm})^{-1}$ to 3.0-3.5 $(\mu\Omega\text{-cm})^{-1}$ with the incorporation of 6% (vol) NiO, with a slight dependence on the method used to mix the two constituents. The room temperature value of same half Heusler composition (Pd=0.2) containing 3% (vol) NiO and 6% (vol) NiO increases 49% and 97% respectively. The low electrical conductivity of Pd=0/6%NiO-BM is attributed to the high porosity of this composite. Figure 5.14 shows the effect on the Seebeck coefficient of adding NiO nanoparticles into half Heusler alloys. All compounds and composites are n-type (electrons as the majority carrier). Although the substitution of 20% Pd for Ni results in a ~50% reduction in electrical conductivity, the Seebeck coefficient is not affected by this alloying. All the samples containing NiO show decrease in the absolute value of Seebeck coefficient relative to the samples without inclusions. This is consistent with the observation of increased electrical conductivity and is due to the reaction of NiO with the half-Heusler to form a metallic, full-Heusler phase. The power factor $(S^2\sigma)$ is plotted in Fig. 5.15. The power factor for all of the composites except Pd=0.2/3%-NiO-BM is lower than that of the pure matrix compound $Zr_{0.5}Hf_{0.5}Ni_{0.8}Pd_{0.2}Sn_{0.99}Sb_{0.01}$ does show a slight improvement after the incorporation NiO

128
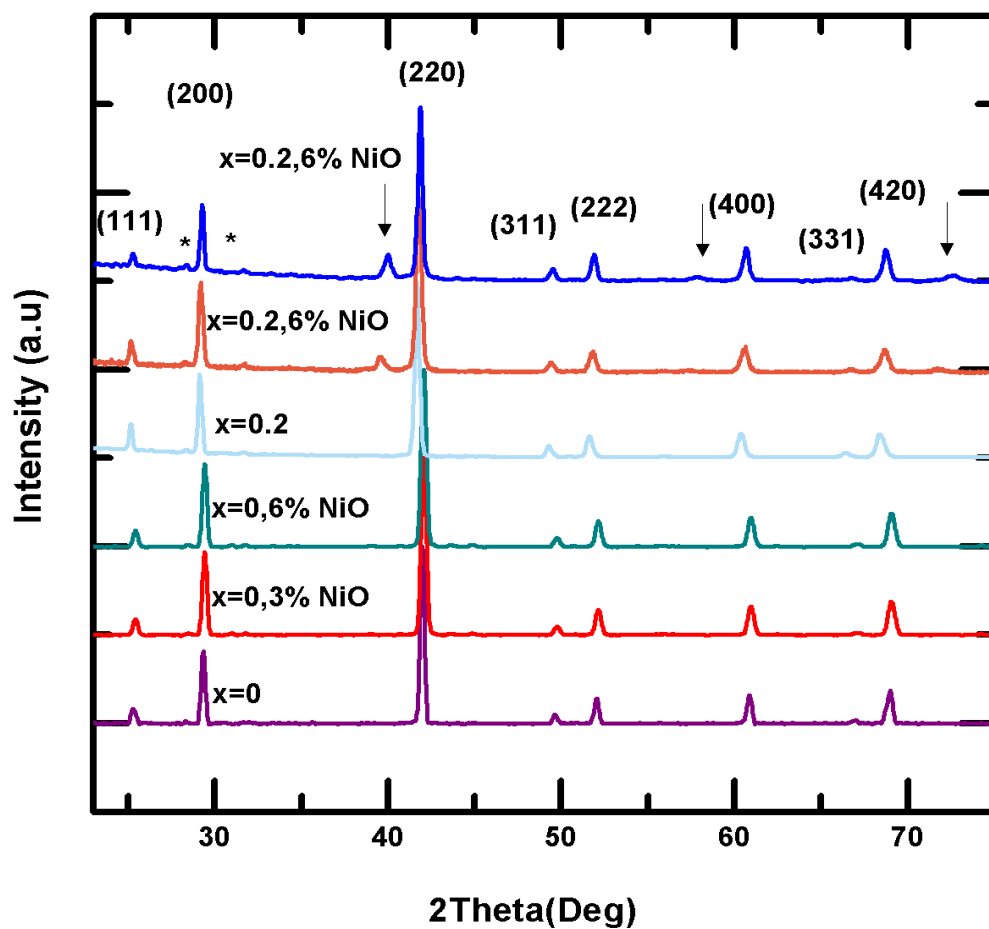
Figure:5-26 Powder X-ray diffraction (XRD) data for $Zr_{0.5}Hf_{0.5}NiSn_{0.99}Sb_{0.01}$, $Zr_{0.5}Hf_{0.5}Ni_{0.8}Pd_{0.2}Sn_{0.99}Sb_{0.01}$ and composites containing, 0, 3 and 6% (vol) NiO nanoparticles. There is peak shift with increasing NiO concentration indicating incorporation of Ni into the lattice. HfO_2 and/or ZrO_2 peaks are evident in the composite sample (labeled with an *) and no evidence of NiO nanoparticles is seen in the XRD data.

nanoinclusions. Comparison shows that the pure Ni compound ($Zr_{0.5}Hf_{0.5}NiSn_{0.99}Sb_{0.01}$) has a peak power factor 46.5µW/cm-K^2 which is 35% higher than that reported by [1] for the same composition, consolidated by spark-plasma sintering.

Thermal conductivity evaluated from thermal diffusivity and heat capacity measured from laser flash method for $Zr_{0.5}Hf_{0.5}Ni_{1-x}Pd_xSn_{0.99}Sb_{.01}$ and composites containing 3% and 6% vol of NiO nano particulates is shown in Fig 5.16. It is the lattice part of thermal conductivity that we are trying to reduce by increasing phonon scattering by addition of nanoparticles. The lattice contribution to thermal conductivity is shown in Fig. 6. The lattice thermal conductivity exhibits the conventional 1/T dependence and 6% (vol) NiO in $Zr_{0.5}Hf_{0.5}NiSn_{0.99}Sb_{.01}$ shows minimum lattice thermal conductivity in all range of temperature .The reason for low thermal conductivity for this sample is that it is highly porous (see Appendices F,G,H). In general, the composite materials have higher lattice thermal conductivity than their matrix (pure) counterparts The x-ray diffraction data show that adding NiO nanoparticles to the $Ni_{0.8}Pd_{0.2}$ based half- Heusler materials results in a partial conversion of half-Heusler to full-Heusler structure, although no such conversion can be seen in the XRD data for the pure Ni (Pd=0) based materials. While the half-Heusler compounds are semiconductors with bandgaps of 0.1-0.2 eV13, full Heusler compounds are metals. The resulting composite is then a half-Heusler matrix with metallic (full-Heusler) inclusions. A simple Debye-Scherer analysis of the peak width of the full-Heusler peaks identified in Fig 5.12 indicates of grain size of about 20 nm for the full Heusler phase. Of course, incorporation of the metallic full-Heusler phase into the half-Heusler results in an increase in electrical conductivity Fig 5.13 along with a decrease in Seebeck coefficient Fig 5.14. This is also consistent with our previous finding that the addition of NiO results in an increase in the carrier mobility[6] .Interestingly, no full-Heusler peaks are seen for pure Ni (Pd=0) composites..

130
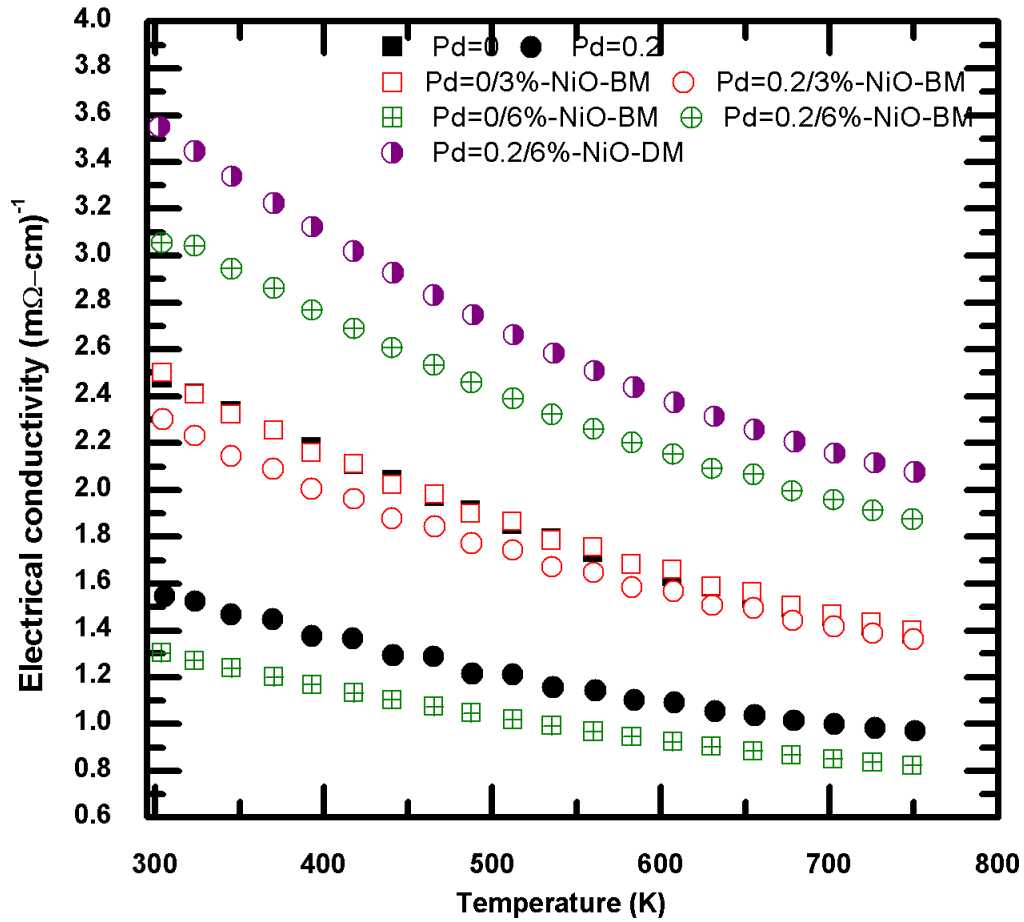
Figure:5-27Electrical Conductivity changes by adding NiO nanoinclusions into $Zr_{0.5}Hf_{0.5}NiSn_{0.99}Sb_{0.01}$ and $Zr_{0.5}Hf_{0.5}Ni_{0.8}Pd_{0.2}Sn_{0.99}Sb_{0.01}$
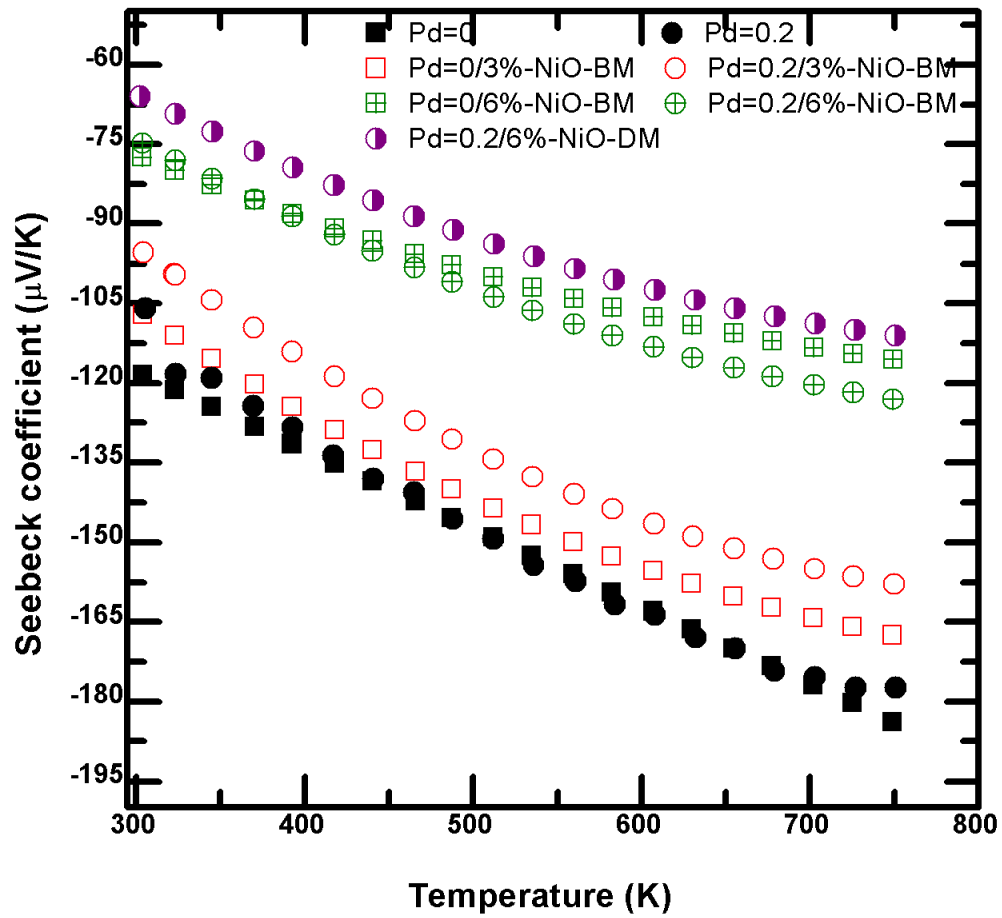
Figure:5-28 **Temperature dependent Seebeck coefficient for** $Zr_{0.5}Hf_{0.5}NiSn_{0.99}Sb_{0.01}$ **and** $Zr_{0.5}Hf_{0.5}Ni_{0.8}Pd_{0.2}Sn_{0.99}Sb_{0.01}$ **changes by increasing NiO inclusions into the controlled matrix**
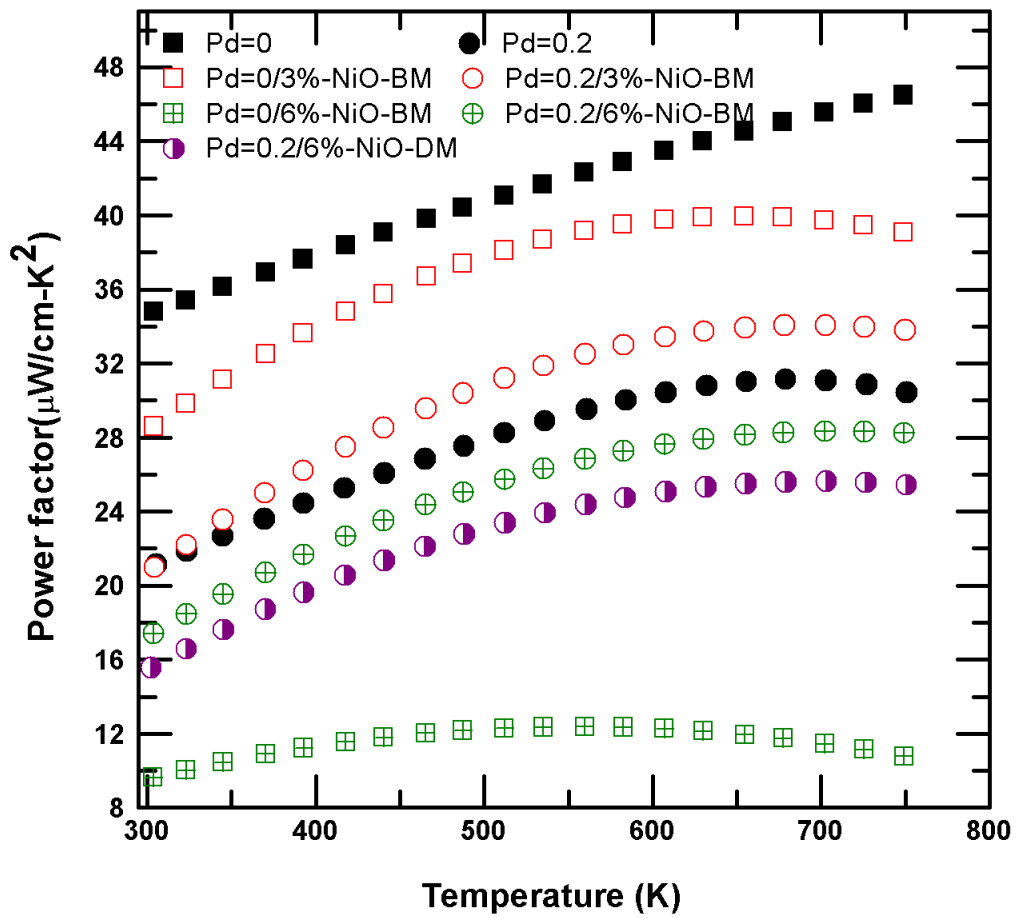
Figure:5-029 Power factor of $Zr_{0.5}Hf_{0.5}Ni_{0.8}Pd_{0.2}Sn_{0.99}Sb_{0.01}$ is increased by addition of 3% NiO
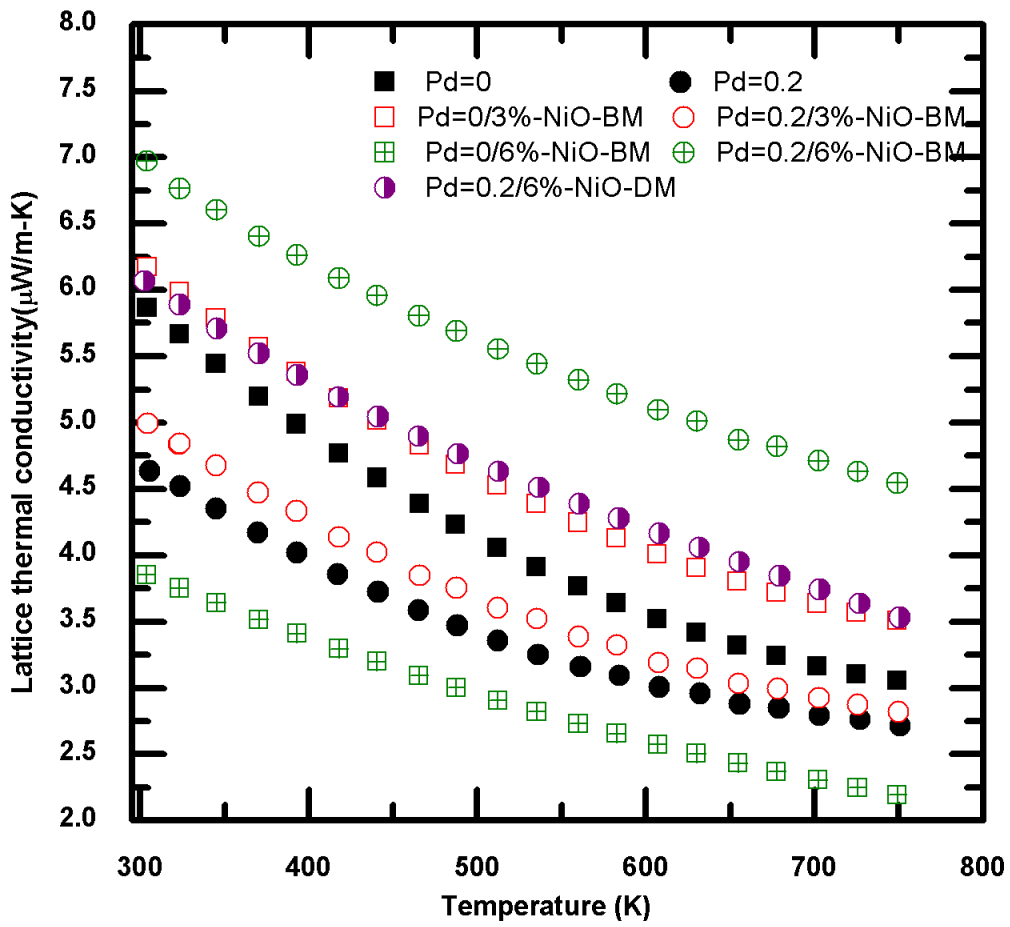
Figure:5-30 Lattice thermal conductivity for NiO-doped half Heusler $Zr_{0.5}Hf_{0.5}Ni_{1-x}Pd_xSn_{0.99}Sb_{0.01}$ with x=0 and 0.2

Table5 Room temperature Hall coefficient, resistivity, carrier concentration and mobility for the $Zr_{0.5}Hf_{0.5}Ni_{1-x}Pd_xSn_{0.99}Sb_{0.01}$ with x=0,0.2 and composites

Compounds	R_H (Web/m^2)	n ×10^{26} (m^{-3})	ρ×10^{-6} (Ω-m)	μ (cm^2/Vs)
$Zr_{0.5}Hf_{0.5}NiSn_{0.99}Sb_{0.01}$	2.67	2.39	4.21	61.8
$Zr_{0.5}Hf_{0.5}NiSn_{0.99}Sb_{0.01}$/3%-NiO	3.17	1.97	3.79	83.6
$Zr_{0.5}Hf_{0.5}NiSn_{0.99}Sb_{0.01}$/6%-NiO	1.67	3.73	7.70	21.7
$Zr_{0.5}Hf_{0.5}Ni_{0.8}Pd_{0.2}Sn_{0.99}Sb_{0.01}$	–	–	–	–
$Zr_{0.5}Hf_{0.5}Ni_{0.8}Pd_{0.2}Sn_{0.99}Sb_{0.01}$/3%-NiO	1.42	4.39	4.67	34.0
$Zr_{0.5}Hf_{0.5}Ni_{0.8}Pd_{0.2}Sn_{0.99}Sb_{0.01}$6%-NiO	1.62	3.84	3.23	54.0
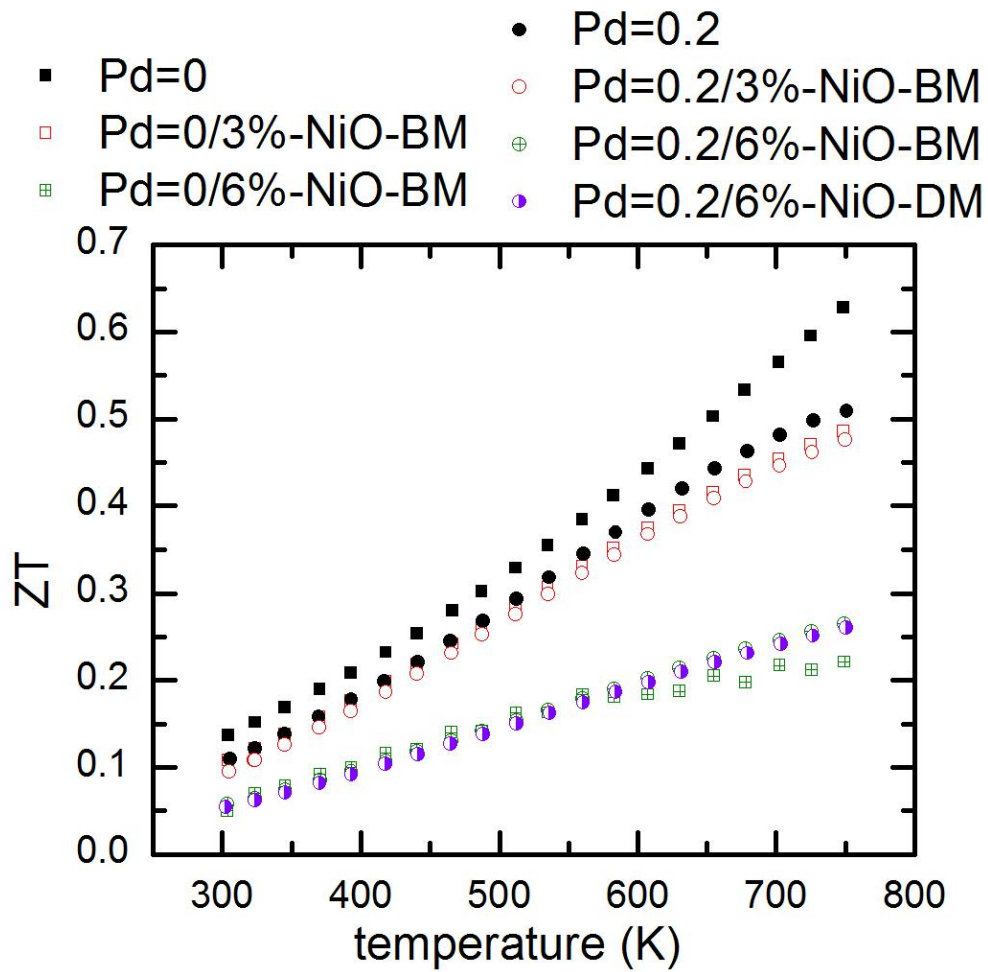
Figure:5-31 Thermoelectric figure of merit of $Zr_{0.5}Hf_{0.5}Ni_{1-x}Pd_xSn_{0.99}Sb_{0.01}$ and composites with NiO nanoparticles

In this case, the electrical conductivity did not change on the addition of NiOnanoinclusions and the Seebeck coefficient decreased by approximately 10% over the measured temperature range. In addition, the lattice thermal conductivity also increased indicating that NiO nanoparticles may be present in this composite

5.4 Effect of HfO$_2$ Nanoinclusions on the Thermoelectric Properties of Zr$_{0.5}$Hf$_{0.5}$Ni$_{1-x}$PdxSn$_{0.99}$Sb$_{0.01}$

Our goal of this project was divided into two steps first was to study the effect of Pd substitution on the electrical and thermal properties of Zr$_{0.5}$Hf$_{0.5}$Ni$_{1-x}$Pd$_x$Sn$_{0.99}$Sb$_{0.01}$ and second objective was to investigate the role of NiO and HfO$_2$ nanoparticles incorporation in half Heusler phases to impede the thermal conduction and allow electrical conduction. NiO and HfO$_2$ nano inclusions are insulating, chemically stable, and inert with regard to the half Heusler matrix As we see incorporation of NiO nanoparticles was not successful attempt to enhance thermoelectric properties so we decided to add HfO$_2$ and discontinued mechanical mixing of nanoinclusion into host in favor of dry mixing to avoid any contamination from ball milling. In this section we continue with our objective to investigate the role of 4nm sized HfO$_2$ into the bulk half Heusler matrixes in their transport properties.

We mixed HfO$_2$ prepared by method described in section (4.6), of 3%, 6% and 9% into Zr$_{0.5}$Hf$_{0.5}$Ni$_{1-x}$Pd$_x$Sn$_{0.99}$Sb$_{0.01}$ with X=0 and 0.2, in an agate mortar inside the glove box in the presence of Ar. The resulting homogenous mixture was hot pressed Sec(4.3.3).Thermal conductivity was measured on disk shaped samples and electrical conductivity and Seebeck coefficients were measured simultaneously in helium atmosphere from room temperature to

500˚C on rectangular shaped specimens. XRD and elemental analysis was performed in the SEM using EDAX.

Figure 5-18 shows the powder XRD of HfO_2, and "as-syn" indicates as it was synthesized at room .After the synthesis of HfO_2, described in section, HfO_2 nanoparticles were annealed at increasing temperature from 300˚C to 600˚C for four hours in oxygen atmosphere. Fig 5.18 indicates that all peaks correspond to monoclinic phase of HfO_2. TEM Fig shows the particle size of HfO_2 is ≈4nm. The PXRD of composites of Heusler phases with HfO_2 do not show any HfO2 peaks.Fig 5.19.There is possibility the main HfO2 peaks would have overlapped with half Heusler matrix at 29˚ during consolidation by hot press. There is a small peak located at in between 38˚ and 39 ˚ in the composite sample containing 6% HfO_2 with Pd content 20% .The position of this peak is same as seen in composites of half Heusler containing Pd 20% with HfO_2 nano Fig 5.12. The appearance of this peak is due to formation of an additional phase. The secondary phase in that composite is full Heusler. This suggests that there is partial reaction between HfO_2 and half-Heusler.

Figures 5.21 and 5.22 show that the electrical conductivity and Seebeck coefficient of all samples with HfO_2 and without HfO_2 decrease with increasing temperature. Thus retain semiconducting characteristics. The electrical conductivity results are not as favorable though fairly remain stable for some samples There is drastic reduction in electrical conductivities of all composite samples with Pd=0 and this is attributed to the decrease in carrier concentration from 4.9 to $2.6×10^{26}$ m^{-3} after introducing inclusion as shown in Table 5-3. The electrical conductivity of composite sample with Pd=0.2 for 9% HfO_2 nanoinclusion do not show significant change with respect to matrix Pd=.2 no inclusion. Although the Hall effect measurement at room temperature Table 5.3, shows decrease in carrier concentration for all composites of Pd=0.2/

HfO$_2$ but electrical conductivity of composite Pd=0.2/6% vol- HfO$_2$ is higher than the matrix with Pd=0.2 value. The highest room temperature mobility is obtained for a sample containing 3%HfO$_2$ with Pd content 20%. The minimum value of conductivity 0.78(mΩ-cm)$^{-1}$ at 750K is obtained for Zr$_{0.5}$Hf$_{0.5}$NiSn$_{0.99}$Sb$_{0.01}$ with 3%HfO is and maximum value of conductivity is 2.5(μΩ-cm)$^{-1}$ at 300K.The backscattered SEM images of half Heusler phases with HfO$_2$ show the presence of nanosized phase at grain boundaries. The presence of the grain boundaries scatter not only the phonon but also the electron which results in decrease conductivity.

SEM monograph appendices I, J and K show the inhomogeneity all samples and different contrasts are seen indicating presence of many phases Seebeck coefficient shows promising results Fig 5.23 shows improvement in Seebeck coefficient of composite phases is because of the inhomogeneity the increases is not systematic. Comparing Seebeck results with electrical conductivity the variation in Seebeck coefficient is little bit more consistent and curves remain identical. The absolute value of Seebeck coefficient of Zr$_{0.5}$Hf$_{0.5}$NiSn$_{0.99}$Sb$_{0.01}$ with addition HfO$_2$ first increases for 3% HfO$_2$ and then decreases monotonically by increasing HfO$_2$ volume percent but higher than the half Heusler phase. The increase in Seebeck coefficient in the composites phases in this case is due to grain boundary potential barrier scattering according to which high potential barrier caused by point defects, influence increase in Seebeck coefficient thereby decreases the electrical conductivity[7, 8]. The addition of 9% vol-HfO$_2$ in Zr$_{0.5}$Hf$_{0.5}$Ni$_{0.8}$Pd$_{0.2}$Sn$_{0.99}$Sb$_{0.01}$ does not show any significant change in Seebeck coefficient. This is consistent with electrical conductivity data. There is noticeable increase in the Seebeck coefficient in sample containing 3% vol-HfO$_2$ in a. host matrix with Pd=20%. The composite phase Pd=0.2/6% vol-HfO$_2$ does not show increase in Seebeck coefficient and the power factor
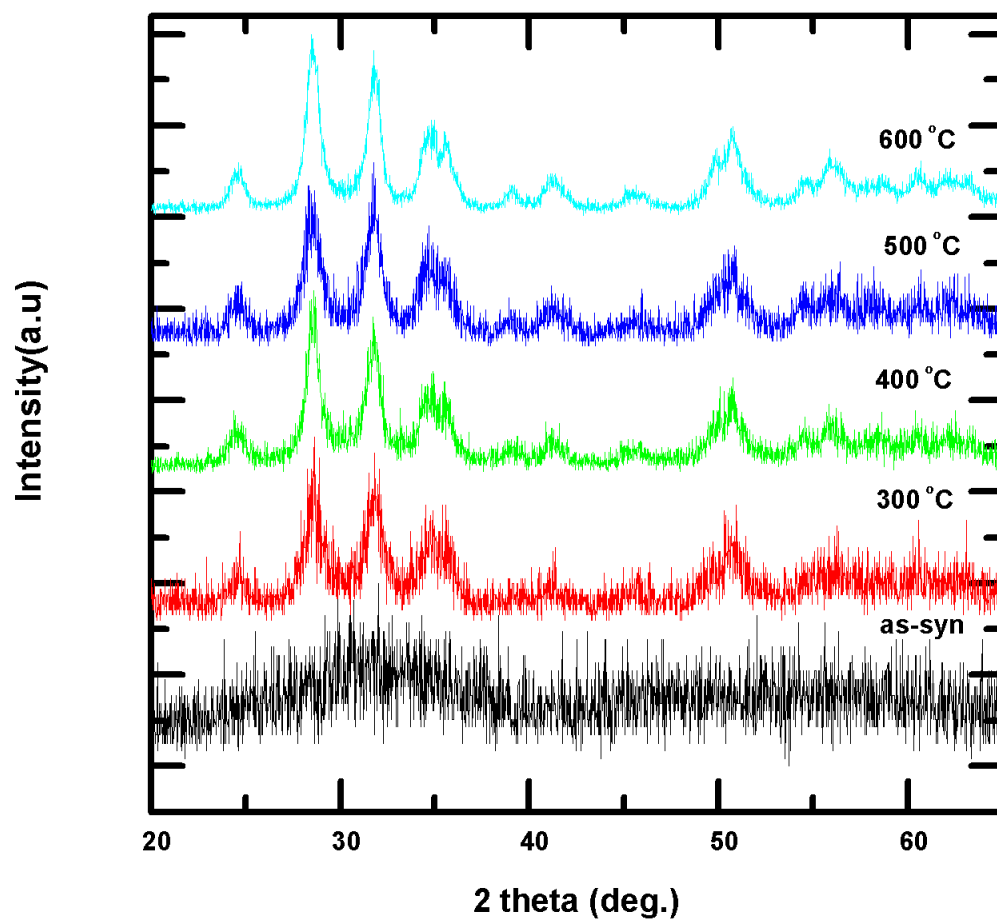
Figure:5-32 PXRD patterns of HO2 nanoparticles at different annealing temperature.
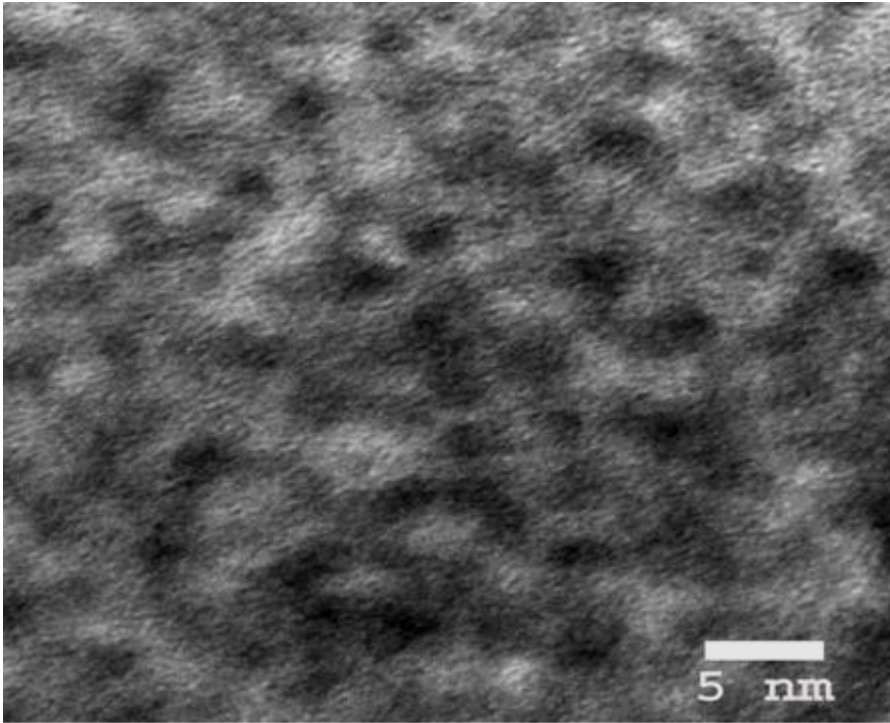
Figure:5-33 TEM image of as-syn HfO nanoparticles.Nanoparticles have different diameter of average 4nm.Due to amorphous nature, edges of nano particles are not clear.
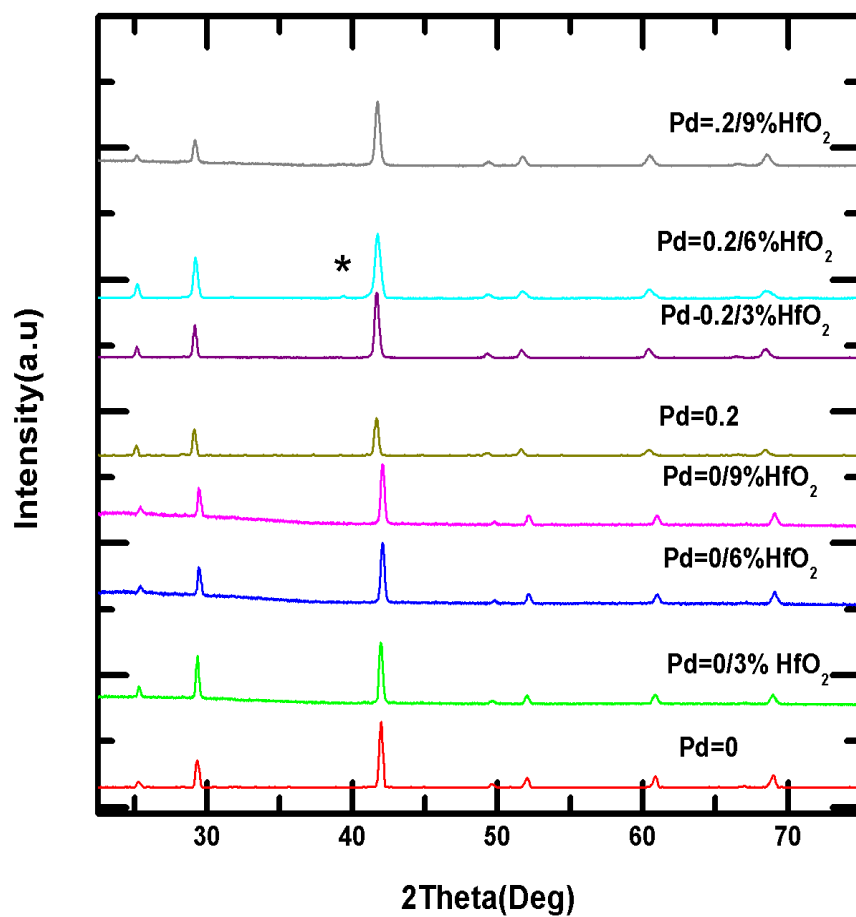
Figure:5-34 Powder diffraction pattern of the mixture containing 3,6 and 9 volume percent HfO$_2$ nanoparticles.
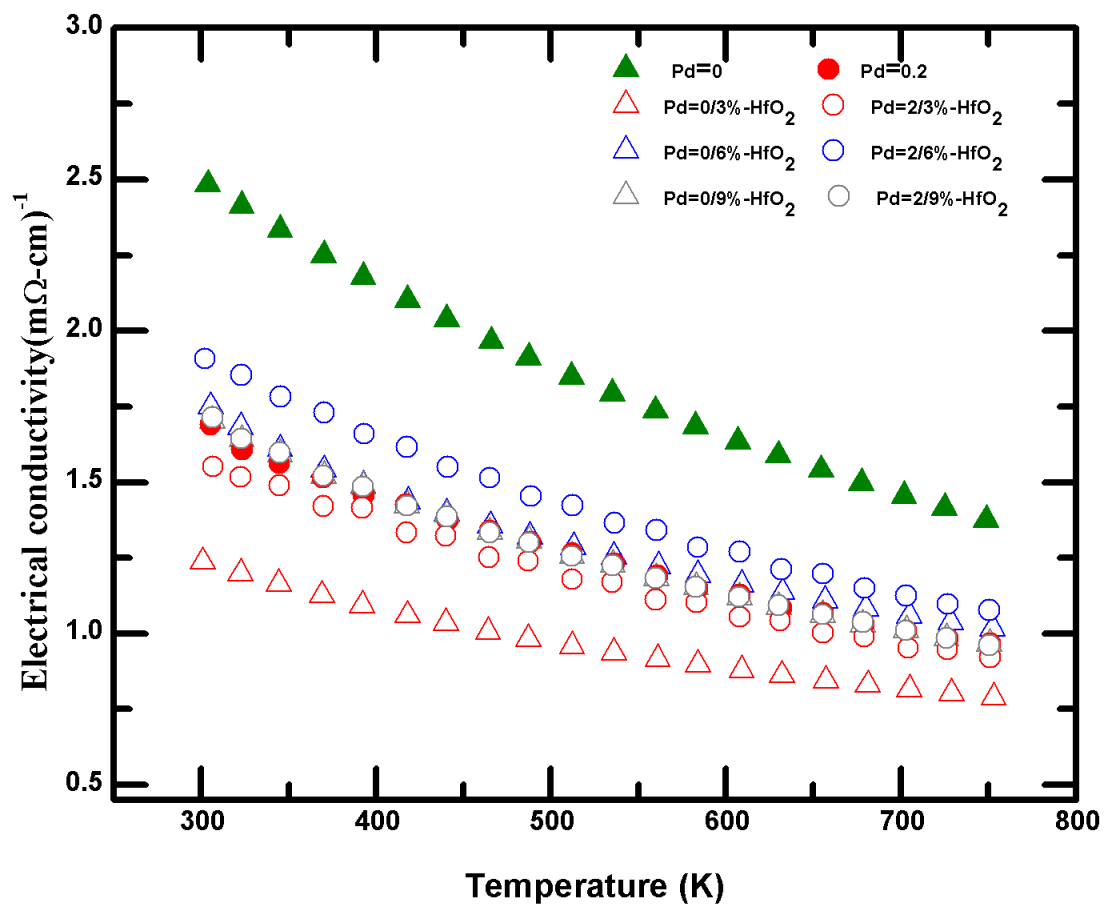
Figure:5-35 Temperature dependence of the electrical conductivity for $Zr_{0.5}Hf_{0.5}Ni_{1-x}Pd_xSn_{0.99}Sb_{0.01}$ and nanocomposites with HfO_2.

Table:5-6 Room temperature Hall coefficient (R_H), resistivity (ρ), carrier concentration (n) and mobility (μ) for the $Zr_{0.5}Hf_{0.5}Ni_{1-x}Pd_xSn_{0.99}Sb_{0.01}$ with x=0,0.2 and of samples containing 3%,65 and 9% volum- HfO_2 nano inclusions

Compounds	R_H $(m^3/C)\times10^{-8}$	$n \times10^{26}$ (m^{-3})	$\rho\times10^{-6}$ $(\Omega\text{-m})$	μ (cm^2/Vs)
$Zr_{0.5}Hf_{0.5}NiSn_{0.99}Sb_{0.01}$	-1.27	-4.89	4.76	26.9
$Zr_{0.5}Hf_{0.5}NiSn_{0.99}Sb_{0.01}/3\%\text{-}HfO_2$	-1.27	-4.91	4.73	26.9
$Zr_{0.5}Hf_{0.5}NiSn_{0.99}Sb_{0.01}/6\%\text{-} HfO_2$	2.28	-2.78	8.03	20.6
$Zr_{0.5}Hf_{0.5}NiSn_{0.99}Sb_{0.01}/9\%\text{-} HfO_2$	-2.44	-2.56	8.45	29.2
$Zr_{0.5}Hf_{0.5}Ni_{0.8}Pd_{0.2}Sn_{0.99}Sb_{0.01}$	-1.75	-3.59	7.99	31.5
$Zr_{0.5}Hf_{0.5}Ni_{0.8}Pd_{0.2}Sn_{0.99}Sb_{0.01}/3\%\text{-} HfO_2$	-2.60	-2.40	6.99	37.5
$Zr_{0.5}Hf_{0.5}Ni_{0.8}Pd_{0.2}Sn_{0.99}Sb_{0.01}6\%\text{-} HfO_2$	2.28	-2.78	8.50	20.6
$Zr_{0.5}Hf_{0.5}Ni_{0.8}Pd_{0.2}Sn_{0.99}Sb_{0.01}6\%\text{-} HfO_2$	-2.44	-2.56	8.37	29.2

is lower as compare to composite phase Pd=0.2/3%vol-HfO$_2$ The power factor decreases for all composites. of Pd=0/3%-6%-9% vol-HfO$_2$.The thermal conductivity decreases for all volume concentration of HfO$_2$ in the composites of Zr$_{0.5}$Hf$_{0.5}$NiSn$_{0.99}$Sb$_{0.01}$. This decrease in thermal conductivity is due a phonon scattering effect at the grain boundaries as shown in Figs 5-25 and 5-26. The lowering in lattice thermal conductivity by addition of nanoinclusion as explained by X.Y. Hang is due to pinning of grain boundaries[9].. The nanoparticles situated at grain boundaries pin grain boundaries and prevent the half-Heusler matrix phase from growing up. The nanoparticles inclusion in Zr$_{0.5}$Hf$_{0.5}$Ni$_{0.8}$Pd$_{0.2}$Sn$_{0.99}$Sb$_{0.01}$ do not show any reduction in thermal conductivity except for sample containing 3% vol-HfO$_2$ but inclusion in this sample also scatter carriers and there is no change in thermal conductivity value at room 300K. Only in the composite Pd=0.2/3% vol-HfO$_2$ power factor is increased All the composites phases obtained by adding HfO$_2$ nanoinclusions ($\approx$4nm) are n-type. Temperature dependence of *ZT* Fig 5.27 shows that there is an improvement of *ZT* about 19.65% at 750 K in Pd=0.2/3%vol-HfO$_2$ This is due to increase in power factor and decrease in thermal conductivity. By increasing the volume fraction of inclusion beyond 3%% no improvement in *ZT* is seen. The highest *ZT* obtained in the composite phase is 0.61 whereas the highest ZT with no inclusion is 0.63 for Zr$_{0.5}$Hf$_{0.5}$NiSn$_{0.99}$Sb$_{0.01}$.
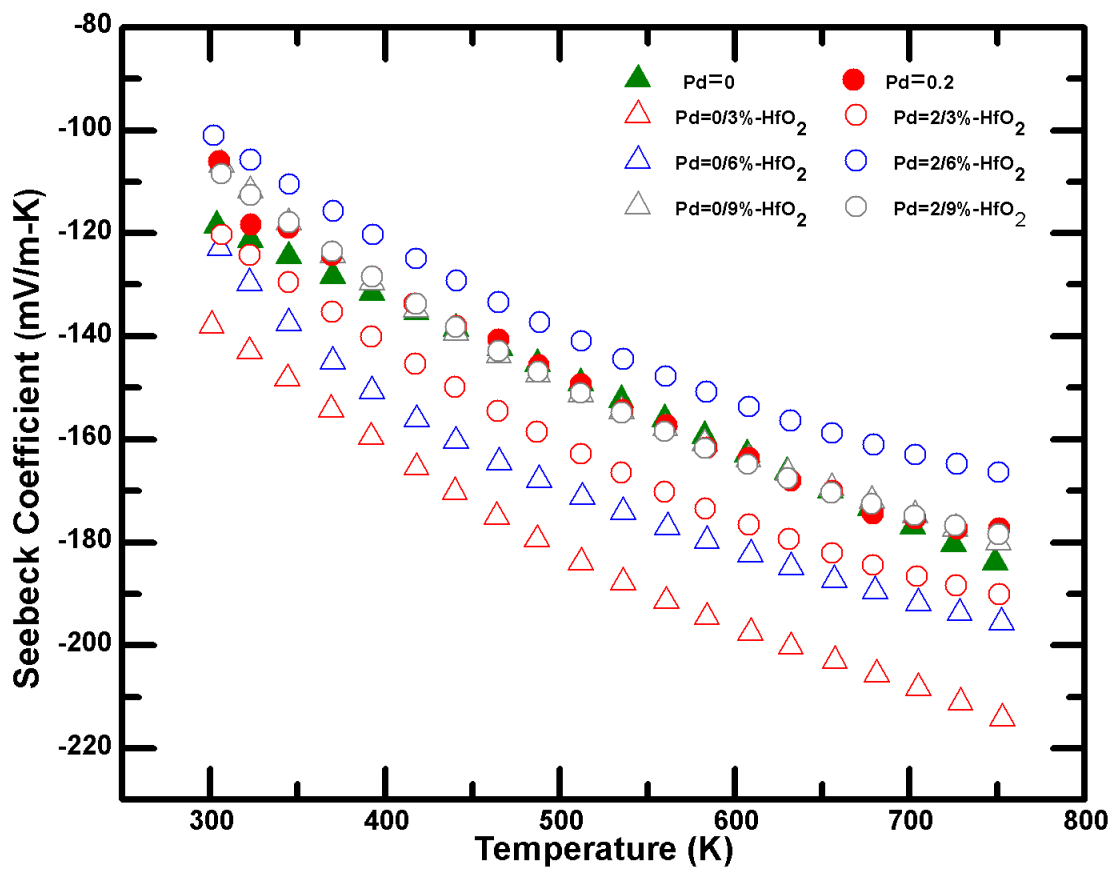
Figure:5-36 Temperature dependence of Seebeck of $Zr_{0.5}Hf_{0.5}Ni_{1-x}Pd_xSn_{0.99}Sb_{0.01}$ (x=0,0.2) and nanocomposites

146
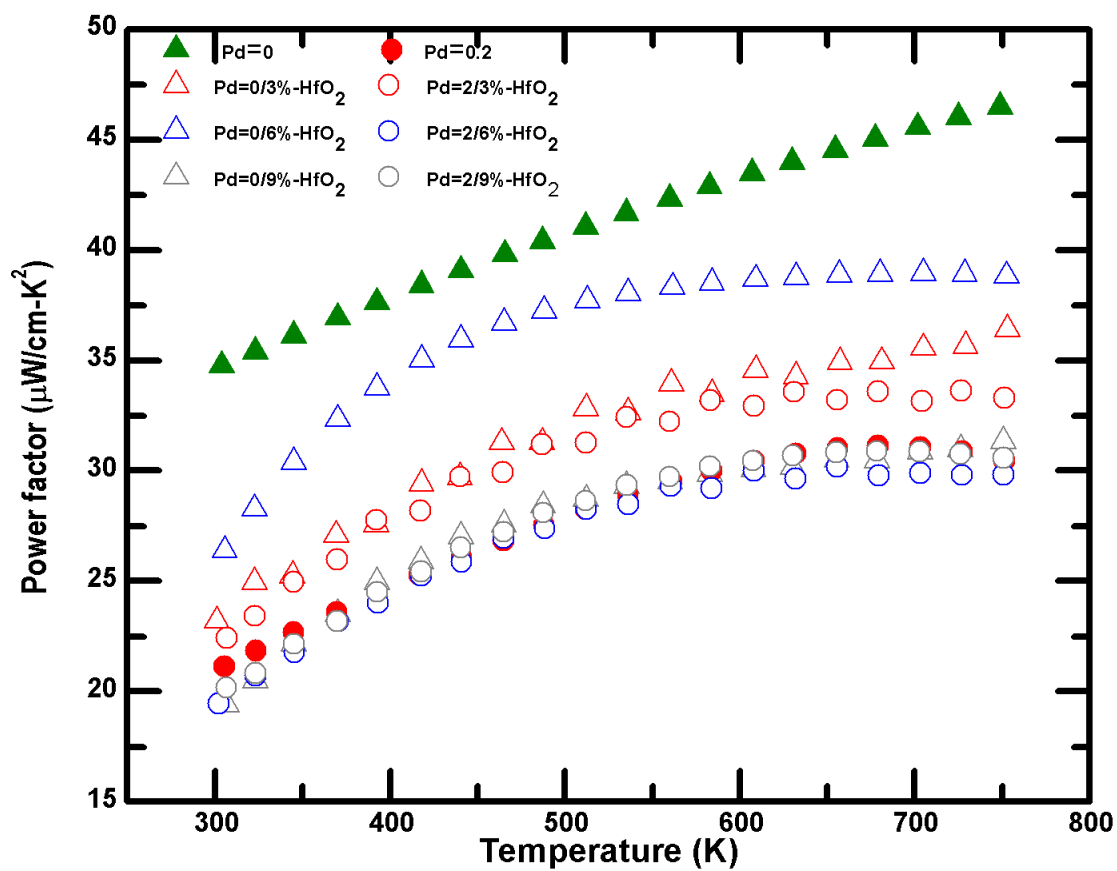
Figure:5-37 Power factor ($S^2\sigma$) as a function of temperature for half Heusler composites of HfO$_2$ nanoinclusions
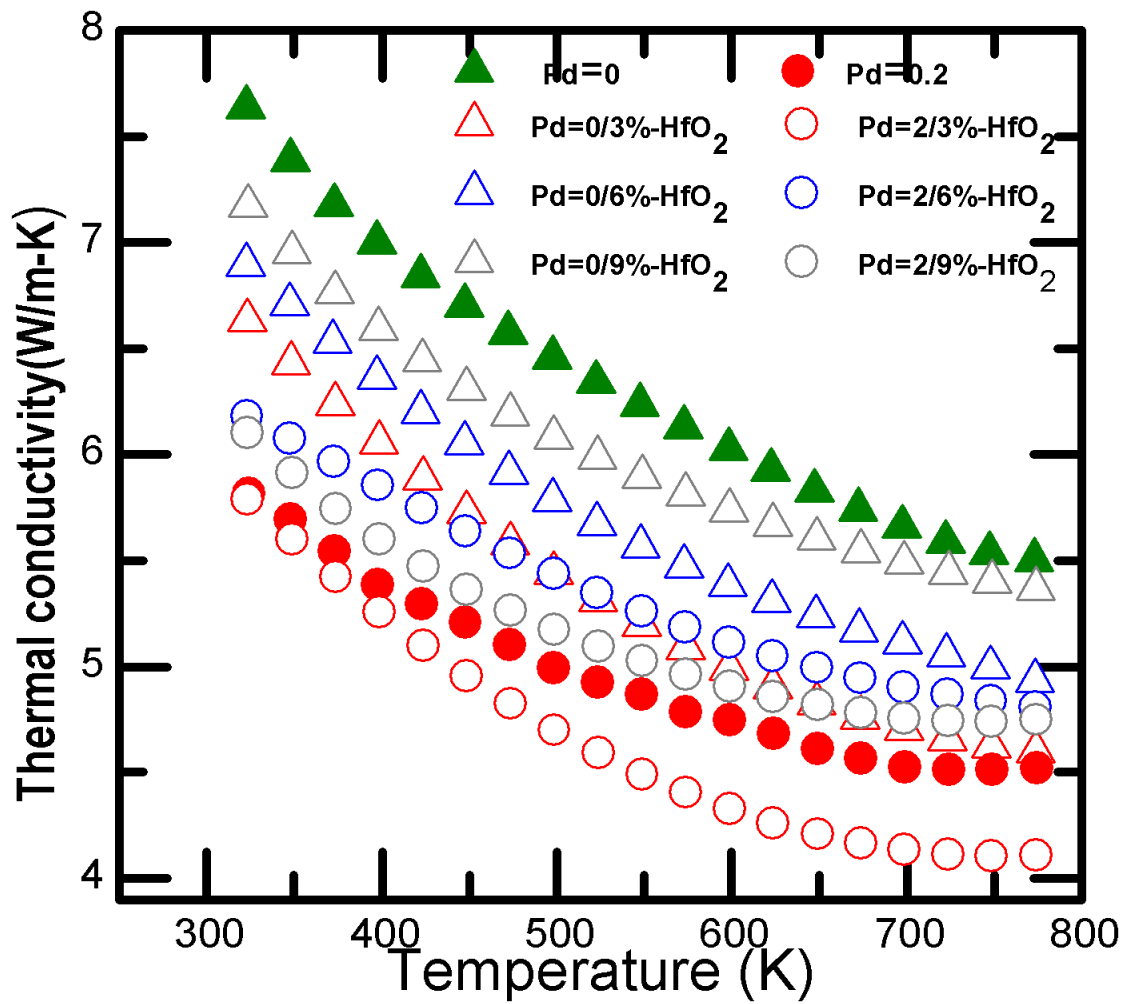
Figure: 5-38 Thermal conductivity as a function of temperature
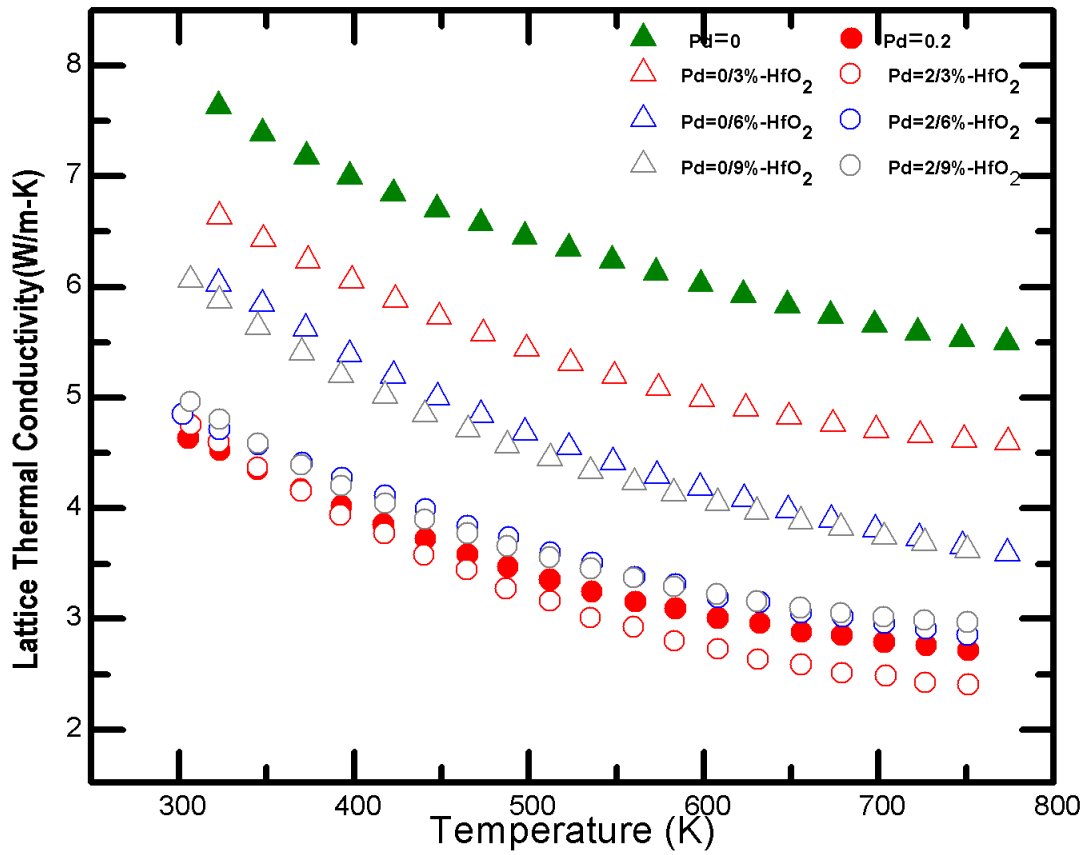
Figure 5-39 Temperature dependence of lattice thermal conductivity for half Heusler samples containing 3%,6% and 9% volume HfO$_2$ nanoinclusions
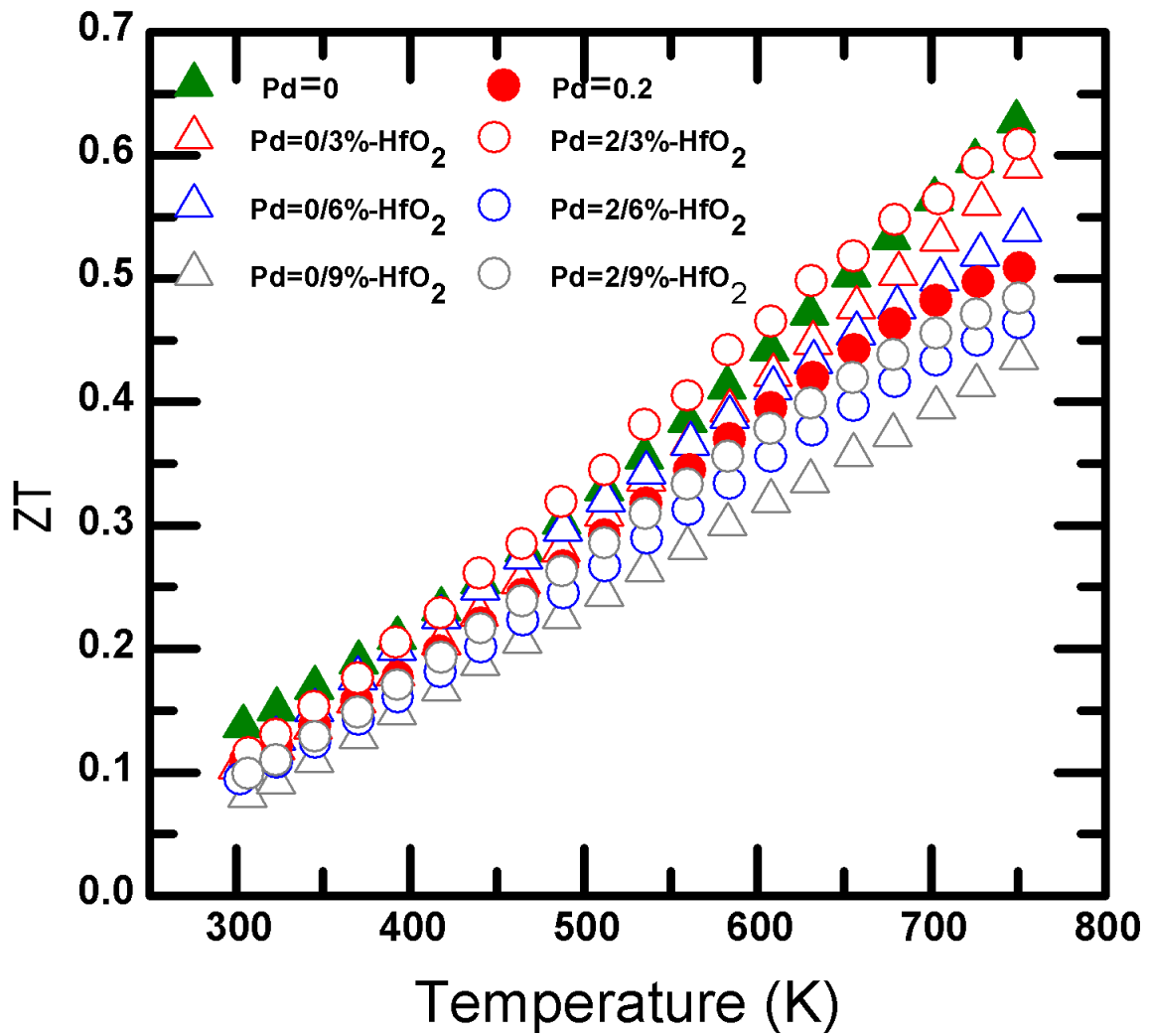
Figure:5-40 Dimensionless figure of merit for half Heusler composites with HfO$_2$ nanoinclusions.

5.4 References

[1]   Q. Shen, L. Chen, T. Goto, T. Hirai, J. Yang, G. P. Meisner, and C. Uher, Applied Physics Letters 79 (2001) 4165.

[2]   H. Hohl, A. P. Ramirez, W. Kaefer, K. Fess, C. Thurner, C. Kloc, and E. Bucher, in Thermoelectric Materials-New Directions and Approaches, Mater. Res. Soc. Proc., Vol. 478 (T.M.Tritt, G.Mahan, J. H.B.Lyon, and M.G.Kanatzidis, eds.), MRS, Warrendale, PA, 1997, p. 109.

[3]   H. Julian Goldsmid, Introduction to Thermoelectricity, Springer, 2009.

[4]   Y. Xia, S. Bhattacharya, V. Ponnambalam, A. L. Pope, S. J. Poon, and T. M. Tritt, Journal of Applied Physics 88 (2000) 1952.

[5]   J. Yang, T. Aizawa, A. Yamamoto, and T. Ohta, Journal of Alloys and Compounds 309 (2000) 225.

[6]   R. Yaqub, P. Sahoo, J. P. A. Makongo, W. M. Nolting, N. Takas, P. F. P. Poudeu, and K. L. Stokes, in Thermoelectric Materials─Growth, Properties, Novel Characterization Methods, and Applications, Mater. Res. Soc. Symp. Proc., Vol. 1267 (J. D. Baniecki, ed.), MRS, Warrendale, PA, 2010, p. 1267.

[7]   K. Kishimoto, M. Tsukamoto, and T. Koyanagi, Journal of Applied Physics 92 (2002) 5331.

[8]   C. H. Seager and T. G. Castner, Journal of Applied Physics 49 (1978) 3879.

[9]   X. Y. Huang, Z. Xu, and L. D. Chen, Solid State Communications 130 (2004) 181.

Appendix A

Techniques for the measurement of thermal conductivity

| Method	Temperature Range	Uncertainty	Materials	Merit	Demerit
Guarded hot place (Steady State)	80-800K	2%	Plastics, glasses Insulations materials,	High accuracy	Long measurement time, large specimen size.
Heat flow meter (Steady state)	-100-200C	3-10%	Plastics, glasses Insulations materials, ceramics	Simple construction and operation	Measurement uncertainty, relative measurement
Comparative (Steady state)	20-1300C	10-20%	Metals, ceramics, plastic,	Simple construction and operation	Measurement uncertainty, relative measurement
Direct heating (Steady state)	400-3000K	2-10%	Metals	Simple and fast measurement, simultaneous determination of electrical conductivity	Only electrically conducting materials
Hot wire, hot strip	20-2000C	1-10%	Liquids, gases, low conductivity solids	Wider temperature range	Limited to low conductivity materials
Laser Flash	-1000-3000C	3-5%-100-3000C	Solids, liquids	Wide temperature range, most solids liquids powders small specimen, fast accuracy at high temperature	Expensive, not for insulation materials

C. Horst;, Saito Tetsuya, and E. Smith Leslie, Springer Handbook of Materials Measurement Methods, Springer, 2006.

Appendix B

Densities of half-Heusler Pd Series ($Zr_{0.5}Hf_{0.5}Ni_{1-x}Pd_xSn_{0.99}Sb_{0.01}$)

Pd Concentration	Geometric Density (gm/cc)	Relative Density (Geometrical/Theoretical Density*100)
0	8.739	95%
0.1	8.720	94.5%
0.2 HP	8.917	96%
0.2 SPS	8.39	90%
0.3	8.421	90.21%
0.4HP	8.59	92%
0.4-SPS	8.872	95.8%
0.5	8.372	89.5%
0.6	8.783	93.6%
0.7	9.061	95.94%
0.8	9.139	96.3%
0.9	9.04	94.7%
1.0	9.54	98.7%
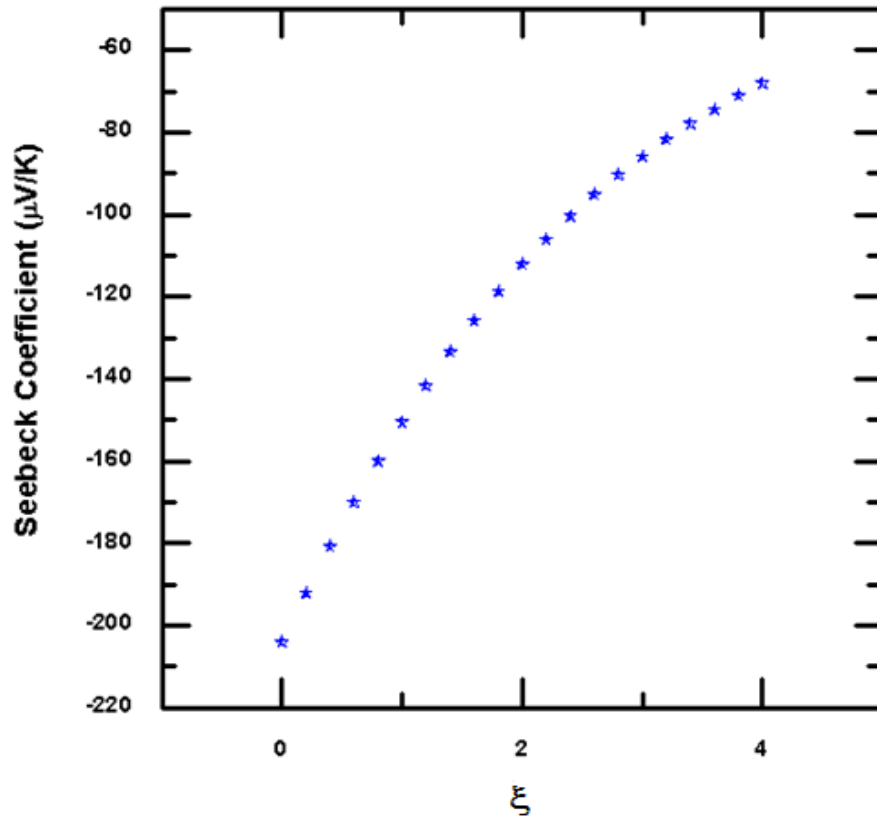
Seebeck dependence on reduced Fermi energy for acoustic scattering mode (r =-1/2)
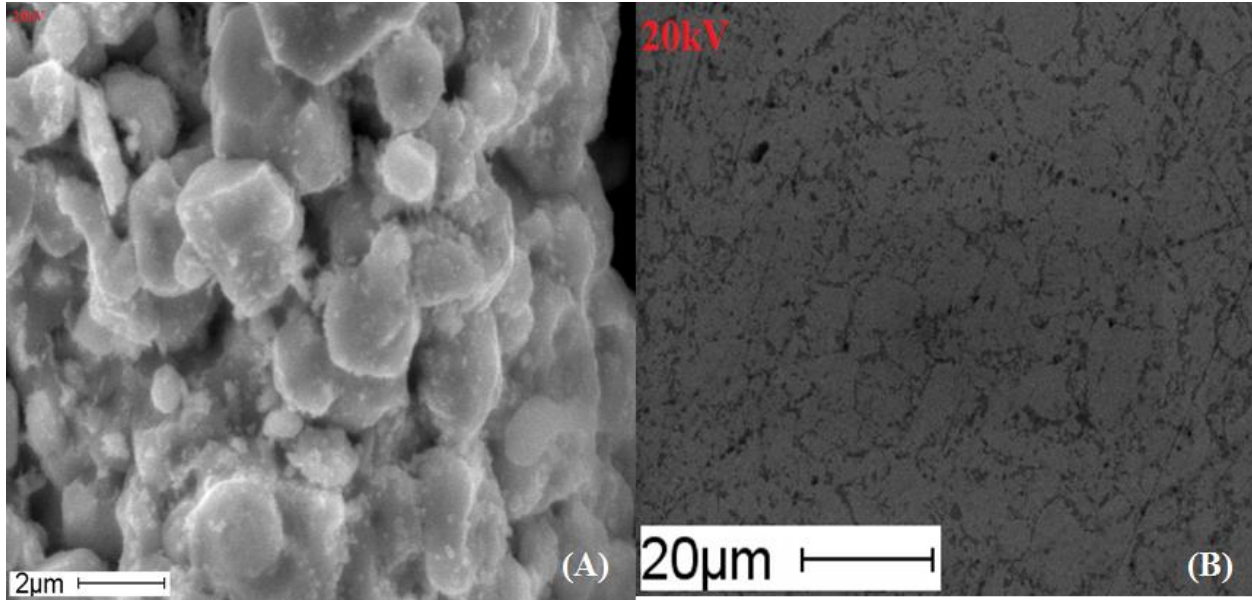
Figure (A)SEI monograph of powder sample of $Zr_{0.5}Hf_{0.5}Ni_{0.8}Pd_{0.2}Sn_{0.99}Sb_{0.01}$ (B) After consolidation by SPS.

Appendix E
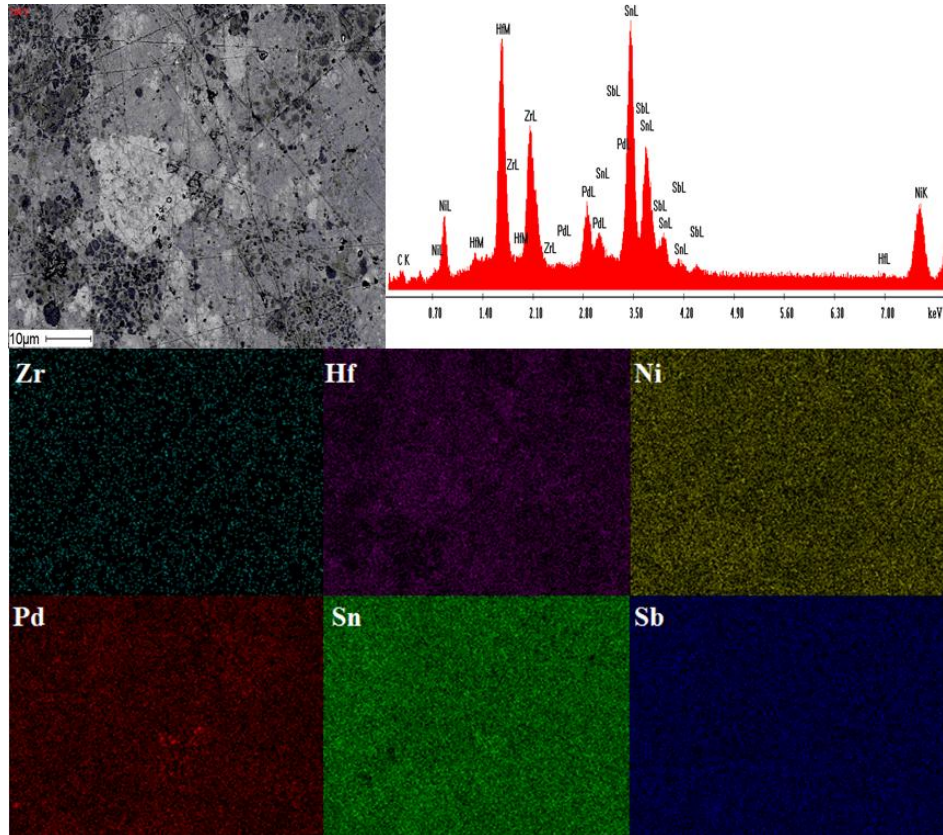
SEI backscattered image of hot pressed $Zr_{0.5}Hf_{0.5}Ni_{0.8}Pd_{0.2}Sn_{0.99}Sb_{0.01}$
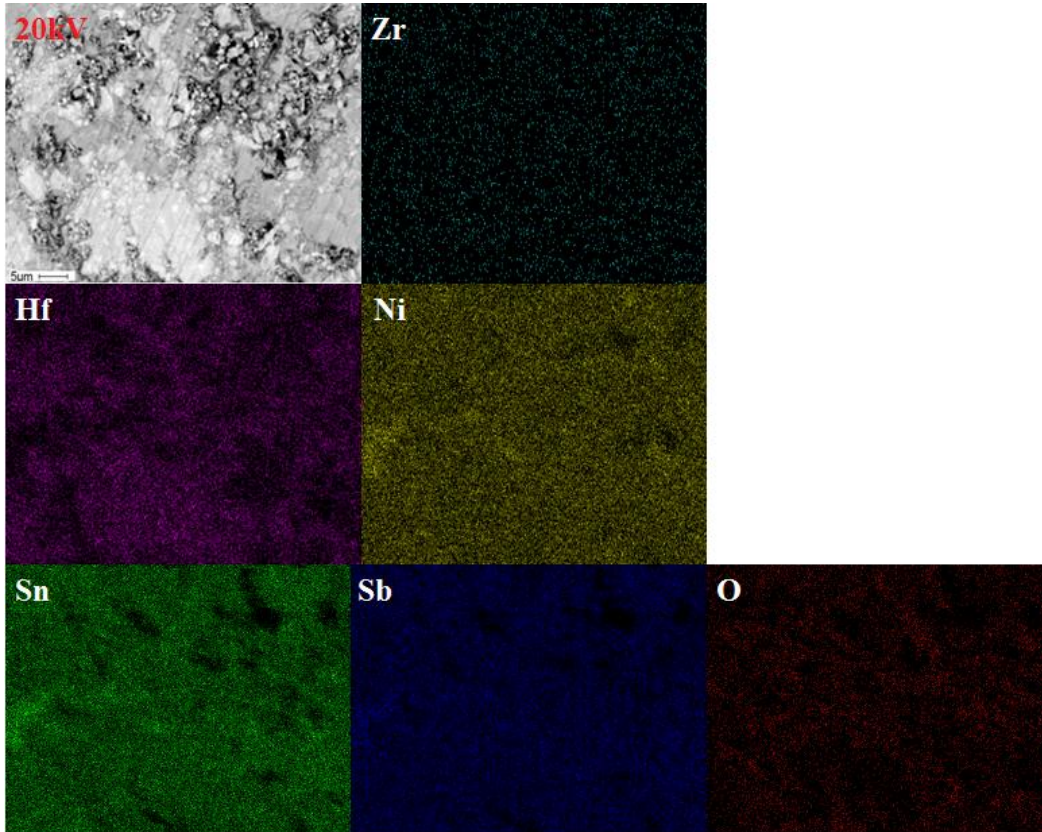
Back Scattered SEM and EDX-mapping monograph of $Zr_{0.5}Hf_{0.5}NiSn_{0.99}Sb_{0.01}$ with 6% vol-NiO.nanoinclusions were mixed by balling for 20 minutes

Appendix G
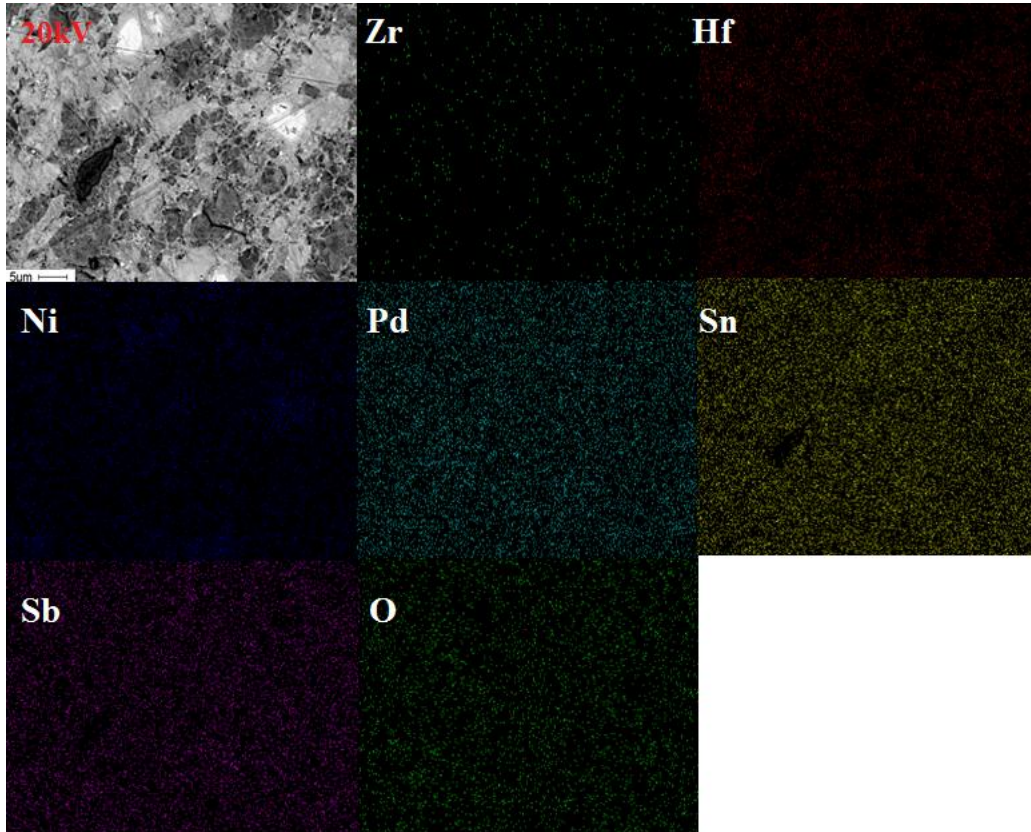
Backscattered SEM and EDX-mapping monograph of Zr0.5Hf0.5Ni0.8Pd2Sn0.99Sb0.01 with 6%vol-NiO. nanoinclusions mixed ball milling for 20 minutes.

Appendix H
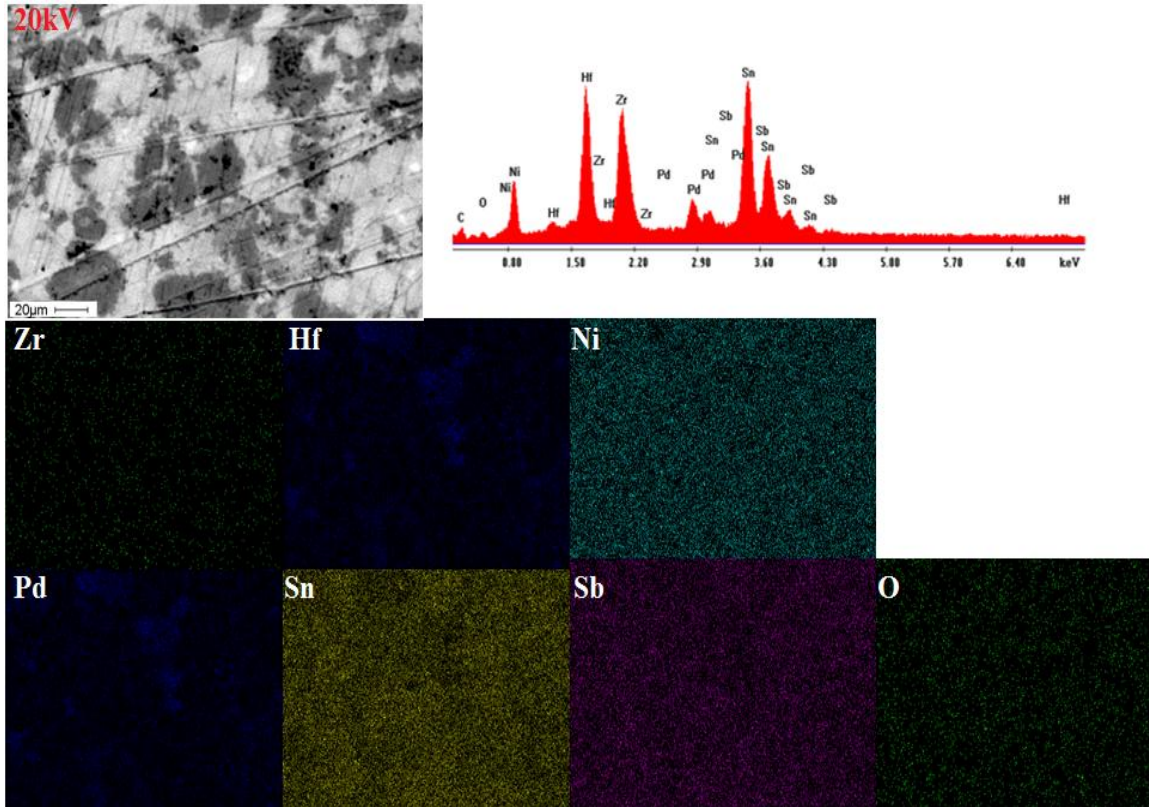
Backscattered SEM and EDX-mapping monograph of $Zr_{0.5}Hf_{0.5}Ni_{0.8}Pd_2Sn_{0.99}Sb_{0.01}$ with 6% vol-NiO.nanoinclusions mixed by hand inside the glove box in agate mortar
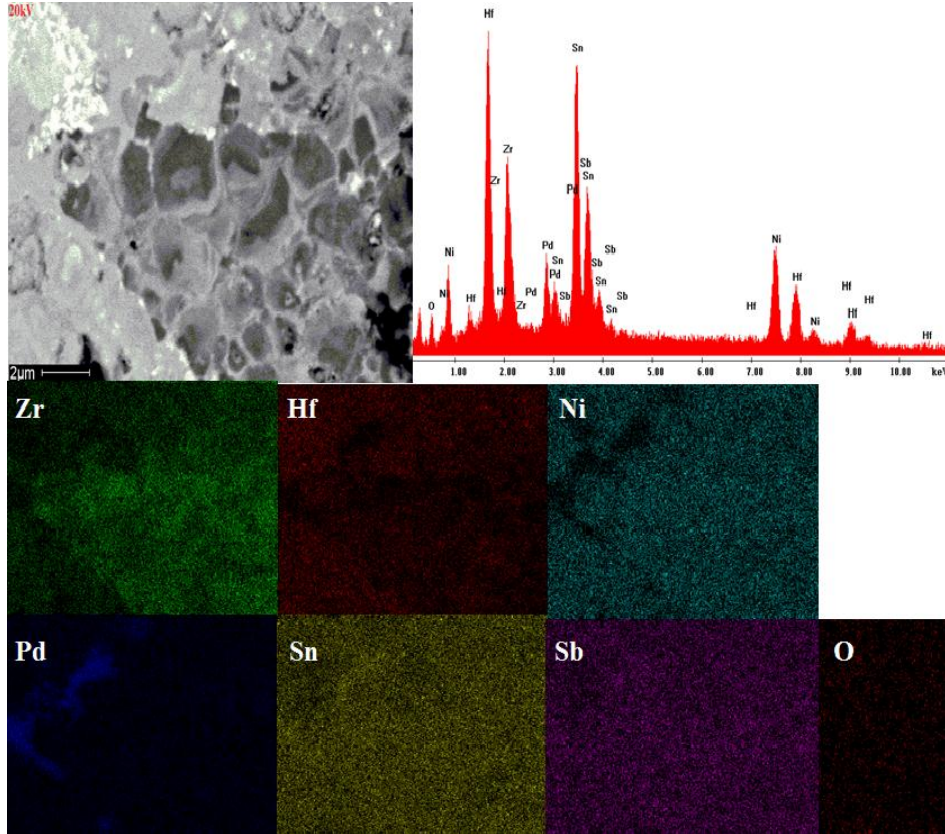
Backscattered SEM and EDX-mapping monograph of $Zr_{0.5}Hf_{0.5}Ni_{0.8}Pd_{0.2}Sn_{0.99}Sb_{0.01}$ with 3% vol-HfO_2

Appendix J
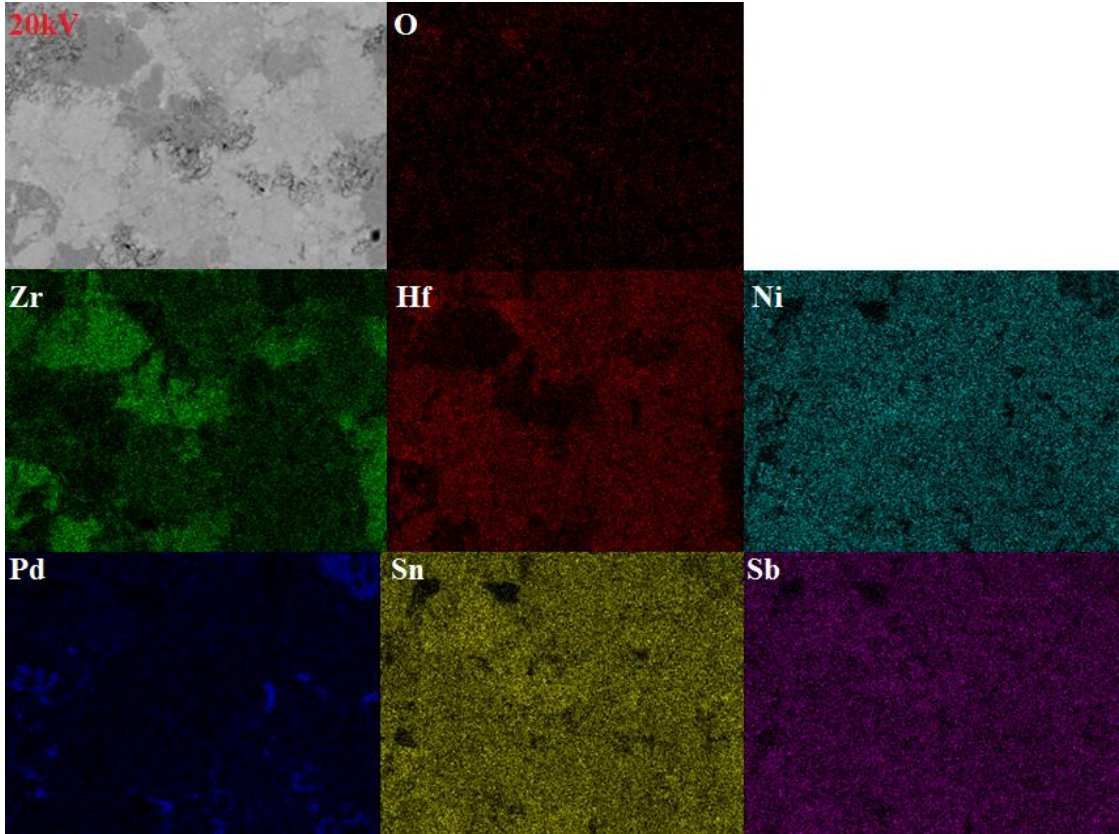
Backscattered SEM and EDX-mapping monograph of $Zr_{0.5}Hf_{0.5}Ni_{0.8}Pd_{0.2}Sn_{0.99}Sb_{0.01}$ with 6% vol-HfO_2

Appendix K
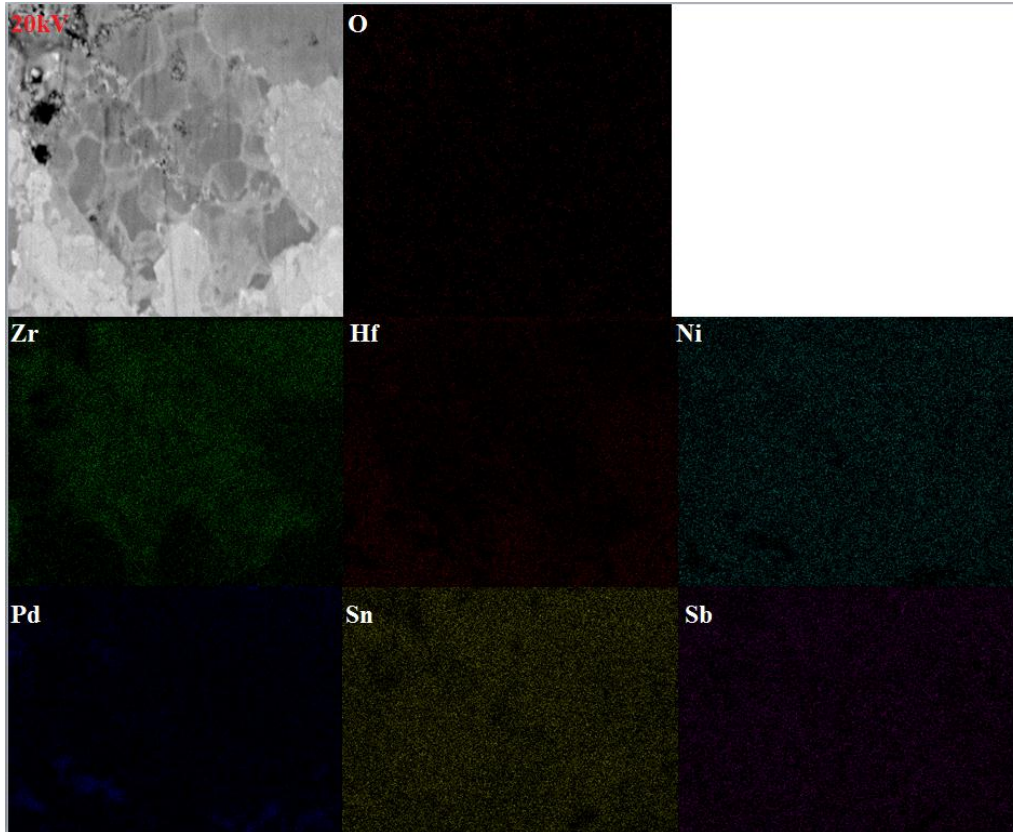
Backscattered SEM and EDX-mapping monograph of $Zr_{0.5}Hf_{0.5}Ni_{0.8}Pd_{0.2}Sn_{0.99}Sb_{0.01}$ with 9% vol-HfO_2

Vitae

Rumana Yaqub was born in Sargodha, Paksitan daughter of Mohammed Yaqoob Goindi and Kulsoom Akhter. After completing B.Sc. at Lahore College for women, Punjab, Lahore She went to Govt College University, Lahore to pursue M.Sc. in Physics. After receiving master degree in Physics in 1989 she pursued her carrier as lecture in Govt APWA College for Women for 10 years. Meanwhile she got diploma in French as second language as well Associate Degree in computer application and programming from American National College Pakistan. She came to United States and worked completed Master in Physics from Wayne State University, Michigan. She entered the Graduate School at the University of New Orleans in 2008 to pursue Ph.D in engineering and Applied Sciences